Summer 8-2023

Chemical and Physical Interaction Mechanisms and Multifunctional Properties of Plant Based Graphene in Carbon Fiber Epoxy Composites

Daniel W. Mulqueen
Old Dominion University, dan.mulqueen@gmail.com

Recommended Citation

Mulqueen, Daniel W.. "Chemical and Physical Interaction Mechanisms and Multifunctional Properties of Plant Based Graphene in Carbon Fiber Epoxy Composites" (2023). Doctor of Philosophy (PhD), Dissertation, Mechanical & Aerospace Engineering, Old Dominion University, DOI: 10.25777/39mt-mr68
https://digitalcommons.odu.edu/mae_etds/366

CHEMICAL AND PHYSICAL INTERACTION MECHANISMS AND MULTIFUNCTIONAL PROPERTIES OF PLANT BASED GRAPHENE IN CARBON FIBER EPOXY COMPOSITES

by

Daniel W. Mulqueen
B.S. May 2008, Colorado School of Mines

A Dissertation Submitted to the Faculty of
Old Dominion University in Partial Fulfillment of the
Requirements for the Degree of

DOCTOR OF PHILOSOPHY

MECHANICAL ENGINEERING

OLD DOMINION UNIVERSITY
August 2023

Approved by:

Oleksandr G. Kravchenko (Director)

Gene Hou (Member)

Diego Pedrazzoli (Member)

Tian-Bing Xu (Member)

ABSTRACT

CHEMICAL AND PHYSICAL INTERACTION MECHANISMS AND MULTIFUNCTIONAL PROPERTIES OF PLANT BASED GRAPHENE IN CARBON FIBER EPOXY COMPOSITES

Daniel W. Mulqueen
Old Dominion University, 2023
Director: Dr. Oleksandr G. Kravchenko

Graphene has generated substantial interest as a filler due to its exceptional strength, flexibility, and conductivity but faces obstacles in supply and implementation. A renewable, plant-based graphene nanoparticle (pGNP) presents a more accessible and sustainable filler with the same properties as mineral graphenes. In this study, the mechanisms of graphene reinforcement in carbon fiber reinforced plastic (CFRP) were examined, along with the resulting improvements to mechanical strength, resistance to crack propagation, electrical and thermal conductivity at elevated temperatures. pGNP, produced from renewable biomass, was shown to have a graphitic structure with flakes 3-10 layers thick and a median lateral size of 240 nm with epoxide and carboxyl functional groups. pGNP was sprayed on carbon fiber/epoxy prepreg at loadings from 1.1 g/m^2 to 4.2 g/m^2. An even particle dispersion was achieved using a spray application in a water/alcohol suspension with the addition of surfactants and dispersion aides. Results show interlaminar pGNP improved Mode I fracture toughness at crack initiation by 146% at 20°C and 126% at 90°C, with fracture toughness improved by 53% and 52% during propagation at 20°C and 90°C, respectively. Mode II fracture toughness was not changed at 20°C and improved 55% at 90°C. pGNP addition increases flexural modulus by 15%, flexural strength by 17%, and interlaminar shear strength by 17%, as well as electrical conductivity by 397% (κ_{22}) and thermal conductivity by 27% (k_{11}), with these improvements observed at 1.1-2.3 g/m^2 spray loadings. Raman spectroscopy, X-ray photoelectron spectroscopy (XPS), and dynamic mechanical analysis (DMA) show polymer crosslinking with graphene surface groups and the resulting restriction of side chain movement. These restrictions improve composite performance at ambient and elevated temperatures, extending the damage process zone and increasing fracture toughness, as well as improve particle/matrix interaction, leading to improved conductivity.

To:
My father, Daniel Patrick Mulqueen
In loving memory,
You engaged my interests and fueled my love of science and the natural world.

You have to learn and keep learning.
-Gil Scott-Heron

Truth springs from the earth; And righteousness looks down from heaven.
-Psalm 85:11

ACKNOWLEDGMENTS

I owe my tremendous thanks to my advisor Dr. Oleksandr G. Kravchenko, for giving me the opportunity to work with him, for his guidance and support through my PhD, and for the insight he has given me. This dissertation would not have been possible without his vision, direction and the physical resources he made available to me, despite my remote learning. I am thankful to my committee members Dr. Gene Hou, Dr. Diego Pedrazzoli, and Dr. Tian-Bing Xu, as well as Dr. Miltos Kotinis for their encouragement, technical discussions, and feedback. I want to thank all of the students in my research group in the Mechanical and Aerospace Engineering Department at Old Dominion University that offered help and support.

I would like to thank Dr. Thomas Furtak for introducing me to the worlds of materials science and nanomaterials. Your guidance sparked an interest that has driven my career. I also owe thanks, in memory, to the late Dr. Thomas B. Reed, who introduced me to pyrolysis and to the potential of plant-based carbons.

Last, but not least I would like to give my deepest thanks to my family. To my daughter Amalia, who has grown so much over these years and who got to enjoy being a remote student alongside her father. To my partner, Katherine Brown, you mean the world to me, and I could not have done this without your help and support.

NOMENCLATURE

a	Crack Length, m
b	Beam Width, m
DMA	Dynamic Mechanical Analysis
E	Modulus of Elasticity, GPa
E'	Storage Modulus, GPa
E''	Loss Modulus, GPa
EC	Electrical Conductivity, S/m
G_C	Critical energy required for crack extension
G_{Dis}	Energy dissipation due to viscous effects and plasticity
G_{IC}	Critical energy required for crack extension in Mode I Fracture
G_{IIC}	Critical energy required for crack extension in Mode II Fracture
GNP	Graphene Nanoplatelet
GO	Graphene Oxide
h	Beam Height, m
I	Current, A
k	Thermal Conductivity, W/m*ºK
l	Span Length, m
P_c	Critical Load, N
pGNP	*Plant-Based* Graphene Nano-Platelet
R	Electrical Resistivity, Ω
rGO	Reduced Graphene Oxide
SEM	Scanning Electron Microscopy
TC	Thermal Conductivity, W/m*ºK
TEM	Transmission Electron Microscopy
V	Voltage, V
α	Degree of Cure, (No Units)
δ	Load Point Displacement, m
κ	Electrical Conductivity, S/m
ρ	Electrical Resistivity, Ω·m
σ_f	Flexural Strength, MPa

TABLE OF CONTENTS

LIST OF TABLES

Table Page

LIST OF FIGURES

CHAPTER 1

INTRODUCTION

Graphene is composed of a hexagonal lattice of aromatically bonded carbon atoms, either one layer thick or consisting of a few stacked layers [1]. It has a unique combination of properties, including high mechanical strength, high electrical conductivity, and high thermal conductivity, which make it highly attractive for a wide range of applications, including composite materials where a small amount of graphene can significantly increase the strength, stiffness, and toughness while also improving the electrical conductivity and thermal stability of the material [2–6]. However, there are several issues with the use and adoption of graphene; graphene has been difficult and expensive to produce on a commercial scale, there is currently no standardized method for characterizing graphene, making it difficult for researchers to compare results and for industry to adopt it into products, and integrating graphene into material systems—composite and otherwise—has proven difficult due to issues with self-agglomeration of graphene particles [1]. This dissertation aims to address these issues in the following ways: First, a plant-based graphene nanoplatelet (pGNP) will be introduced as a more available, lower cost pathway to conventional graphene production; second, methods will be discussed to illustrate the connection between graphene characterization and utilization in a material system and; third, the roots of particle agglomeration in graphene/surface interactions will be highlighted.

Agglomeration is frequently cited as a primary obstacle to effective graphene utilization [7–10]. Liquid phase dispersions are well understood, and well dispersed particles require that Brownian motion be a sufficient energy barrier to aggregation [1]. Graphene, owing to its unique, hybridized, aromatic lattice, has very high Van der Waals self-interaction [11], which—when coupled with the extremely high theoretical surface area of monolayer graphene (~2590 m^2/g [1])—results in substantial agglomeration potential which requires a high degree of energy to overcome [12–15]. This agglomeration is given as the cause for poor filler-matrix interfaces which result in negative impacts to composite properties, however—as this dissertation aims to show—graphene agglomeration is the result of poor filler-matrix interfaces, rather than the cause. Proper material characterization and system design can be used to engineer effective graphene composites.

1.1. Nanomaterials in Polymer Composites

Plastic based composite components and Carbon fiber Reinforced Plastics (CFRP) in particular offer several advantages over metals for OEM parts manufacture; lighter weight, higher specific strength and stiffness, and impact resistance [16]. Plastic utilization is growing rapidly [17,18], but fiber reinforced composites suffer from several drawbacks as compared to traditional materials including poor interlaminar toughness, high temperature sensitivity, and low thermal and electrical conductivity all of which are functions of the polymer matrix [16,19]. Temperature dependence of the fracture resistance of composites is critical to many applications of the materials, but temperature studies have been underrepresented in literature [20].

Graphene is a Carbon Nanoparticle (CNP) composed of a large network of aromatic, sp2 bonded carbon rings in planar lattices. Nanomaterials are defined as having at least one dimension on the nanoscale (1-100 nm) and graphene is notable for having a thickness of 0.3-10 nm with lateral dimensions of hundreds or thousands of nanometers [21]. This results in materials which interact on both the scale of chemical interactions as well as the scale of mechanical interactions [22]. Graphenes have shown potential for use in composite materials due to high mechanical strength as well as exceptionally high conductivity [2–6], however success in application has relied on successful dispersion of CNP and integration into polymer systems [1]. Graphene nanoparticles (GNP) have potential in enhancing the interlaminar properties of the composite matrix [23]. Very small loadings of graphene have shown mechanical improvements in composite systems [21,24–26].

There has been substantial work showing the effectiveness of GNP in improving fracture strength at ambient temperatures, [25–30]. Other work demonstrated the effectiveness of using GNP to improve the thermal stability of composite materials [31–33] and the electrical conductivity with interlaminar applications [34–37]. Studies examining graphene coated fibers in composite systems have examined the temperature dependence of interfacial bonding between fibers and the polymer matrix. One study showed that at cryogenic and room temperatures, graphene oxide fiber coating improves interfacial bonding but at elevated temperatures defects between the graphene oxide and the polymer are enhanced [38]. A study of a CFRP using carbon fibers with electrophoretically deposited graphene showed improvements to interlaminar shear strength of 25% at ambient temperature, 16% at 70ºC, and 13% at 120ºC [39].

GNP interface with polymers at both the molecular and macroscopic scale, resulting in multifunctionality of GNP nanocomposites in terms of effective thermal-electrical, mechanical and viscoelastic properties, respectively. As seen by these examples of the prior studies, GNP nanoparticles are commonly considered as a reinforcement on a smaller scale without focusing on the potential impacts of GNP on the mobility of the cured network, especially at elevated temperatures. The effects of GNP on TC and fracture properties at elevated temperature properties have not been widely explored, despite offering insight into polymer-nanoparticle interactions. This work aims to use a broad selection of methods to characterize the mechanisms of interlaminar pGNP reinforcement on a CFRP system.

1.2. Problem

1.2.1. Fracture

Due to the wide variety of fiber and matrix properties, there is a range of elevated temperature behaviors for composite fracture. Generally, temperature increase results in reduced elastic modulus [40], however, the effect of temperature on strength and toughness depends on the epoxy matrix system used in the composite. In studies utilizing resins with high glass transition temperatures (T_G) (170ºC-190 C), the fracture resistance increases over ambient conditions by 19% at 80 °C [41] and 36% at 90 °C [20]. This is due to increases in the ductility of the matrix and the testing temperature relative to the T_G of the resin. Conversely, a study of resin based unidirectional CFRP with T_G of 180°C showed a decrease in toughness at 150 °C of ~20% and an increase in toughness of ~40% at 100°C [42]. Another study used resin with T_G of 60ºC and found that G_{IC} was maximized at T_G and reduced at higher temperatures by 50% at 100ºC and 86% at 140ºC [43]. Similarly, in Mode II fracture, G_{IIC} was shown to increase slightly at 70ºC and decrease by nearly 40% at 100ºC due to resin softening [44]. Other mechanical properties, such as flexural strength show similar temperature dependence. An examination of flexural strength from -100ºC to 100ºC showed that flexural modulus was consistent at low temperatures and decreased 50% at 100 ºC from ambient values [45]. Flexural strength at -100ºC was 75% greater than ambient and reduced at elevated temperature: at 60ºC it was 8% lower and at 100ºC was 83% lower than ambient [45]. Studies of CFRP tensile strength have shown strong temperature dependence on tensile strength, with a significant loss of strength (30-50%) occurring well before T_G due to matrix softening and reduction of fiber–matrix adhesion [46].

Very small loadings of graphene have shown mechanical improvements in composite systems. 0.1% w/w loading of graphene in bisphenol-A epoxy provided improvements of 40%, 31% and 53% to tensile strength, modulus, and fracture toughness as compared to 3%, 14%, and 20% with carbon nanotubes [24]. A loading of 0.2% w/w has shown improvements of ~34%, 20%, 83%, and 55% to tensile strength, modulus, toughness, and flexural strength, respectively [21]. The study of the mechanisms of GNP reinforcement has been limited, examining fracture through microscopy or ignoring mechanisms of composite toughening altogether [1,23,25–27,47–49] with a small number considering possible chemical interactions between GNP functional groups or physical interactions on the scale of polymer molecules [50–53], and very few examining behavior at elevated temperature.

1.2.2. Conductivity

Thermal and electrical conductivity are seeing a growing demand as properties such as heat and current dissipation are of increasing concern for applications for miniaturized electronics to electric vehicle construction [2]. Lack of electrical conductivity is an obstacle to the use of reinforced thermosetting plastics in applications where conductivity is essential such as the aerospace industry [3]. Electrostatic painting systems are widely used in automotive coatings but have difficulty with plastic parts because of a lack of electrical conductivity [4]. Plastics are widely used for corrosion resistant tanks and piping, but static build up due to a lack of conductivity creates an explosions hazard [5]. The transition from metal to plastic parts in automotive structures, such as battery enclosures, requires the addition of electrically conductive elements to provide shielding from electromagnetic interference [54].

Carbon nanomaterials, such as graphene, have exceptionally high carrier mobility which promises dramatic increases in electrical and thermal conductivity as well as benefits to the physical properties of the plastic parts [2–6]. The large, aromatic structures of GNP create long mean free paths for electrons without electron-electron interactions, which gives graphene a fundamentally different mechanism for conductivity from metals and semimetals [55]. This unique physics gives pristine graphene a conductivity of up to 100 MS/m–70% higher than copper–and in macroscopic application graphene has shown conductivity of 70-80 MS/m [56]. Coupled with a density of 0.3 g/cm^3–as compared to copper (8.93 g/cm^3) and aluminum (2.69 g/cm^3)–graphene has a theoretical specific electrical conductivity of 333.3 MS·cm^3/g·m, giving graphene a specific electrical conductivity 50 times higher than copper and 23 times higher than aluminum [57]. Functionally, the percolation limit of graphene may be reached at 1% loading w/w, although at these loadings' conductivity may be increased by nine orders of magnitude [58].

Thermal conductivity is also an important problem for composite manufacture. As compared to metals, the CRFP has very low thermal conductivity, the thermoset matrix in most epoxies has a thermal conductivity of ~0.17-0.79 W/m·K, while the fibers have a conductivity of 24.0 W/m·K. The thermal conductivity is anisotropic, and variations in fiber volume, fiber orientation, and configuration all affect the final conductivity, but ranges from 0.5 W/m·K (through the thickness) to 3 W/m·K (in the fiber direction) are reasonable [59]. Aluminum has a thermal conductivity of 200 W/m·K and copper has a thermal conductivity of 400 W/m·K, while graphene has a thermal conductivity of as much as 4000 W/m·K [55].

1.2.3. Dispersion and Agglomeration

Carbon nanomaterials have a potential in enhancing the interlaminar properties of the composite matrix when used as an interlaminar layer [23]. Interlaminar graphene addition offers multiple benefits over nanoparticle dispersion in resin. First, the uniform dispersion of nanoparticles through the matrix reinforces critical as well as noncritical regions equally resulting in a higher than necessary cost. Secondly, small nanomaterial addition increases the resin viscosity substantially, resulting in difficult processing in resin transfer molding. Spray application of nanoparticles offers a solution to both issues. By not mixing the nanoparticles directly, resin viscosity is not increased and by only applying nanoparticles to critical, interlaminar, areas, costs are optimized [60]. Additionally, in a resin transfer process, the fibers can filter nanoparticles from the resin, creating agglomeration and uneven distribution through the composite [7]. Targeted interlaminar addition of carbon nanoparticles (CNP) have shown increases in fracture toughness [34] as well as functionalization for structural health monitoring [35] and applications in microwave welding [36]. Hand rolling, or coating of graphene interlaminar layers can be time consuming and inconsistent. The use of interleaf layers adds complexity and mass beyond the low mass of interlaminar GNP, as well as potentially interfering with resin impregnation.

1.2.4. Barriers to Graphene Use

While graphene offers several benefits, it has yet to succeed widely in the marketplace for several reasons. Graphene has high levels of Van der Waals self-interaction which are correlated to aggregation and difficulty in dispersion and application [1,2]. Graphene materials have maintained a high cost, due to short supply of high-quality graphite precursors and difficulty producing graphene nanoparticles. Another issue which has not been broadly discussed is carbon emissions and the significant environmental impact of graphene production. Due to increased environmental awareness—as well as environmental regulations—composite manufacturers are utilizing new material from renewable, plant-based feedstocks [3]. Graphene production from graphite through the chemical reduction of graphene-oxide, ultrasonic exfoliation, and thermal exfoliation are all energy intensive, requiring 70-2000 MJ/kg to produce, utilize several hazardous chemicals and produce hazardous pollutants [4–7].

1.3.Scope of Work

This dissertation focuses on experimental characterization of CRFP composites treated with interlaminar spray of pGNP in order to determine the mechanisms of interaction responsible for pGNP reinforcement and multifunctionality. Due to the unique scale and morphology of pGNP, interactions in the composite system were investigated on the order of; *(i)* chemical bonding, *(ii)* polymer chain vibrations and, (iii) direct physical reinforcement. To this end, this dissertation aims to use a broad selection of methods to characterize the mechanisms of interlaminar pGNP reinforcement.

Characterization of pGNP particles develops a basis for the mechanisms of interaction which were observed. Analysis of the reaction kinetics under curing presents insight into the impacts of pGNP addition on reaction kinetics. Physical analysis of the mechanical properties of pGNP/CFRP as well as thermal and electrical conductivity build a cohesive model of pGNP interactions across a wide range of conditions. Special attention in this dissertation was given to the performance of the pGNP/CFRP system at elevated temperatures, where the impacts on polymer behavior at elevated temperature provide key insights into pGNP interactions in the epoxy system.

Thorough attention was also paid to pGNP suspension formulation. Suspension formulation and spray performance were shown to have a significant impact on achieving pGNP dispersion in the interlaminar region which was necessary to achieve the targeted effects.

1.3.1. pGNP Characterization

pGNP was characterized to develop an understanding of how pGNP properties interact with the CFRP composite system and to provide a reference to other studies which use GNP. GNP vary widely in properties depending on the properties of the precursor graphite material and the exfoliation process used for production [12]. Biomass feedstocks typically carbonize into amorphous, hard carbons which are dominated by sp3 bonding [62]. Detailed analysis of GNP properties is essential for both plant and mineral based GNP to be able to compare nanomaterials between studies as well as to understand the interactions between the GNP and the composite system. An additional factor which is considered in this dissertation, which is underexamined in other literature, is the energy and environmental impact of pGNP production and cradle-to-gate lifecycle assessment.

In order to quantify the properties of the pGNP material, several methods were used. Raman spectroscopy was used to confirm the graphitic nature of the sample and assess the level of disorder. Scanning Electron Microscopy (SEM) was used to determine the range of lateral platelet sizes. Transmission Electron Microscopy (TEM) was used to confirm the layered particle morphology and to survey the layers in the particles. X-ray Photoelectron Spectroscopy (XPS) was used to determine the chemical species present and the bond structure on the surface of the platelets.

1.3.2. Spray Suspension Formulation

The formulation of an effective pGNP spray suspension was studied to develop an understanding of how selection of suspension components affects interlaminar pGNP dispersion. Suspension components do not impact the pGNP/CFRP system, but multiple secondary characteristics are important for developing a successful suspension. Particle loading in the suspension is important for delivering effective interlaminar coatings without excessive spraying. Wetting of the surface and rapid drying are important for producing a uniform coating without spotting or agglomeration. Suspension viscosity is important, shear thinning is preferable for spray formulations where low viscosity at high shear rates improves spraying performance while high viscosity at lower shear rates prevents sagging of the sprayed surface and improves long term suspension stability [63,64]. Cost and environmental impacts are also considered.

Water, alcohol, and acetone solvents were investigated along with carboxymethylcellulose (CMC) and sodium dodecyl sulfate (SDS) as dispersion aides. Loading of suspended pGNP in the suspension was evaluated by measuring the suspended solids 48 hours after mixing. pGNP dispersibility in investigated solvents was compared to conventional graphenes from mineral and synthetic graphite sources. Surface energy of the suspension on prepreg substrates was evaluated through contact angle measurement using the sessile drop method. Viscosity was measured to evaluate the impacts of dispersion aides at shear rates from 1-1000 s^{-1}. Finally, test surfaces were sprayed, comparing the optimized suspension to a simple pGNP/water suspension to observe the applied coating.

1.3.3. Curing Kinetics

The effects of pGNP interlaminar addition on CFRP-prepreg cure kinetics were studied to develop an understanding of how pGNP properties impact the chemical and thermal properties of the cure cycle. The expected impacts of pGNP thermal conductivity and chemical interaction with the curing polymer were expected to provide a significant change to the cure kinetics of the pGNP/CFRP system. Significant temperature fluctuations and changes in curing time have a crucial impact on the design of pGNP/CFRP composites. As there are various factors that can potentially affect the curing kinetics, multiple techniques are utilized for characterization. The heat flux in pGNP composites is measured using Dynamic Scanning Calorimetry (DSC) in comparison to neat composites to determine the rates of curing reactions. To assess the impact of pGNP addition on the bond structure of the cured composite, Raman Spectroscopy is employed to measure the cured bond structure as compared with a neat resin. Because temperature evolution in the center of thick composite sections is a product of both through thickness conductivity and heat of reaction, the temperature during curing is measured using a thermocouple probe to provide direct measurement of the impacts of interlaminar pGNP addition. The specific gravity of cured composites is measured at increasing pGNP loadings to evaluate void formation and its impacts on temperature evolution during curing.

1.3.4. Mechanical Characterization

The mechanical properties of the pGNP/CFRP system were studied to quantify the impacts of pGNP addition and to develop an understanding of pGNP interaction in the interlaminar region of the CFRP composite system. Investigations on the reenforcing properties of GNP are well studied [25–30], as is work demonstrating the effectiveness of GNP in improving the thermal stability of composite materials [31–33] examinations of the mechanical benefits of GNP at elevated temperature have been limited [39]. It is the aim of this dissertation to explore these benefits and to use the performance at multiple temperatures to describe the interactions of pGNP with the composite system.

Thermo-mechanical characterization of viscoelastic properties was performed using Dynamic Mechanical Analysis (DMA), showing the storage and loss modulus of the composite when heated past the glass transition temperature (T_G). The impacts of pGNP addition on the flexural modulus and strength of the composite were measured using flexural beam testing. Interlaminar shear strength (ILSS) was measured using short beam testing. Mode I (opening mode) fracture was evaluated using Double Cantilever Beam

(DCB) testing and the fractured surfaces were measured using fracture surface micrography to quantify mechanisms of fracture toughness improvement. Mode II (sliding mode) fracture was measured using End Notch Flexure (ENF) testing. The examination of fracture modes with stable crack growth (Mode I) and unstable crack growth (Mode II) gives particular impacts into the detailed interactions between pGNP and the composite system with regards to matrix plasticity and the damage process zone. Measurements were performed at ambient (20ºC) and elevated temperatures (90ºC).

1.3.5. Thermoelectrical Characterization

The thermal and electrical conductivity of the pGNP/CFRP system were studied to quantify the impacts of pGNP addition and to identify potential uses for the multifunctionality of pGNP treated composites. Enhancing thermal and electrical conductivity is beneficial as it broadens the scope of applications for composite parts, allowing them to function effectively under a wider range of conditions. Measurements of conductivity were made on unidirectional composite cubes, which allowed for the isolation of conductivity in the fiber direction (1), perpendicular to the fiber direction (2), and in the out-of-plane direction across the composite thickness (3). The Kelvin four-point measuring technique was employed to measure electrical conductivity. This approach involves using distinct pairs of electrodes for current delivery and voltage sensing. This method is particularly beneficial for measuring low resistance values since separating the current and voltage electrodes removes any lead and contact resistance that could affect the measurement. Thermal conductivity was measured using a two-sensor heat flux measurement between a heated and cooled plate at a constant power. Both conductivity measurements were conducted at 30ºC, 50ºC, 70ºC, and 90ºC to examine impacts on temperature on the composite conductivity.

1.3.6. Scope of Dissertation

The targets of this work are multifold. First, it is the goal of this work to show a more detailed description of graphene/polymer interaction and to highlight how a combination of chemical, mechanical, electrical, and thermal analysis is useful in this aim. Additionally, pGNP will be introduced as a more available, lower cost pathway to conventional graphene production. The mechanical and multifunctional benefits of pGNP application will be detailed. Spray application will be presented as a means of nanoparticle application with benefits over other methods. Finally, the roots of particle agglomeration in graphene/surface interactions which are frequently attributed to difficulty in graphene utilization will be examined.

Chapter 2 provides background for the work of this dissertation. It describes graphene as a material, the properties of graphene which are relevant to the scope of this work, the means by which graphene has previously been produced, and the environmental impact of graphene production and utilization. Chapter 2 also describes the state of graphene use in composite materials, difficulties in utilization which have been published, and the potential for future applications.

Chapter 3 provides background on the materials and methods used in this dissertation. Information is given on key materials used, including points of purchase and material specifications. Details for suspension formulation and composite fabrication are also included in this section. The methods of characterization are described with a description of the high temperature heating chamber used in fracture and conductivity analysis.

Chapter 4 aims to provide a thorough characterization of pGNP which is key in both understanding the similarities and differences pGNP has when compared to other graphene materials as well as characterizing the behaviors observed in subsequent chapters. pGNP production and life cycle assessment are given to show the environmental impact of pGNP production and use. pGNP characterization gives a thorough analysis of the particle size, morphology, chemical composition, and functionality.

Chapter 5 aims to provide a clear description of the key factors in designing a graphene suspension for spray application, particle dispersion, surface energy, and viscosity, as well as cost and chemical compatibility. The impacts of solvent choice and suspension additives are evaluated for each of the above properties, and an optimal suspension formula is tested in spray application.

Chapter 6 investigates the impact of interlaminar pGNP addition on the curing kinetics of the CFRP system with the goal of characterizing chemical interaction with the curing epoxy matrix. Differential scanning calorimetry directly measures the impact of pGNP addition to energy flow during curing, Raman spectroscopy analyzes the impact to the epoxy bond structure with pGNP after curing, and the measure of temperature evolution inside a thick composite during curing shows the impact of pGNP addition in a practical application.

Chapter 7 examines the mechanical performance of the pGNP/CFRP system, with a focus on examining changes at elevated temperature as a means of understanding nanoparticle/matrix interactions. Dynamic Mechanical analysis examines the flexural strength of the pGNP/CFRP system across a range of temperatures and provides detail on how pGNP impacts polymer chain movement. Flexural beam testing measures the improvement of interlaminar pGNP on the strength and modulus of CFRP. Short beam testing measured interlaminar shear strength, a property of the load transfer between plies in the interlaminar region. Mode I and II fracture testing highlights the impacts of pGNP on fracture—a key failure mode for composites—which demonstrates the mechanisms of reinforcement as developed in previous chapters.

Chapter 8 examines the multifunctional properties of pGNP/CFRP—specifically electrical and thermal conductivity—with a focus on relating conductivity to the particle matrix interactions as developed in previous chapters. Electrical and thermal conductivity are examined at ambient and elevated temperatures.

Chapter 9 describes ongoing work which aims to apply the principles developed in the previous chapters to a new material system. Glass fiber/PA6 organosheet is used as a composite system to highlight the differences in application with both fiber and matrix. The specific challenges of the GF/PA6 system are discussed, the suspension and spray formulation steps are repeated and a pGNP spray is applied to organosheet panels. Surface conductivity is measured.

Chapter 10 summarizes the conclusions of this work, describes ongoing work, and makes recommendations for future research.

CHAPTER 2

BACKGROUND OF THE STUDY

This section provides background for the work of this dissertation. Graphene is described, along with its history, unique structure, and the different graphene materials which are commonly used. Relevant properties of graphene are illustrated and compared to similar nanomaterials. Past work utilizing graphene in composites is summarized, with a focus on the mechanical and multifunctional properties, methods of application, difficulties in utilization, and the potential for future applications.

2.1.Graphene Background

Graphene was first isolated and characterized in 2004 at the University of Manchester, UK by Andre Geim and Konstantin Novoselov, who would be awarded the Nobel Prize in Physics in 2010 for their work [6]. While graphene refers to a monolayer of carbon atoms, the term has expanded to describe a family of materials including mono-layer or "pristine" graphene to multilayer graphene nanoplatelets (GNP), graphene oxides (GO) which are derived from graphene and have a distinct structure and chemistry, and reduced graphene oxides (rGO) [65]. Graphene materials are divided into two categories: "bottom up" production which utilizes a chemical vapor deposition (CVD) process to deposit carbon atoms on a metal substrate and "top down" production which uses a graphite feedstock material that is exfoliated using one of several methods—chemical, thermal, or physical—to separate the stacked carbon layers [6,65]. Over 40 commercial areas have been identified where graphene is expected to have a significant impact, including structural materials, smart materials, electronics, thermal transfer, and lightweighting [65]. With such variation in materials and applications, it is important to clearly define graphene's properties and potential applications.

2.1.1. Graphene Properties

Orbital hybridization is the concept of mixing atomic orbitals to form new hybrid orbitals in order to form chemical bonds [66]. Carbon, with four valence electrons, has one electron in the s-orbital and three electrons in p-orbitals which can form bonds with up to four different atoms. The names for these hybrid orbitals, sp, sp2, and sp3, refer to the ratio of mixing of the two atomic orbitals, sp being an equal mixing of the s- and p-orbitals, while sp3 has 75% of the p-orbital characteristic and 25% of the s-orbital characteristic. In sp hybridization, carbon atoms form 180° bonds as in molecules such as acetylene (C_2H_2), where the carbon atoms are bonded to each other via a triple bond. In sp3 bonding, carbon atoms have four orbitals arranged tetrahedrally with a bond angle of 109.5 degrees, such as four hydrogen atoms in methane (CH_4), with other carbon atoms in a diamond like structure, or other organic molecules. The absence of unhybridized p-orbitals in sp3 hybridization makes it less likely for molecules to form pi bonds or participate in conjugation, however sp3 hybridization can result in greater steric hindrance and less reactivity due to the lack of available p-orbitals for pi bonding [66]. The different carbon hybrid orbitals and the corresponding carbon structures are shown in Figure 1.

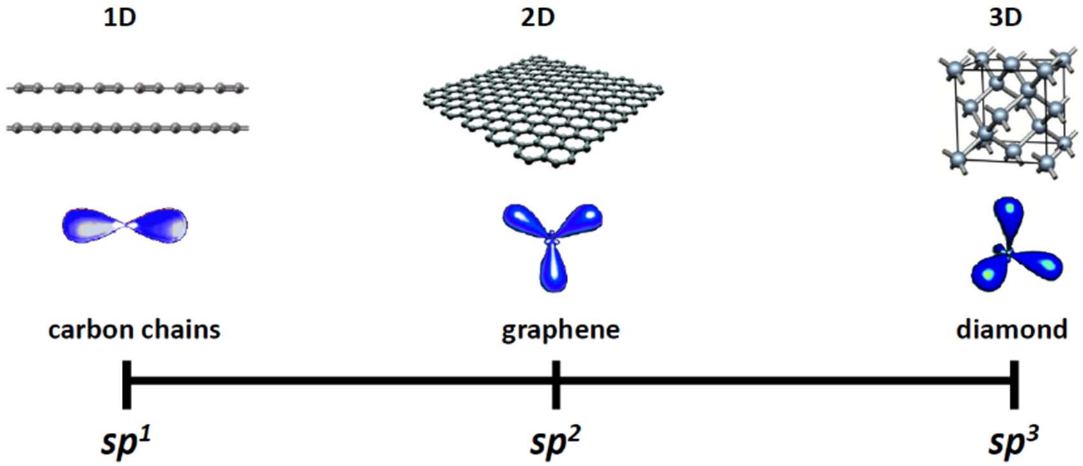

Figure 1. Carbon hybrid orbitals and the corresponding crystal structures [67].

In sp2 bonding, carbon atoms have three hybrid orbitals and one unhybridized p-orbital, which can overlap with the p-orbitals of other atoms to form pi bonds. The combination of overlapping p-orbitals from adjacent carbon atoms creates a delocalized pi-electron system that spans the entire molecule. In benzene (C_6H_6), the simplest aromatic molecule, each carbon atom is bonded to two other carbon atoms via sp2 hybrid orbitals and one hydrogen atom via a sigma bond. The remaining p-orbital of each carbon atom overlaps with the p-orbitals of the adjacent carbon atoms to form three pi bonds that are delocalized across the entire ring structure. This results in a continuous ring of overlapping pi-orbitals, which makes benzene highly stable and resistant to chemical reactions. This delocalized system of pi-electrons is responsible for the characteristic properties of molecules that exhibit sp2 bonding, such as planarity and aromaticity as well as electrical conductivity, thermal resistance, and strength [8–10]. It is because graphene is a large molecule composed of a crystalline network of sp2 bonded carbon atoms that it has such unique properties which are desired in research and commercial applications. Because the carbon atoms in GO have been oxidized, the hybrid sp2 bonds have been converted to sp3 bonds, removing the delocalized electrons and many of the properties of graphene. This is why GO acts as an insulator rather than a conductor. Other carbon materials may have a combination of sp2 and sp3 bonding, such as soot and carbon black [68] and biomass charcoals [62], but they lack the large-scale aromatic structure which imparts the properties graphene is known for.

Other carbon nanomaterials, including Carbon Nanotubes (CNT) and fullerenes possess similar sp2 structure to graphene, but have a different morphology. CNT consist of long tubes of sp2 carbons, giving them a similar high aspect ratio in one dimension. As such, there is less interfacial area for bonding with a matrix and creating conductive pathways through a composite [69]. Fullerenes are small spheres of aromatic carbons, sometimes referred to as 0D carbons [6] The lack of significant aspect ratio limits fullerenes applications in composite materials.

The physical dimensions of GNP are important to understanding their physical properties and interface with material systems. A single layer of graphene has a thickness of 0.335 nm, and a multilayer graphene will have a thickness that is roughly 0.335 nm times the number of layers, on the order of 0.3-10 nm. Lateral dimensions on the order of hundreds or thousands of nanometers [21,69]. The aspect ratio of GNP has been shown to affect the interlock between GNP and the matrix [69]. The exceptionally high aspect ratio and single or multiple atom thickness gives GNP exceptionally high specific surface area, ~2590 m^2/g for monolayer graphene [1].

Surface functionality is another key property of graphene materials. Pristine graphene is noteworthy for having a unique surface structure which is primarily interactive through Van der Waals forces with other aromatic structures and other graphenes in particular [1]. Impurities in the graphene surface, in the form of Surface Functional Groups (SFG) add chemical interactions with other chemical structures. SFG refers to specific chemical groups or moieties that are present on the surface of a material. These groups can play a critical role in determining the chemical and physical properties of the surface, including its reactivity, wettability, and adhesion. SFG which are common on carbon surfaces include hydroxyl (–OH), carboxyl (-COOH), carbonyl (–C=O), epoxide (C–O–C), carbonate ($–CO_3$), alkyl (C–H), and silane (Si–H) [70,71], although many more are possible with chemical functionalization. The high surface area of GNP, and unique aromatic properties result in a high impact of surface functionalization.

2.1.2. Graphene Enhanced Composites

GNP have been studied extensively for impacts to composite material systems with a range of results. Studies have focused on enhancing the mechanical properties or conductivity of composites but rarely are both impacts considered, or the relationship between them.

Very small loadings of graphene have shown mechanical improvements in composite systems, with fracture toughness showing the greatest relative improvements. A 2009 study by Rafiee, et al. compared the impacts of GNP and CNT addition at 0.1% w/w loading of graphene in bisphenol-A epoxy, dispersed in epoxy using an acetone solvent replacement method. GNP provided improvements of 40%, 31% and 53% to tensile strength, modulus, and fracture toughness as compared to 3%, 14%, and 20% with carbon nanotubes [24]. A similar 2018 study by Adak, et al. tested a loading of 0.2% w/w GO, which showed improvements of ~34%, 20%, 83%, and 55% to tensile strength, modulus, toughness, and flexural strength, respectively [72]. Brushed on graphene nanoparticles have shown improvements in a 2015 study by Kamar, et al. where glass fibers were coated in a GNP/epoxy mixture dispersed in alcohol before CFRP composite fabrication. Mode I fracture toughness was increased 25% with a 0.25% (w/w) of particles [26]. Ning, et al, showed that use of a GO/epoxy interleaf in CRFP showed an optimal loading of 2 g/m^2 (0.5% w/w) which enhanced Mode I toughness by 170.8%. The interleave was produced by dispersing GO in N,N-dimethyl formaldehyde before solvent exchange with epoxy resin to produce a GO/epoxy paste which was applied to the interlaminar fracture region [25]. In a similar interleave study, by Zhao, et al, GO was polymerized with polyamide at 1% w/w in an in-situ process provided 80.6% and 36.2% under Mode I and Mode II deformation, respectively at a loading of (0.5% graphene oxide w/w) [27]. In a 2013 study, Shadlou compared the behavior of spherical nanodiamond, CNT, and GNP and observed 13% reduction in mode-II fracture toughness of epoxy resin reinforced with 0.5 wt% graphite oxide (GO) [73]. Similar 13% decreases in Mode II toughness were observed by Ahmadi-Moghadam in 2013, which was attributed to stress imbalance between the matrix and GNP [69]. A study by Kumar and Roy in 2018 on fracture using hydrogen passivated graphene showed improvements of ~48% in Mode I toughness on initiation and ~158% in Mode II, owing in part to improved Van Der Waals interactions of the passivated graphene [50]. While Mode I fracture results are generally improved with GNP addition, Mode II results appear split, with untreated GNP and GO decreasing the fracture toughness while GNP with surface modifications to the particle/matrix interfacial energy increase Mode II toughness.

Significant study has also gone into the impacts of GNP addition on composite conductivity. In metals, electrical and thermal conduction are modeled with the “Free Electron Model,” in which electrons are assumed to behave like a gas of free particles, and the electrical conductivity of the material is determined by collisions with the metal ions in the metal lattice. Collisions in this model are proportional to the mean free path between metal ions, on the order of 0.04 μm for a conductive metal such as copper [74]. The “Mean Free Path Model,” is used to describe electron transport in graphene. In this model, the mean free path is the average distance that an electron can travel before colliding with impurities, defects, or other scattering mechanisms. The mean free path model provides a better description of electron transport in graphene because it takes into account the effects of impurities and defects, which have a significant impact on electron scattering in graphene [75,76] and because electrons in graphene are in the ballistic transport regime, which occurs when the mean free path is larger than the particle dimensions. In this regime, electrons can travel across the particle without significant scattering, resulting in a high conductivity [6]. This unique behavior is owed to the shared electrons in the aromatic structure of the sp2 lattice of GNP with a mean free path of 100 μm [55] or longer for pristine graphene [75,76]. Pristine graphene has a conductivity of up to 100 MS/m and in macroscopic application graphene has shown conductivity of 70-80 MS/m [56]. More important for many applications, the low density of graphene (0.3 g/cm^3) results in a theoretical specific electrical conductivity of 333.3 MS·cm^3/g·m. When compared to copper, with a conductivity of 70 MS/m and a density of 8.93 g/cm^3, or aluminum with a density of 2.69 g/cm^3 and conductivity of ~37 MS/m, graphene has a specific electrical conductivity 50 times higher than copper and 23 times higher than aluminum [57]. Carbon nanotubes offer substantially less potential for conductivity, with an electrical conductivity ranging from 0.1-1.0 MS/m and a density of 1.4 g/cm^3 [77], leading to specific electrical conductivities of 0.071-0.71 MS·cm^3/g·m, substantially less than graphene, aluminum, and copper.

Thermal Conductivity (TC) describes the ability of a material to conduct heat which—for nonmetals—is due to the transmission of phonons through the molecular lattice structure [78]. Phonons are quantized units of lattice vibrations in a material that act as carriers in heat transport. TC of monolayer graphene has been reported to be very large, up to 5300 W/m·°K at room temperature compared with diamond (2000

W/m·°K) or copper (400 W/m·°K) [79]. As with EC, the high TC of graphene is a result of exceptionally long mean free paths (although for phonon transport rather than electron transport) while TC of the conventional metals is mainly given by free electrons [79]. The differences between EC and TC in GNP enhanced composites relate to the difference between electron and phonon behavior. While electrons have a tunneling potential through resistive epoxy [80], phonons behave acoustically and TC in a multicomponent system can be impacted by phonon scattering at the interphase between composite constituents [81]. Polymer materials are disordered on a molecular scale, resulting in strong phonon scattering at all temperatures and low TC values for plastics. The phonon mean free path is approximately constant with temperature and as such the TC is constant with increasing temperature [81]. However, in composite materials the TC is a result of the combined thermal conductivities of the constituent components [9] and in the case of anisotropic fiber composites, the TC will be likewise anisotropic [82]. While GNP have an exceptionally high theoretical TC, low loading thresholds limit the potential effectiveness of graphene in polymer systems [9,83]. GNP are superior to other carbon nanoparticles in enhancing TC in polymer systems because their large surface area promotes efficient phonon transfer between the matrix and the nanoparticle [32].

GNP have shown significant improvements to the TC of epoxy composites, at both low and high loadings. Yu, et al. in 2007 showed that a 5% (v/v) loading of graphene performed as well as 50-70% (v/v) loadings of alumina or silica [31]. A 2020 study by Zhao, et al. with carbon fiber reinforced polyamide 4,6 have shown increases in thermal and electrical conductivity with GNP addition which have varied between in-plane and through thickness measurements, owing to percolation between the GNP and the carbon fibers. In plane thermal conductivity was increased 213% and through thickness conductivity was increased 526% at 5% (w/w) loading of graphene, but at these loadings all measured mechanical properties were reduced substantially [82]. GNP have increased the decomposition temperatures of thermoplastic materials, but the effect is concentration dependent [84,85]. Garcia, et al. showed in 2021 that, at loadings up to 2% (w/w), GNP retard the decomposition of the polymer, preventing structural breakdown. Loadings of as little as 0.1% (w/w) have increased the thermal stability of polypropylene by 13 °C [85]. Liu, et al showed that, at higher loadings, GNP increase the thermal conductivity of the composite, accelerating thermal decomposition [33]. A study of graphene oxide in thermoset polyimide at loadings of 1-5% by Liu, et al. in 2012 showed improvements in thermal stability due to the trapping of the polymer moieties in nano-filler networks.

Improvements were optimized at 3% loading, with the temperature at 5% mass loss increasing from 480ºC to 530ºC [86]. A 2018 Simulation of T_G by Singh and Sharma modeled epoxy resin and graphene fillers functionalized with COOH and NH_2 functional groups using molecular dynamics and found increases of T_G of 40ºC and 45ºC, respectively, due to covalent bonding between functional groups and polymer chains [87]. Another study by Yu, et al. in 2016 found that a 1% loading of graphene oxide, functionalized with diamine in a bisphenol epoxy improved T_G of the cured resin by 23ºC due to an increase in crosslink density from 0.028 to 0.069 mol/cm^3. The higher crosslink density also resulted in an increase in tensile strength from 87.4 MPa to 110.3 MPa at ambient temperatures, but higher temperatures were not studied [88].

2.1.3. Graphene Environmental Impact

One issue which has not been broadly discussed is the carbon emissions and environmental impact of graphene production. The 2021 United Nations Intergovernmental Panel on Climate Change (IPCC) report reaffirms that human-induced climate change is widespread and intensifying, with several trends likely irreversible. The IPCC projections indicate that immediate, ambitious, and equally widespread reductions in greenhouse emissions are necessary to limit global warming to the most optimistic 1.0°C–1.8°C increase in average temperatures [89]. Graphene offers several opportunities for reducing carbon emissions in a wide variety of production sectors, both by means of offsetting or replacing conventional material fillers or by improving material performance to reduce the volume of materials which need to be produced. By way of example, concrete is a widely used construction material and concrete production is one of the largest global emitters of CO_2, at 8% of total emissions [90]. A cement composite produced with recycled aggregates along with 0.2% w/w GO reduced the need for natural aggregates in the composite while increasing compressive and flexural strength by 19.2% and 47.5%, respectively. The GO addition resulted in a reduction of CO_2 emission in the lifecycle of the aggregate of 6.7%, and the increase in strength [91]. If GNP addition results in a 5% reduction of Portland cement usage, the impact of the concrete mix on global warming can be reduced by 21% [92]. Similarly, an analysis of emission in tire production found that the production of carbon black made up the largest share of carbon emissions for tire production. Utilization of graphene to replace carbon black can result in a reduction of CO_2 emissions of 23.46% [93]. However, in some applications there is negligible benefit to GNP addition regarding lifecycle carbon emissions. In one study a 5.8% loading of GNPs were added to an epoxy matrix for improvements to thermal conductivity. The thermal conductivity was increased from 0.2 W/m·°K to 1.0 W/m·°K, but the energy required to produce GNP added an additional energy cost to the composite of 187 MJ, resulting in a total energy cost to produce of 303 MJ/kg-composite. GNP addition in this case resulted in an increase of energy usage of 161% at a loading of 5.8% [12]. The low loadings of graphene present substantial opportunities to reduce the greenhouse emissions when offsetting other carbon intensive fillers, but the high energy cost of GNP production can still be a subject of concern. The energy costs of sustainable, plant-based GNP are presented herein in contrast to conventional routes of GNP manufacture.

GNP produced from mineral graphite or through chemical vapor deposition have a wide range of environmental impacts depending on production methods. Production of carbon nanomaterials is often much more energy intensive than the production of conventional materials, but lower loadings and substantial system improvements often result in a net improvement of energy usage [13]. Mineral GNPs are produced from mined graphite of a high grade, predominantly from Sri Lanka. Emissions rates for mining and transportation are on the order of 0.05-0.5 kg-CO_2/kg graphite and are minimal when compared with the impacts of GNP production. These values are included in one cited Life Cycle Assessment (LCA) [12] but are neglected in others [13,14].

The chemical exfoliation of natural and synthetic graphite has several possible variations in process, with the selection of acid and the amount of acid used having the largest impact [13]. Most routes are derived from the Hummers Method, which oxidizes graphite in a strong acid to produce GO platelets which can be used in their oxidized form or reduced to produce rGO [14]. Processes utilizing sulfuric acid have emissions rates ranging from 46-280 kg-CO_2/kg-GO while processes using nitric acid have ranges from 107-110 kg-CO_2/kg-GO. Reduction of the GO to rGO increases CO_2 emissions and also varies by method. Chemical reduction of GO using an agent such as hydrazine has a net emission value of 100 kg-CO_2/kg-rGO. Thermal reduction by heating the GO requires less energy but has a decrease in yield since some GO is lost in emitted CO_2, the net emission value is 40 kg- CO_2/kg-rGO [15]. When combined with production values, the range of possible cradle-to-gate emissions values from 86-220 kg-CO_2/kg-rGO. Commercial production using renewable energy production could reduce these values to 44-79 kg-CO_2/kg-rGO [5]. GO and rGO production also presents several substantial environmental risks because of chemicals used in the process. Hydrazine has a toxicological risk for humans and animals who are exposed to it [94]. NOx, which is produced in the oxidative exfoliation of graphene is also a significant concern for both human exposure and environmental impact and sulfuric acid used in oxidation is a potential water contaminant [14].

Exfoliation of mineral graphite to produce graphene through ultrasonication utilizes high frequency, sonic energy transmitted through a solvent to mechanically exfoliate GNPs. The energy utilization of ~500 MJ/kg is approximately half as much as for chemical exfoliation and could be reduced to as little as 70 MJ/kg with the use of decarbonized electricity but the use of hazardous solvents such as diethyl ether have significant impacts on health and environmental safety [15]. Thermal exfoliation of graphene involves soaking graphite in sulfuric and nitric acid to form a sulfate-graphite intercalation. This intercalated material is heated in stages, in a furnace and with microwaves to expand the graphite into GNP stacks which can be separated by pulverization. Electrical usage for microwave heating makes up greater than 90% of the energy usage and environmental impact [12].

2.2. GNP Composite Manufacturing

2.2.1. Nanofillers in Matrix/RTM Limitations

Despite promising early results, graphene remains difficult to implement. Graphene dispersion is essential, as well as good graphene/polymer interaction, however graphene loading and particle interaction can be too high, increasing agglomeration and reducing conductivity [8,95]. The resin flow in commonly used Resin Transfer Molding (RTM) and Vacuum Assisted Resin Transfer Molding (VARTM) infusion manufacturing processes can have detrimental effects of nanoparticle diffusion. Dispersion of nanoparticles directly into resin prior to infusion has several drawbacks. First, the fiber reinforcement acts as a filter to the nanoparticles as resin flows, creating regions of detrimentally high and low particle density [96]. Second—even at small loadings—nanomaterials increase resin viscosity substantially, resulting in difficult processing in RTM. When uniform nanoparticle distribution can be achieved, then noncritical regions as well as critical regions are reinforced equally resulting in a higher than necessary cost [60].

Nanoparticle spray application onto fiber surfaces before resin infusion has been investigated. In 2013, Shan, et al. incorporated sprayed multiwall carbon nanotubes (MWCNT) into a VARTM by spraying the MWCNT directly onto a carbon fiber fabric and then spraying a high viscosity epoxy to adhere the MWCNT to the fiber surface. Fracture strength was measured with and without the epoxy adhesive spray and it was found that with MWCNT loading at 0.6% w/w, coupled with an adhesive spray, the fracture toughness was improved 24%. However, with MWCNT spray with resin integrated or MWCNT spray following a resin spray, all mechanical properties were reduced due to MWCNT displacement and agglomeration during resin infusion. Scanning electron microscopy (SEM) showed nanoparticle agglomeration in the MWCNT samples where MWCNT, ethanol, and resin were sprayed together, and where MWCNT/ethanol were sprayed after a resin coating, but not where MWCNT/ethanol were sprayed and followed with a resin spray. Miscibility between the ethanol and resin was important to effectiveness of the spray sequence [97]. The migration of nanoparticles during infusion and the subsequent filtration by fibrous media was detailed by Zhang, et al. in 2017. Two plies of woven E-glass twill were infused with an epoxy with well dispersed graphene particles in a VARTM process with resin flow across the preform panels. Center line optical transmission was used to demonstrate that, as distance from the infusion point increases, the likelihood of graphene particles being filtered by the fiber preform increases, resulting in lower graphene loadings near the outlet. Similarly, measurements of electrical conductivity show the same filtration effect. Near the resin infusion point conductivities of 6-10 S/m are observed, but these decrease with increased distance from the infusion point until no improvement in electrical properties is observed [96].

2.2.2. *Spray Application*

Spray application of GNP and other CNP has shown substantial promise in improving fracture toughness in composites. In 2014, Almuhammadi, et al. measured the impact of functionalized multi-walled carbon nanotubes (MWCNTs) applied to a prepreg surface with respect to mode I fracture toughness, G_{IC}. MWCNTs were applied at 0.5% w/w by spray application in an ethanol suspension. Ethanol was chosen over water, acetone, and dichloromethane because of its high surface energy and low chemical interaction with the epoxy matrix. A 17% increase in fracture toughness was observed and SEM imaging showed that the improvement derived from the ability of the MWCNT to spread the damage through pullout, peeling and bridging of the particles, as well as from crack displacement from the 10 μm MWCNT rich region to MWCNT poor regions of the matrix. This indicates that the MWCNT are not fully utilized as a reinforcing agent due to crack displacement away from the reinforced regions [98]. A more dramatic improvement was obtained in 2015 by Zhang, et al. using a carbon nanotube (CNT)/methanol spray solution to deposit CNTs at 0.047% w/w onto a 2x2 twill carbon fiber/epoxy prepreg. The resulting composite showed a G_{IC} improvement of 50% [37]. The highest MWCNT reinforcement was found 2012 by Joshi and Dikshit, where MWCNTs were dispersed into an ethanol solution and sprayed onto woven carbon fiber/epoxy prepregs. The optimal loading was found to be 1.32 g/m^2, at which G_{IC} was improved by 79% and Mode II fracture, G_{IIC}, was improved by 140%. Higher loadings resulted in decreasing mechanical performance. Examination of the composites showed that the MWCNTs moved during curing from the spray surface into the fiber reinforced region, significantly increasing fiber bridging at optimal loading. Investigation of the surfaces with SEM showed that at higher loadings, MWCNTs did not disperse into the matrix, agglomerating on the fracture surface [7]. In 2019 MWCNTs and GNP were compared by Liu, et al. Both were applied to unidirectional carbon fiber prepregs with a $[0°]_{30}$ stacking sequence at 1 g/m^2 using an acetone solvent. G_{IC} values were improved 12.6% for MWCNTs and 101.5% for GNP. SEM analysis showed that GNP perpendicular to the fracture surface exhibit pullout from the matrix, resulting in a much higher G_{IC} than neat or MWCNT reinforcement [29]. In 2021, Leow, et al, investigated the spray application of interlaminar GNP carbon fiber reinforced PEEK composites to improve electrical conductivity for Lightning Strike Protection (LSP). Composites were prepared by spraying a 1.5% w/w graphene-water suspension onto CF/PEEK tapes before sets of 9 plies were molded to make test specimens. An interlaminar loading of 1.3% w/w GNP into CF-PEEK composites resulted in in-plane and through thickness electrical conductivity enhancement both of 1100% and 67.5% respectively [99].

2.3. Multifunctionality

Graphene has shown a very low percolation threshold for increasing conductivity in polymers [33]. A 0.38% loading of isocyanate treated graphene oxide in polyamide led to a conductivity increase of eight orders of magnitude, along with increasing the strength of the film [100]. A 2019 investigation of the anisotropic effects of GNP addition to carbon fiber reinforced plastic (CFRP) composites by Senis, et al. showed variance between EC and TC depending on fiber direction. A 6.3% v/v loading of GNP provided a 63% increase in transverse EC, while providing an over 300% improvement in the through thickness direction. Through thickness TC was reduced at low GNP loadings before improving by 8% at a 6.3% v/v loading, while transverse TC showed moderate decreases in conductivity 0.3% loading [101]. Another 2019 study by Imran and Shivakumar investigated the through thickness EC and TC of GNP/CRFP composites and showed improvements of 132% and 8% respectively [102]. Experiments by Senis, et al. in 2020 using electric fields to orient GNP have shown that thermal and electrical conductivity is impacted by GNP orientation as well, with aligned GNP providing 300% and 27% improvements to through thickness electrical and thermal conductivity as compared to 82% and 20% for unaligned GNP [48].

2.3.1. Lightning Strike Protection and EMI Shielding

Recently, researchers have begun exploring the potential of carbon nanomaterials for EMI shielding and LSP. In 2017, Zhang, et al, produced a thin, flexible coating made of pristine graphene which was applied to the surface of a CFRP laminate which was subjected to simulated lightning strike. It was found that the area and volume of damage in the coated laminates was reduced by 94% and 96%, respectively, as compared to untreated CRFP. Electromagnetic interference (EMI) shielding effectiveness was also measured and it was found that the graphene treated composites had a 49% increase in EMI shielding effectiveness at 12–18 GHz. The graphene film was made without binder, by filtering a solution of graphene flakes in water on a glass fiber filter. The graphene film was placed as a base layer against the aluminum mold in which subsequent prepreg layers were stacked. The graphene film had a conductivity of $2.14 \cdot 10^4$ S/m with thicknesses from 0.023-0.140 mm [103]. A similar, paper-based method was used by Han, et al., who prepared a carbon nanotube paper and bonded it to the surface of CRFP using three different adhesive layers, a pure epoxy adhesive layer, an insulating, boron nitride doped adhesive layer, and a conductive adhesive layer. The optimized LSP coating was composed of ~70 μm thick nanotube paper and ~200 μm thick insulating adhesive, which resulted in a weight reduction up to 30% compared to the commercial Cu LSP coating. In addition, the thin nanotube layer did not provide sufficient EMI shielding to prevent damage to onboard electronics as a result of EMI from lightning strike [104]. In 2018, Wang, et al. utilized a percolation assisted, resin film infusion to deposit reduced graphene oxide (rGO) onto the surface of a CFRP composite. In this method, filtration of GNP by fibrous media was utilized by sealing the fibrous preform using filter paper and sealant tape to form a confined region that prevented the transmission of rGO from the fibrous preform while also limiting the rGO flow along the thickness direction, causing rGO to accumulate on the CFRP surface. Surface conductivity was increased to $4.4 \cdot 10^4$ S/m from- the untreated $1.6 \cdot 10^3$ S/m. as well as improving thermal resistance, resulting in a substantial improvement for LSP as shown by post-strike mechanical testing. Residual strength after the simulated strike, measured by 3-point flexural testing, was reduced 23% in rGO treated composites, as opposed to 66% for the pristine sample [105]. This study is noteworthy as it takes advantage of the nanoparticle filtering by the fibrous media which is limiting nanoparticle use in RTM applications.

2.3.2. Structural Health Monitoring

Structural health monitoring (SHM) is the practice of detecting and quantifying damage in structures at an early stage as a means of preventing future, unexpected failure as well as reducing life cycle costs and aiding design [106]. As composite materials are used in increasing amounts, SHM for composite parts and systems becomes correspondingly more critical. Composite materials fail by complicated and interacting damage methods as compared to metal parts, and damage detection in composite parts is more complicated than in metal structures due to the anisotropy of the material, differences in matrix and fiber properties, and the possibility of layers of the composite to hide damage from visual inspection. Several techniques for SHM in composites have been investigated for in vivo health monitoring, primarily utilizing micro-scale semiconductor sensors [107–110]. However, the use of traditional sensors has several distinct drawbacks; the sensor must be local to the measured damage, installed sensors create discontinuity in the composite which can become a focal point for damage propagation, and integrated-circuit sensors require wiring and circuit boards in addition to their own construction, which adds complexity and weight to constructed parts. The intrinsic conductive properties of composite materials may supersede traditional sensors for SHM [35,111,112]. GNP is the leading candidate for advanced electronics because of its high carrier mobility and large saturation velocity in conjunction with its strength and flexibility [6]. GNP piezoresistivity has recently begun to be explored as a tool for SHM applications, in which small amounts of CNP additives are used to increase the conductivity of otherwise nonconductive matrix materials. When subjected to strain, the network of CNPs change conductivity, allowing for reversible in vivo strain measurement. Upon inception of microscopic damage to the matrix, permanent changes to electrical conductivity act as damage detectors in the composite. This has been shown with epoxy matrixes using fibers of CNT materials [113,114], as well as with interlaminar layers [35] and in fused, thermoplastic joints [36].

An application by Zhang, et al. utilized the conductivity of CNT for SHM in 2014. A methanol spray solution was used to deposit CNT at 0.047% w/w onto a 2x2 twill carbon fiber/epoxy prepreg. The resulting composite showed a 50% improvement in fracture toughness. Treating the ends of the composite beams with a silver loaded epoxy allowed for damage monitoring through changing resistance. CNT addition reduced the initial composite beam resistivity from 1.430 Ω to 0.984 Ω, but as damage propagates through crack extension, the beam resistance increases, allowing for active measurement of damage to the composite. In this application, very low CNM loading was chosen to prevent percolation and a high conductivity to maintain SHM resolution [37]. Higher loadings would provide much higher conductivity and likely higher mechanical reinforcement. In 2018, Kravchenko, et al. demonstrated the potential of a Buckypaper—formed from CNT—applied by frictional rolling in creating a thin layer on impregnated unidirectional glass fiber lamina. The sample exhibited reversible piezo-resistive behavior in the linear range of loading. When the sample was loaded past the linear range, the resistivity showed an immediate and irreversible increase corresponding to microscopic damage in the composite [35].

CHAPTER 3

METHODOLOGY

This section describes the materials and methods for producing pGNP spray suspensions and pGNP/CFRP composites as well as experimental methods used to characterize pGNP and pGNP treated composites. High temperature testing was used to compare the performance of pGNP/CFRP composites at elevated temperatures to compare with ambient performance as a means of gaining insight into pGNP interaction with the polymer composite system. pGNP characterization of particle size, morphology, surface functionality, and graphitization are necessary to compare the pGNP material used with other GNP in other studies, as well as to fully understand the mechanisms of interaction with the polymer systems. Measurements of particle loading, surface energy, and viscosity of the pGNP suspension inform the dispersion and effectiveness of the interlaminar coating. Utilizing a broad range of mechanical, thermal, and electrical characterization provides the necessary data to build an understanding of multiscale pGNP interactions with the composite system and the multifunctionality of the produced composites.

3.1.Materials

Carbon fiber/epoxy prepreg was purchased from Rock West Composites. The unidirectional prepreg was composed of a Toray T800S fiber (63% w/w) in an intermediate modulus epoxy with a 135 ºC cure temperature and T_G of 130 ± 10 °C. Graphene nanoplatelets were provided by the Carbon Research and Development Company in a 70 g/l suspension with water. Platelet thickness ranged from 3-20 layers (1-6 nm) with a lateral size from 300-1000 nm. The nanoplatelets contained both epoxide and carboxyl functional groups.

GNP for suspension testing was supplied by Kanodia Minerals & Chemical Co, India. GNP from mineral and synthetic graphite sources were supplied. Mineral graphene was specified at 94% fixed carbon, synthetic graphene was specified at 98% fixed carbon. Both were delivered as a powder sieved to -325 mesh or <44 microns. The supplied volume of mineral and synthetic GNP was only sufficient for dispersion testing, not interlaminar testing.

Sodium carboxymethyl cellulose was supplied by Sigma-Aldrich with an average molecular weight of ~250,000. Sodium dodecyl sulfate was supplied by Sigma-Aldrich at 98% purity.

3.1.1. Spray Formulation

A GNP spray was formulated using a water/pGNP dispersion, diluted with isopropyl alcohol and with carboxymethyl cellulose (CMC) and sodium dodecyl sulfate (SDS) as dispersion aides and viscosity modifiers. The pGNP used in this work was delivered as a 70 g/l suspension in water. As will be shown in detail in later chapters, water gives better pGNP loading in suspensions, but does not effectively wet the prepreg surface or dry quickly enough to work effectively. Isopropyl Alcohol (IPA) provides excellent surface wetting on the prepreg surface, as well as being highly volatile to promote fast, even drying but IPA has poorer dispersion characteristics for the pGNP. The additive CMC was used to provide several benefits to the pGNP spray formulation, principally as a binder to promote surface adhesion, while also improving viscosity and surface tension. Likewise, SDS was added principally as an anionic surfactant, but it also provides benefits to pGNP dispersion.

The 70 g/l pGNP water suspension was mixed thoroughly to ensure even particle distribution, and then mixed in equal volume with 91% IPA. This was placed in a high shear mixed set to a low speed to provide agitation. CMC and SLS were measured, targeting 1g/l and 5 g/l, respectively and mixed into the suspension gradually to prevent clumping. The suspension was mixed in the high shear mixer at high speed for ten minutes to fully integrate all the components.

3.1.2. Composite Fabrication with pGNP in Interlaminar Region by Spray Deposition

CF/epoxy prepreg sheets were treated with pGNP by spraying the prepared suspension through an airbrush onto the sheets by hand while controlling that distance between the airbrush and the prepreg sheet was about 0.2 m. To coat CF/epoxy prepreg sheets with pGNP, an initial weight was taken before the sheets were hung vertically. The pGNP spray suspension was applied using a Central Pneumatic 93506 airbrush using even, overlapping passes as shown in Figure 2-a. Light coatings were used in order to ensure uniformity and to prevent beading on the prepreg surface. Coatings higher than 1.1 g/m^2 were sprayed in multiple coats. Application rates were estimated by volumetric flow rate during application, precise pGNP loading was measured by weighing the sprayed sheets after sufficient drying. The coated surface (Figure 2-c) was slightly less reflective than the uncoated surface (Figure 2-b).

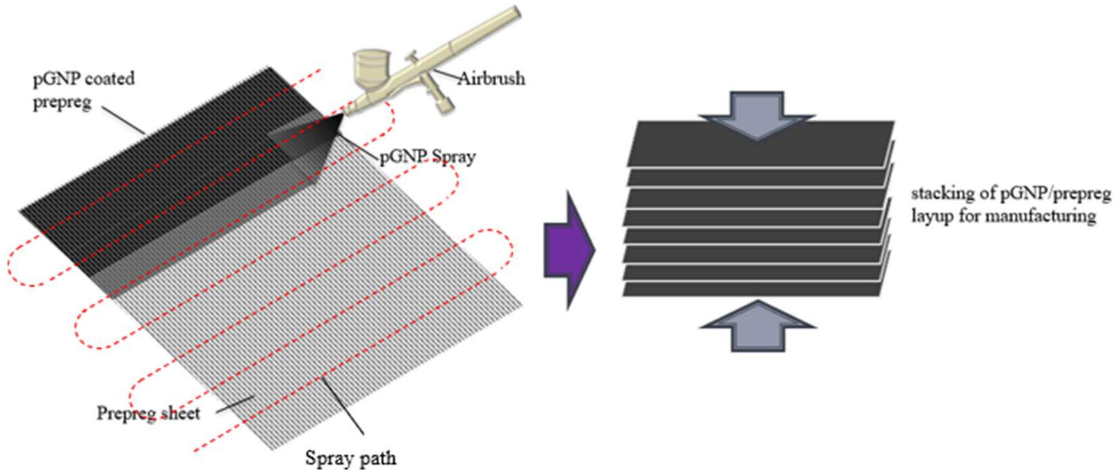

a.

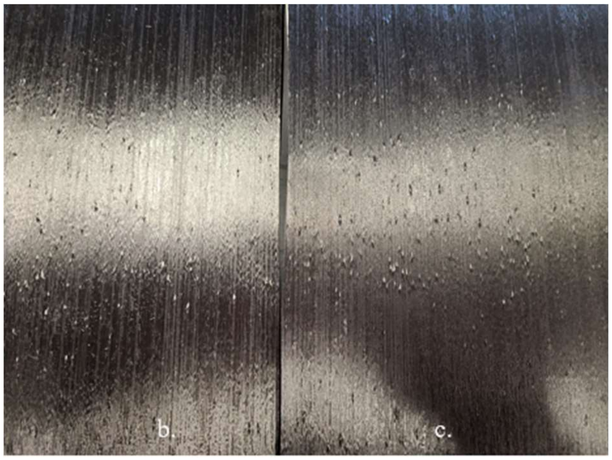

Figure 2. a) pGNP spray application; b) CF prepreg before spraying; c) CF prepreg with pGNP coating.

Coating uniformity was estimated using electrical resistance with a Cen-Tech p37772 digital multimeter, taking an average of 5 points on dried surfaces, at least 10 minutes after spraying. Electrical conductivity across the surface of the dry, uncured ply was measured using an ohmmeter with a resistance of 17 Ω/mm, spray with the GNP solution at 1.1 g/m^2 reduced this to 1.8-3 Ω/mm. Further exploration of this is warranted.

Samples for curing temperature, electrical and thermal conductivity were produced by stacking total of 168 5 cm x 5 cm plies with [0°] orientation to a total thickness of 2.5 cm. Larger prepreg sheets were sprayed before cutting into 5 cm x 5 cm plies and these plies were stacked with the pGNP sprayed surfaces laid against the untreated, paper backed surfaces with backing removed, providing interlaminar pGNP layers between each ply. A thermocouple was placed between plies 84 and 85, in the center of the sample to measure the heat reached internally.

3.2. Characterization

GNPs interface with polymers at both the molecular and macroscopic scale, resulting in multifunctionality of GNP nanocomposites in terms of effective thermal-electrical, mechanical, and viscoelastic properties and a broad selection of tests are required to fully characterize the complicated interactions. To that goal, properties were considered through the prism of pGNP/epoxy interactions. X-ray photoelectron spectroscopy gives a profile of pGNP structure and surface functionality, and TEM imaging gives particle morphology. Raman spectroscopy was used to examine both graphene bond structure and the impact of pGNP on molecular bond structure. Mechanical characterization included flexural testing, interlaminar shear strength using short beam testing, and Mode I and Mode II fracture toughness testing at ambient and elevated temperatures while thermo-mechanical characterization of viscoelastic properties was done using Dynamic Mechanical Analysis (DMA). Fracture surface micrography was used to quantify mechanisms of fracture toughness improvement. Investigation of thermal and electric conductivity indicates electron and phonon transport through the composite, pointing to interaction between the pGNP and the matrix. These methods present a comprehensive investigation of graphene induced improvements on multifunctional properties of CFRP at ambient and elevated temperature.

3.2.1. Elevated Temperature Testing

A custom made heated, convective air chamber was utilized to perform Short Beam, Mode I, Mode II, Thermal Conductivity, and Electrical Conductivity tests at elevated temperatures. The chamber, shown in Figure 3, was constructed using 2.5 cm of insulation on all sides with a glass window to allow for observation of tests. The internal dimensions were built to 40 cm x 40 cm x 60 cm.

Figure 3. The convective heating chamber where high temperature testing was performed.

Temperature was measured using a single, k-type thermocouple installed with the junction near the test location and controlled using a Yokogawa UT150 temperature controller. Heat was supplied through forced air over a 1500-Watt resistive heating element. Load and displacement sensing elements were located out of the heated chamber so as not to influence measurements. For tests at elevated temperature, beams were pre-heated to 90°C for at least 30 minutes and held at 90°C through the duration of the test. This ensured that the material was uniformly heated during crack extension. Duration of preheating was selected to reach the thermal equilibrium inside of the chamber, which was confirmed with the thermocouples placed near the sample.

3.2.2. Microscopy and Spectroscopy

Scanning Electron Microscopy (SEM) was performed using a Zeiss Supra Microscope with 30 µm aperture and 5 kV accelerating voltage with a minimum of 200 individual particles measured to provide a statistically significant distribution of particle lateral size. The image analysis was carried out using SPIP™ (Version 6.7.9). The lateral size of each particle was determined by measuring the length (longest edge-to-edge distance) and width (a perpendicular bisector of the length) of the particles and calculating the mean value of the two. Transmission Electron Microscopy (TEM) was performed using an FEI Talos F200X with 0.16 nm resolution and 200 keV accelerating voltage.

X-ray photoelectron spectroscopy (XPS) was carried out in ultra-high vacuum using a Kratos Axis Ultra DLD instrument. A monochromatic aluminum X-ray source was operated at 75 W (15 kV, 5 mA) emission. Each analysis area was approximately 700 μm × 300 μm, and the depth of information in XPS is less than 10 nm.

Raman spectroscopy is used to provide information on the bond structure of chemicals using the inelastic scattering of photons from a monochromatic laser source. The energy shift in the scattered photons is measured and is translated into a spectrum which provides information on the chemical bond structure of the sample material. Raman spectra were taken using Horiba XploRA™ PLUS with a 532 nm laser source, 100x magnification, and 600 g/mm grating. Data was collected in LabSpec6. Raman spectroscopy was used to measure the impact of pGNP addition on the cured epoxy resin.

3.2.3. Viscosity Measurements

Viscosity of the pGNP suspensions was measured using an Anton Paar MCR 302 Rheometer with a T-PTD 200 tribology cell and a 25 mm parallel plate testing head with a 1 mm test height at 25 °C. Viscosity was measured across a range of shear rates, from 1-1000 s^{-1} to examine both the impact of SDS and CMC added to pGNP suspensions, and potential non-Newtonian behaviors of the suspension. Shear thinning is preferable for spray formulations where low viscosity at high shear rates improves spraying performance while low viscosity at lower shear rates prevents sagging of the sprayed surface and improves long term suspension stability [63,64].

3.2.4. Contact Angle Measurements

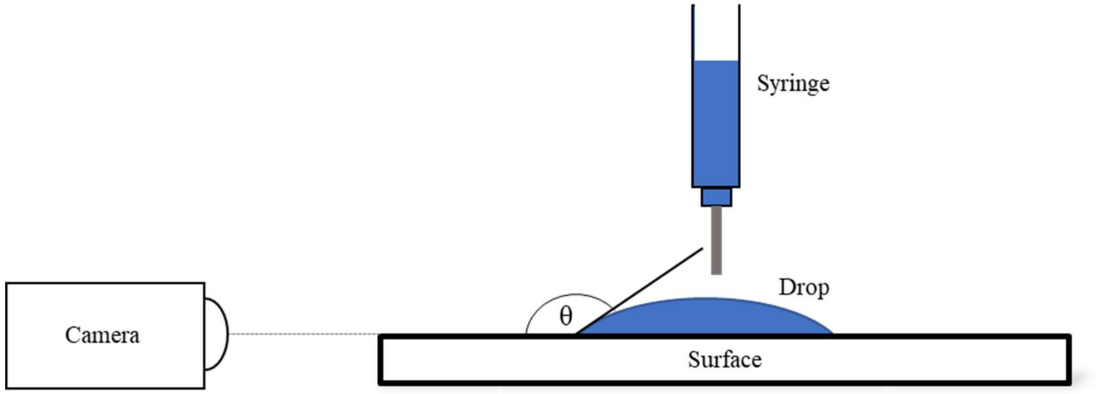

Figure 4. Schematic of contact angle testing apparatus.

The wettability of a liquid on a surface—a measurement of surface energy between a liquid and a surface—can be measured by the contact angle between a drop of liquid and the surface [115]. The contact angle, *CA*, of pGNP suspensions on prepreg surfaces in this work was measured using the sessile drop method, as shown in Figure 4. The prepreg was secured on a level surface and a high-resolution camera was mounted directly perpendicular to the surface to capture the drop in profile. A syringe was used to dispense droplets of 0.05ml. The droplet was expressed to the tip of the needle and then placed on the test surface without letting the drop fall or splash. Images were collected 30-60 seconds after the drop was placed on the surface. Suspensions were measured within 30 minutes after mixing on sheets of uncured prepreg. Images were processed in ImageJ using the DropSnake measurement tool [116].

3.2.5. Temperature Evolution Inside of the Thick Composite

To observe the effects of thermal conductivity and changes to curing kinetics on the curing of large composite members, composite samples were produced by stacking 168 plies with planar dimensions of 5 cm x 5 cm to a total thickness of 2.5 cm. The high thickness of the sample was used to provide a better representation of the cure exotherm. A thermocouple was placed in the center of the sample at the location of the midplane of the layup, shown in Figure 5-a, b. This allows monitoring of the temperature evolution in the middle of the laminate, where the highest temperature peak is expected to occur due to the heat transfer and cure exotherm. These samples were cured under vacuum on a flat mold in a convection oven, without additional pressure and were heated at a rate of 2.8 °C/min to 135 °C for 120 minutes, while internal temperatures were logged.

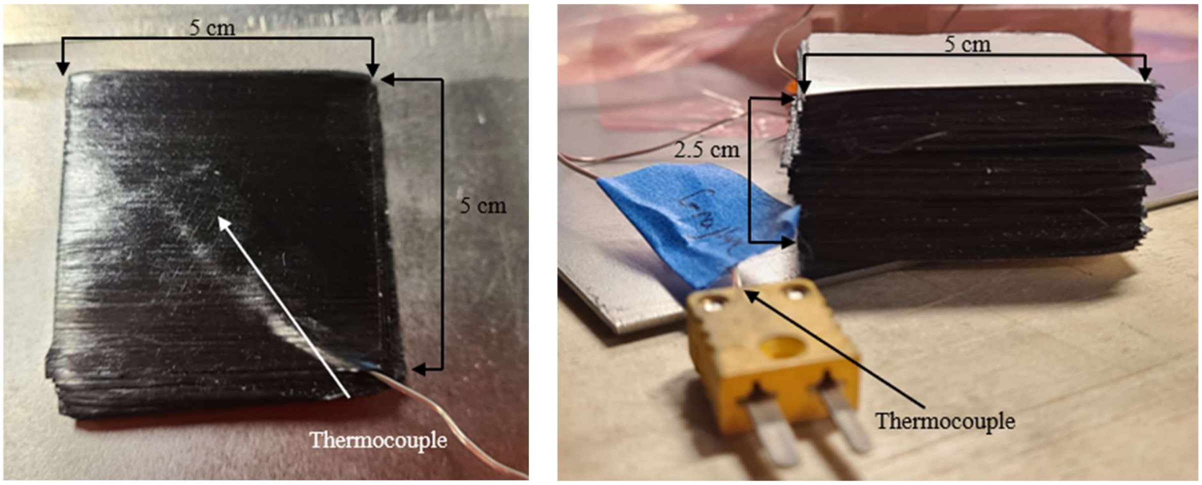

a. *b.*

Figure 5. a) A thermocouple (junction indicated by the white arrow, leads visible in the lower right) placed in the uncured composite, between plies 83 and 84; b) A 168 ply, 2.5 cm thick composite with thermocouple inserted before curing.

3.2.6. Differential Scanning Calorimetry

Differential Scanning Calorimetry (DSC) is a thermal analysis method for obtaining the cure kinetics and degree of cure of a thermoset composite material and was used to measure the impact of interlaminar pGNP on cure kinetics. For this test, two ply composite samples were produced from 13 cm x 13 cm sheets of the prepreg, one pair was left untreated, and another pair of sheets were sprayed with pGNP at approximately 2 g/m² and allowed to dry. Untreated sheets of prepreg were pressed into a two-ply composite. The sprayed faces of pGNP treated plies were pressed together, giving a 4 g/m² interlaminar density. A 2.5 mmx2.5 mm specimen was cut from the center of each laminate and analyzed in a Shimadzu DSC-60A apparatus using aluminum pans under nitrogen atmosphere with dynamic and isothermal heating against reference samples. For dynamic testing, the specimens were heated to 300 ºC with a rate of 10 ºC/min. For isothermal testing, the specimens were heated to 135 ºC and held for 120 minutes. Heat flow through the sample was measured by the instrument under heating and logged and the cure of the composite is shown by a characteristic curve which shows the region where the cure is exothermic.

The degree of cure, α, at time, *t*, is measured by comparing the heat of cure at temperature, ΔH_i, as defined by the integral of the rate of heat generation, *dQ/dt*, from *0* to *t* as given by Equation 1:

$$\Delta H_i = \int_0^t \left(\frac{dQ}{dt}\right) dt \tag{1}$$

To the total heat of cure, ΔH_T to the total heat of reaction as given by the integral of *dQ/dt* from *0* to t_t, the time required to complete the cure; as shown in Equation 2:

$$\Delta H_t = \int_0^{t_t} \left(\frac{dQ}{dt}\right) dt \tag{2}$$

Such that:

$$\alpha = \frac{\Delta H_i}{\Delta H_t} \tag{3}$$

3.2.7. *Dynamic Mechanical Analysis*

Dynamic mechanical analysis (DMA) was used to measure the change in mechanical properties of the pGNP/CFRP composite under continuous heating. DMA is useful in quantifying the glass transition temperature, T_G, of a polymer composite and also quantifies changes to the storage modulus, *E'*, and loss modulus, *E"*, of the composite. Measurements were taken using an Anton Paar MCR 702 MultiDrive with a CTD 600 convective heater, and TPB20 three-point bending fixture. Samples were tested in a three-point bending configuration with a temperature sweep from 20 °C to 250 °C, at a rate of 2 °C/min.

3.2.8. *Flexural Testing*

Composite beam samples were prepared within the guidelines of ASTM D790 using 26 plies of prepreg with a [0°] stacking sequence, with interlaminar pGNP addition between each ply. Composite beams were cut from larger prepared plates. Five beams were tested for each condition.

Flexural modulus and strength were measured on an Ektron TS2000 universal testing apparatus in a three-point bending fixture in accordance with ASTM D790. Beams, approximately 4 mm thick and 13 mm wide, were measured across a 70mm span. The flexural modulus, *E*, is calculated by measuring the slope of the stress over strain in the linear region of deformation, as shown in Equation 4:

$$E = \frac{3P_c}{4bh} \tag{4}$$

where P_c is the critical load b is the beam width, and h is the beam thickness. Flexural strength, σ_f, is calculated using Equation 5:

$$\sigma_f = \frac{3P_c l}{2bh^2} \tag{5}$$

where l is the span length.

3.2.9. *Short Beam Testing*

Composite beam samples were prepared within the guidelines of ASTM D2344 using 26 plies of prepreg with a [0°] stacking sequence, with interlaminar pGNP addition between each ply. Composite beams were cut from larger prepared plates. Five beams were tested for each condition.

Interlaminar shear strength (ILSS) was measured on a Ektron TS2000 universal testing apparatus in a three-point bending fixture following with ASTM D2344. Beams, approximately 4 mm thick and 13 mm wide, were measured across a 35mm span. ILSS, given by F_{31}, is calculated by Equation 6:

$$F_{31} = \frac{3P_c}{4bh} \tag{6}$$

where P_c is the critical load, b is the beam width, and h is the beam thickness.

3.2.10. Mode I Fracture

Large composite panels were prepared within the guidelines of ASTM D5528 for Mode I Fracture by stacking 26 plies of prepreg with a [0°] stacking sequence, resulting in a final panel approximately 4 mm thick. Double cantilever beam (DCB) samples were cut from the cured panels on a bandsaw to the test dimensions at a width of 20-25 mm. The edges of beams were painted with a white correctional fluid to improve crack visibility, and markings were added to track crack growth to the nearest millimeter. Steel hinges were glued to the ends of sample beams using a cyanoacrylate gel adhesive. Cyanoacrylate gel was selected because the cyanoacrylate liquid and available two-part epoxy adhesives both failed under loading at 90°C, while the gel adhesive maintained integrity at the test temperatures. Five DCB samples were tested for each condition.

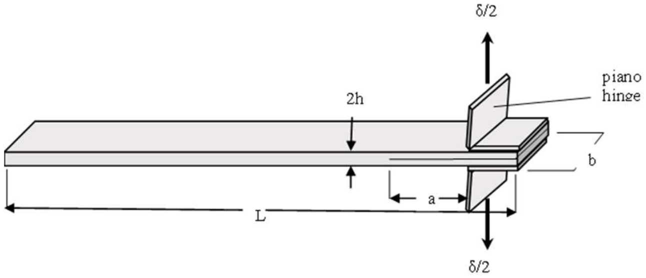

a.

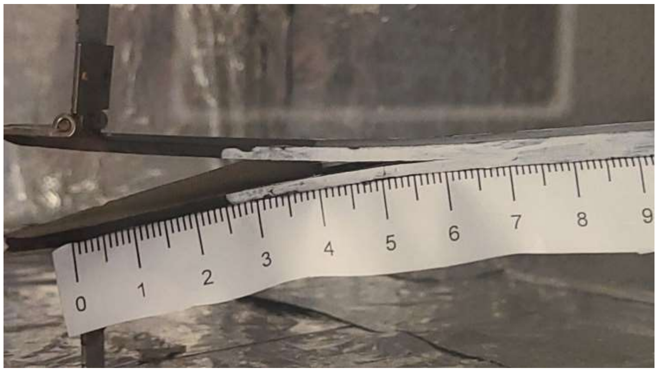

b.

Figure 6. a) Mode I DCB testing configuration; b) Mode I DCB test in operation.

DCB tests for Mode I fracture were performed following the ASTM D5528 standard on an Ektron TS2000 universal testing apparatus as shown in Figure 6. Mode I fracture toughness, G_{IC}, was calculated using the Compliance Calibration (CC) method following ASTM D5528-21. Alternate methods for calculating G_{IC} in ASTM D5528-21 include Modified beam Theory (MBT) and Modified Compliance Calibration (MCC). MBT assumes a beam with no rotation at the reaction front and overestimates G_{IC} and MCC typically provides the highest G_{IC} estimates with the greatest variability, and so CC was chosen as the more consistent and conservative model. The test beam was loaded from the hinges until the crack front propagated 5mm, before unloading and repeating the loading/crack extension for eight cycles. A plot of log (δ_i/P_i) over log(a_i) was generated from test data at each measured crack length and a line of best fit was generated with a slope of n, ranging from 2.56-3.0 for the sampled beams. The compliance factor n was used to calculate the interlaminar fracture toughness as shown in Equation 7:

$$G_I = \frac{nP\delta}{2ba} \tag{7}$$

where P is the load, δ is the load point displacement, b is the sample width, and a is the crack length at fracture.

3.2.11. Mode II Fracture

Mode II fracture was tested according to ASTM D7905 on the fractured Mode I test specimens. Five beams were tested for each condition. Mode II interlaminar fracture toughness, G_{IIC}, was measured on a three-point bending fixture following ASTM D7905 as shown in Figure 7. End notch flexure (ENF) beams were set such that the crack tip was a fixed distance from one of the support rollers (a_0=20mm and a_0=40mm) and loaded at 0.5mm/min to approximately 50% of the estimated critical force (P_c).

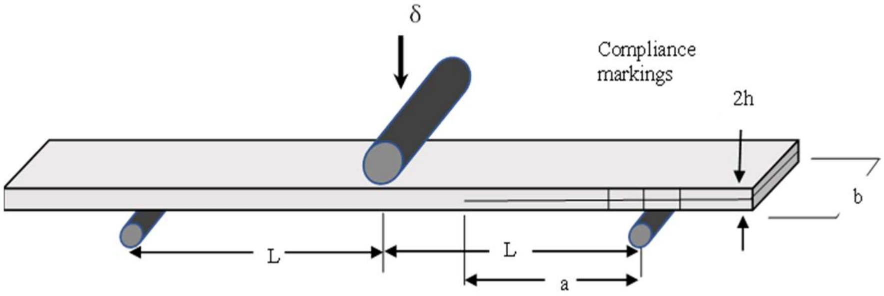

a.

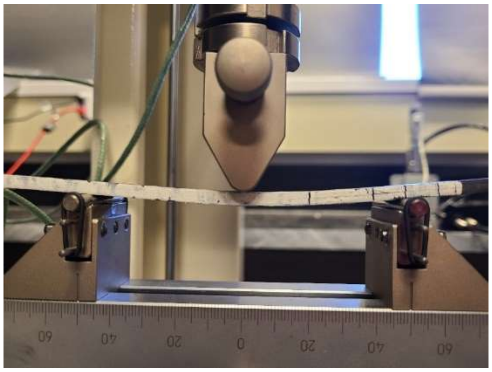

b.

Figure 7: a) Mode II ENF testing configuration; b). Mode II ENF testing in progress.

The ENF test has unstable crack propagation once the load reaches critical value of P_c. A compliance coefficient, m, is calculated according to the Equation 8:

$$\frac{\delta_i}{P_i} = A + ma^3 \tag{8}$$

Mode II interlaminar fracture toughness, G_{IIC}, is given by Equation 9:

$$G_{IIC} = \frac{3mP_c^2 a_0^2}{2b} \tag{9}$$

where *m* is calculated from Equation 8, P_c is the critical load, a_o is the initial crack length (on average 30mm) and *b* is the beam width. The compliance value, *m*, varied depending on pGNP loading and temperature. Untreated beams had *m* values of 0.023-0.040 at 20°C and 0.023-0.053 at 90°C while beams with 2.3 g/m^2 pGNP *m* values of 0.018-0.019 at 20°C and 0.018-0.020 at 90°C.

3.2.12. Fracture Surface Micrography

In order to quantify roughness in the crack surface contributing to crack front elongation, a Leica DM6 optical microscope system was used. Images were taken with a 40x objective lens, and the surface height was measured by using optical profilometry. Surface height data was collected with Leica LAS X Navigator software.

3.2.13. Thermal Conductivity

Thermal conductivity was measured by placing the composite samples in between two Omega HFS-5 heat flux sensors sandwiched between plates of a heat flux apparatus as shown in Figure 8, with the test apparatus inside the convective, heated air chamber.

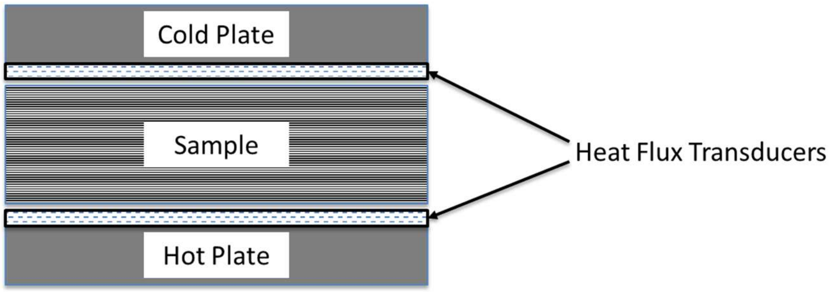

a.

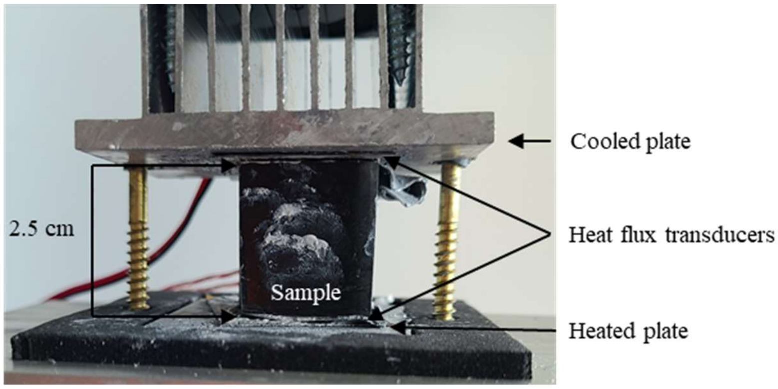

b.

Figure 8: A profile of the thermal conductivity test apparatus.

The heated plate of the apparatus was heated with a thermoelectric heater under a constant 9V DC providing a ~50ºC differential between hot and cold faces. The cooled face was actively cooled with air in the heated chamber at 30ºC, 50ºC, 70ºC, and 90ºC. Heat flux sensors were wired to an Omega HFS-DAQ data logger and values were recorded to a log file. Thermally conductive paste, Omega OT-201-2, was used between all contact faces. The measured heat flux was averaged between the two sensors and used to calculate TC. Measurements in each sample were taken longitudinally, along the fiber length (k_{11}) and through the thickness of the composite (k_{33}). TC for the sample was calculated according to the heat flux equation, Equation 10:

$$k = \frac{xQ}{\Delta T} \tag{10}$$

where k is the TC of the sample in Watts per meter-Kelvin (W/(m·°K)), ΔT is the temperature differential across the sample in Kelvin (°K), *x* is the thickness in meters (m), and *Q* is the average heat flux across the sample in Watts per square meter (W/m^2).

3.2.14. Electrical Conductivity

Electrical measurements were performed on the same samples as were used in thermal conductivity tests. Electrical resistance was measured using a Kelvin four-point measuring technique. This method uses separate pairs of current-carrying and voltage-sensing electrodes, which is advantageous for the measurement of low resistance values because separation of current and voltage electrodes eliminates the lead and contact resistance from the measurement. Composite samples were polished and clamped between copper plates in a fixture inside the heated chamber with a conductive paste at the interface, as shown in Figure 9. Current was supplied with a TEKPower™ TP3005P Programable DC power supply and voltages was measured using a Commercial Electric™ MAS830B digital multimeter across the sample. Measurements were taken at 30ºC, 50ºC, 70ºC, and 90ºC, longitudinally, along the fiber length (k_{11}) and through the thickness of the composite (k_{33}). At each temperature, values were allowed to stabilize, indicating thermal homogeneity throughout the sample.

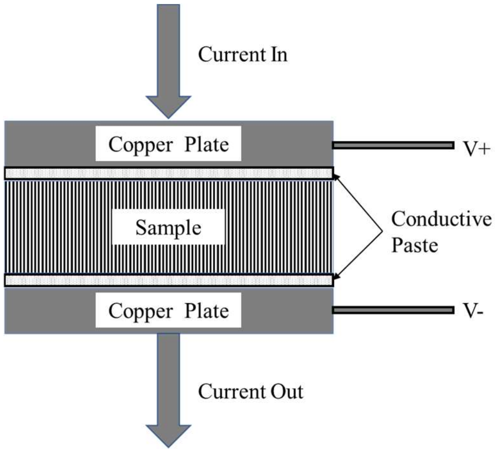

Figure 9. A profile of the four-point electrical conductivity test apparatus.

Current, *I*, is supplied at a constant value. Voltage, *V*, is measured across the sample. Resistance, *R*, across the sample is calculated according to Ohms Law, Equation 11:

$$R = V/\mathrm{I} \tag{11}$$

Conductivity, κ, is converted to conductivity in Equation 12:

$$\kappa = \frac{l}{RA} \tag{12}$$

where κ is the conductivity in siemens per meter (S/m), l is the width of the sample, and A is the cross-sectional area of the sample in meters, m^2.

CHAPTER 4

PLANT BASED GRAPHENE PROPERTIES

This chapter discusses the measured properties of the pGNP used in this study. GNP properties are key to understanding the interactions which are responsible for a wide range of results achieved in utilizing GNP, in this and other works. Factors—such as surface functionalization—which are responsible to a large degree in effects like interfacial bonding with the matrix, are often overlooked [1,23,25–27,47–49]. Nanoplatelets from alternate sources to mineral graphene warrant additional description to validate that they are graphitic and how they diverge from conventional GNP. Recent studies referencing plant based graphenes have omitted this information and appear to be using milled hard carbons rather than graphitic carbons [117].

The large relative environmental impact of nanomaterial production warrants validation of the cradle-to-gate life cycle assessment of pGNP. A cradle-to-gate assessment measures the carbon impact of a material from its production to its delivery to a user, as opposed to cradle-to-gate assessment which includes product lifecycle and the impacts of disposal. A cradle-to-gate assessment is warranted in this case because the impact of GNP use is overwhelmingly in production and because the usage and disposal are largely unknown.

Raman spectroscopy was used to quantify graphitization of the GNP. Particle morphology was assessed by electron microscopy, with lateral dimensions measured by SEM and thickness and layer count assessed by TEM. The two methods were used because of the high asymmetry of GNP. Surface functionalization was assessed using XPS. Results for these tests are compared to provide a cohesive description of the pGNP.

4.1. pGNP Production and Life Cycle Assessment

Plant based graphene nanoplatelets (pGNP) are produced by a proprietary and confidential thermochemical process which converts the sp3 bonded hard carbons typical of charcoals [62] into sp2 bonded graphitic carbons. The materials in this study were produced from renewable pine wood sources, similar particles have been produced from corn stover, lignosulfonates, and spent tea leaves. Because the feedstock used is photosynthesized biomass, carbon dioxide released from thermal decomposition of the biomass does not represent a net increase to atmospheric CO_2 levels. The pGNP produced from biomass sources is solid carbon, removed from the atmosphere through photosynthesis and graphitization [118]. As a result, one kg of pGNP at 93.3% carbon by mass is equivalent to 3.43 kg CO_2 equivalent sequestered from the atmosphere. pGNP production involves several other points of CO_2 generation. The production process for pGNP production requires 1,002 MJ/kg of energy, the majority of which is used for process heating at various stages. This is more energy than is required for chemical exfoliation of graphite, but less than thermal exfoliation. This can be provided through natural gas combustion, electricity, or recovered gases from the thermal decomposition of biomass. Natural gas combustion for the required energy would result in emissions of 66 kg of CO_2 equivalent per kg pGNP.

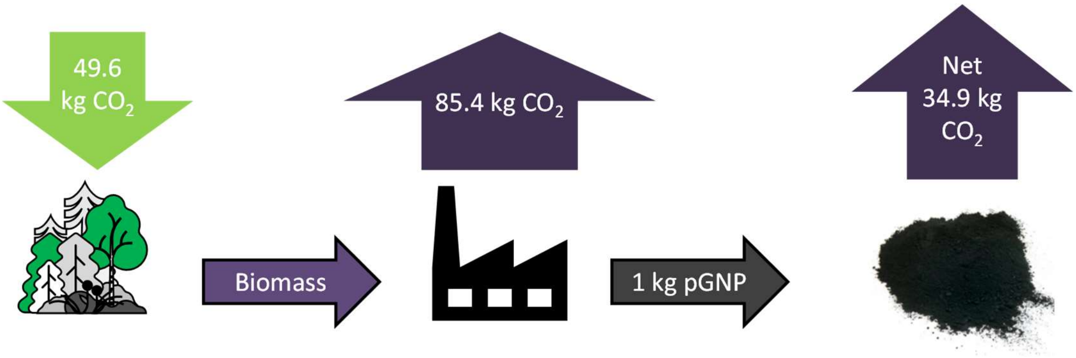

Figure 10: Schematic representation of CO_2 flows during pGNP production.

The feedstock wood has an energy density of 19,080 kJ/kg [119], which provides 457 MJ/kg-pGNP produced. When captured and utilized, this reduces energy requirements to 545 MJ/kg-pGNP and fossil carbon emissions to 34.9 kg CO_2/kg-pGNP, as shown in Figure 10. Utilization of renewable energy, either from renewable electric generation or from onsite biomass combustion would result in no net CO_2 emissions [118], giving a range of 0-34.9 kg CO_2/kg-pGNP.

Table 1. Energy usage for various means of graphene production

Graphene production method	Energy Usage (MJ/kg)	Health and Environmental Risk
Chemical Reduction of Graphene-oxide	*900-1000 [15]*	*Medium-High [14]*
Ultrasonic Exfoliation of Graphene	*70-500 [15]*	*High [15]*
Thermal Exfoliation	*2000 [12]*	*Low [12]*
Thermal pGNP Conversion	*0-545 [120]*	*Low [120]*

As shown in Table 1, the energy usage for pGNP production using a combination of natural gas and recovered energy from the thermal decomposition of biomass is substantially lower than thermal exfoliation and chemical reduction as routs for producing GNPs. The energy usage is comparable to that of ultrasonic exfoliation of graphene. Further, the pGNP production process does not use hydrazine or concentrated acids and does not produce hazardous byproducts.

4.2. pGNP Characterization

4.2.1. Raman Spectra

Graphene is identified in Raman spectroscopy by three characteristic peaks, referred to as the D, G, and 2D peak. The ratios between these peaks indicate the properties of the graphene measured. Using a 532 nm laser, the D peak is at 1350 cm^{-1}, the G peak is at 1580 cm^{-1}, and the 2D peak is at 2700 cm^{-1}. The 2D peak in particular and the ratio of 2D/G identifies the extent of sp2 bonding in graphene which is absent in amorphous carbons. Raman spectroscopy of pGNP, as shown in Figure 11, gives an average 2D/G ratio of 0.28 with a maximum of 0.68, showing a few-layer graphene of 3 or more layers [121,122]. A Raman spectra of an amorphous wood carbon—produced from the same feedstock as pGNP and carbonized though heating under an inert atmosphere—is given as a contrast. The 2D peak is entirely absent in the wood carbon sample, showing typical sp3 bond structure with no sp3 aromatic structure.

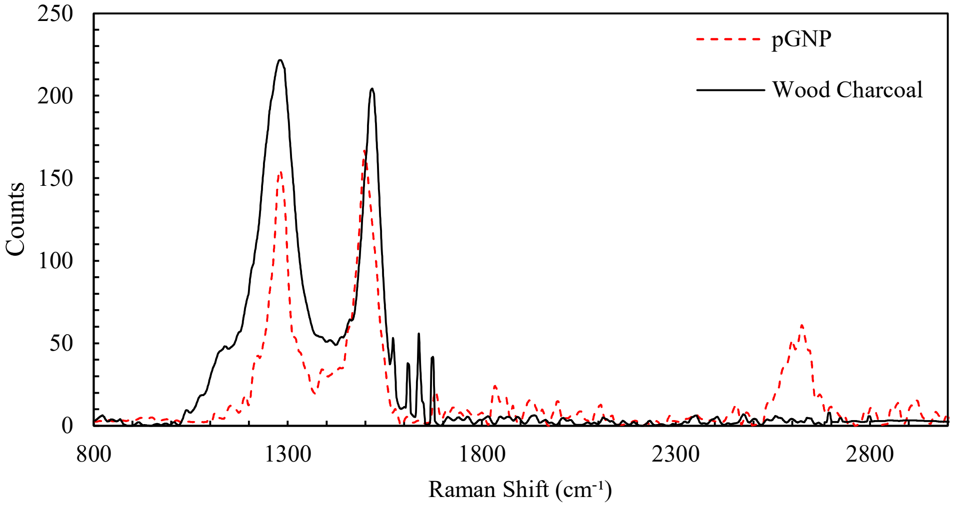

Figure 11: Raman spectra pGNP and a pyrolytic wood charcoal.

The D/G ratio measures the degree of disorder of the flakes, along with surface functionality and the edge properties of graphene. An average D/G ratio of 0.80 for pGNP ratio shows a highly disordered sample [121], which is to be expected from a non-graphite derived material and which corresponds with XPS data later in this chapter showing surface functionality. A D/G of >1.0, as shown in the wood charcoal sample, is indicative of an amorphous, hard carbon with sp3 bonding.

4.2.2. SEM

SEM imaging, as shown in Figure 12 was used to give a profile of the lateral dimensions of pGNP particles. 421 particles measured gave a range of lateral dimensions from 70-1200 nm with a median lateral size of 240 ± 100nm.

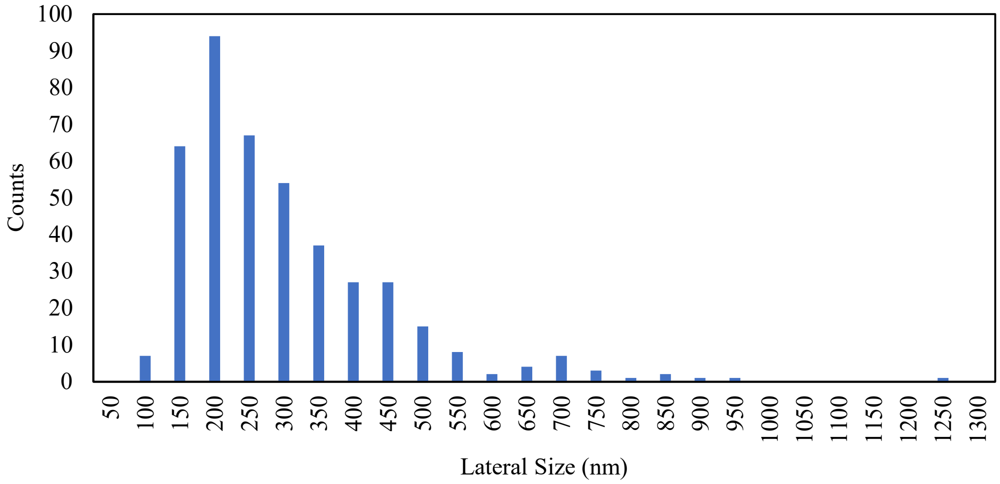

Figure 12: Lateral size survey of pGNP platelets from SEM scan.

The morphology of pGNP is shown in TEM scanning images, as compared to mineral graphene platelets in Figure 13.

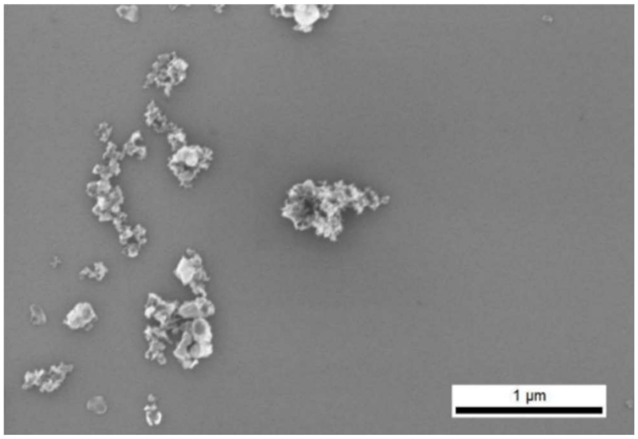

a.

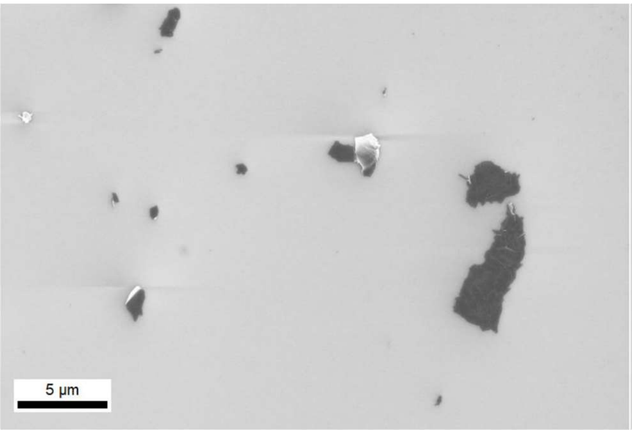

b.

Figure 13: a) SEM scan of pGNP plateletss; b) SEM scan of mineral derived graphene platelets.

Mineral GNP shows larger lateral dimensions and a morphology typical of exfoliated graphite. pGNP by contrast is composed of stacked clusters of graphene platelets more typical of graphenes developed by CVD.

4.2.3. TEM

TEM imaging, as shown in Figure 14 shows stacked, multilayer graphene crystals with an interlaminar spacing of 0.345 nm. The interlaminar spacing is slightly larger than the 0.335 nm spacing typical of mineral graphene. The multi-crystal morphology is more similar to graphene crystals prepared by chemical vapor deposition than exfoliated mineral graphene.

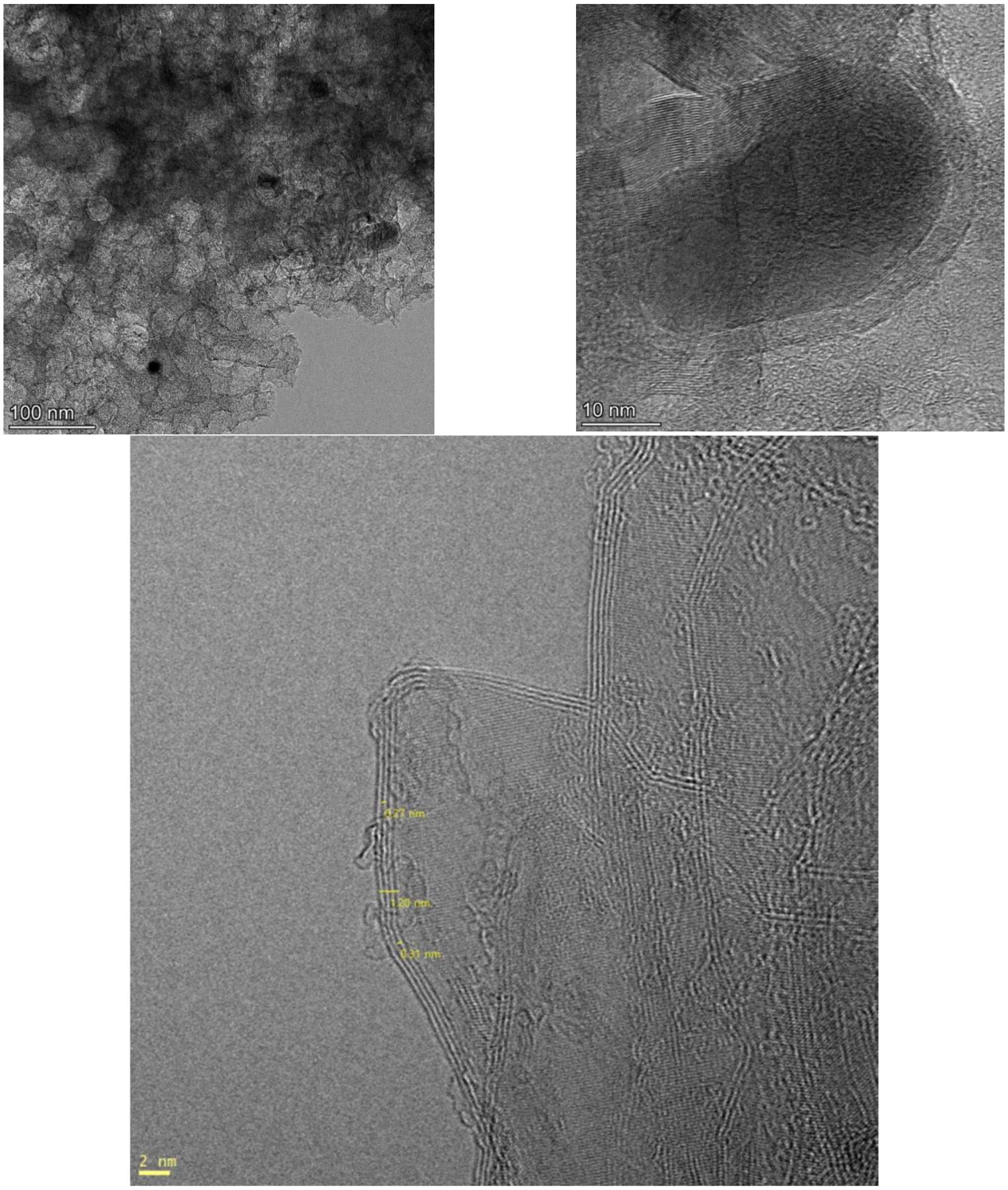

Figure 14: TEM scan pGNP nanoclusters, showing overlapping platelets at layer counts of 4-10. Interlaminar spacing is 0.345 nm.

TEM provides more resolution on the pGNP morphology shown in SEM. Here, the structure of overlapping, stacked nanoplatelets is clearly visible. A survey of the layer counts in the nanoplatelets shows a range of layers from 3-10.

4.2.4. XPS

X-ray photoelectron spectroscopy, as shown in Figure 15, indicates 87.0% carbon, 10.3% oxygen, 1.4%

nitrogen, and 1.3% other elements from wood ash. The structure of the carbon bonds on the powder surface showed 49.82 % sp2 graphitic/graphene bonding, 36.34% graphene-oxide/epoxide groups (C-O-C) and 13.83% carboxyl groups (O-C=O). Surface C:O ratio is 8.45:1, overall C:O ratio is >15:1, indicating that the majority of oxygen is located in surface functional groups.

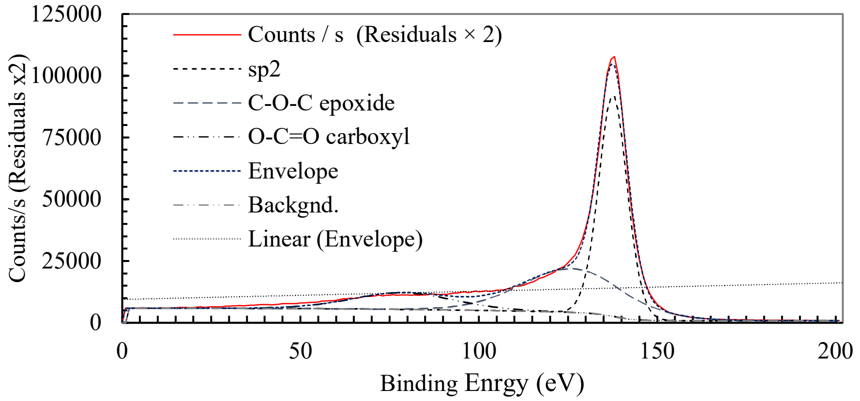

Figure 15: XPS analysis of surface scans show 49.82% sp2 (graphitic carbon), 36.34% C-O-C (graphene oxide/epoxide), and 13.83% O-C=O (carboxyl group).

4.3.Discussion

Analysis from TEM, Raman spectroscopy, and XPS gives a consistent description of pGNP nanoplatelets. The high D:G ratio shown in the Raman spectra could be interpreted to indicate a significant degree of amorphous impurities, which would indicate incomplete graphitization. However, XPS shows a combination of sp2 graphitic/graphene bonding, epoxide groups, and carboxyl groups. The surface C:O ratio is much higher than the bulk C:O. This indicates virtually total graphitization of the biomass carbon without measurable amorphous impurities. TEM shows stacked, multilayer graphene crystals with a morphology more similar to graphene crystals prepared by chemical vapor deposition than exfoliated mineral graphene. The interlaminar spacing of 0.345 nm is slightly larger than the 0.335 nm spacing typical of mineral graphene, but this is consistent with the degree of surface functionalization observed with XPS. When interpreted with XPS and TEM results, the high D:G ratio can be attributed to a combination of the disordered, turbostratic structure of the particles along with the surface functionalization. It is important to observe that guides for characterization of graphenes using a single method, such as Raman, make assumptions based on characterizations of mineral graphenes and would not account for the turbostratic structure or surface functionality of the plant-derived material [121–123].

Biomass feedstocks typically carbonize into amorphous, hard carbons [62] which are typically of a micron scale or greater and which do not have the high aspect ratio or aromatic bonding which gives graphene its properties. pGNP has all of the same properties which make mineral and CDV graphenes desirable, as well as having a morphology and functionality which are useful to applications in thermoset polymers. The biomass derived pGNP contains a higher number of SFGs as compared to mineral graphite which increase interaction with simple solvents such as water, alcohol, and acetone—as will be shown in the next chapter—resulting in a GNP which can be more easily utilized in simple applications such as spray coating. Further—as will be shown in Chapter 6—epoxide functional groups offer opportunities for crosslinking in a thermoplastic matrix.

Graphene production from mined graphite requires high purity, lump graphite with limited sources. In addition, there are several environmental concerns with mineral graphene production due to hazardous materials in wastewater [94]. The use of a biomass feedstock provides a renewable feedstock with opportunities for dramatic reductions in carbon emissions. Graphene use has been shown to have potential to reduce lifecycle carbon emissions in application where small amounts of GNP replace large volumes of conventional fillers, but the high energy cost of mineral GNP production can lead to situations where GNP addition increases the carbon impact of parts, especially where the GNP is not replacing another filler. The low energy cost of pGNP production and the lack of hazardous chemicals in the process creates a significant opportunity for capturing the benefits of nanomaterial addition without the environmental costs.

CHAPTER 5

SPRAY FORMULATION

This chapter discusses the measured properties of the pGNP spray formulations produced and the selection of the formulation used in this study. A wide range of solvents are available for the base of the suspension, with several properties that must be considered including cost, polarity, interactions with the prepreg, health and safety. Water is the default choice since it is the lowest cost and most broadly available when compared to other solvents. Alcohol is widely used for the spray application of GNP [7,97,98], as well as acetone to a lesser extent [29], owing to their wide availability, relative inertness, and low cost. Acetone is soluble with epoxy resins, and can degrade the resin quality, and so was omitted from evaluation with prepreg substrate. Exotic solvents such as n-methyl-2-pyrrolidone (NMP) and dimethyl sulfoxide (DMSO) are frequently used due to their ability to hold higher loadings of GNP in suspension [1] but have significant drawbacks. DMSO and NMP are significantly more expensive as compared to water and alcohol. DMSO has a low volatility and can interact with a wide range of chemicals, including epoxy resins and crosslinkers [124,125]. NMP is highly volatile but has significant environmental health and safety risks that limit its use in many applications [126]. Other additives, shown in Figure 16, can be beneficial in formulating a suspension. Carboxymethyl cellulose (CMC) is a widely used as viscosity modifier used to stabilize emulsions, and as a binder. Sodium dodecyl sulfate (SDS) is an anionic surfactant which is the sodium salt of a 12-carbon tail group combined with a polar organosulfate headgroup. The alkyl chain lays along the pGNP surface while the polar head interacts with the solvent, improving dispersion in polar solvents [127]. CMC and SDS are both plant derived and have been shown to provide benefits to pGNP dispersion [128–130].

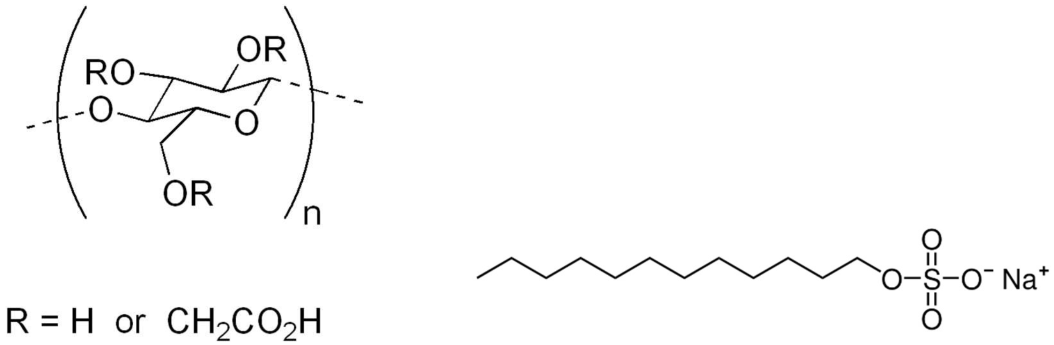

a. *b.*

Figure 16: Diagrams of; a) Carboxymethyl cellulose (CMC) and b) Sodium dodecyl sulfate (SDS).

To examine the dispersion characteristics and determine a functional spray composition, several mixtures were formulated. The supplied 70 g/l pGNP dispersion was diluted with an equal volume of either DI water or 91% IPA. pGNP/91% IPA dispersions were produced by direct exfoliation of pGNP into the solvents using a high shear mixer for thirty minutes. As a reference, suspensions were also produced with GNP supplied by Kanodia Minerals & Chemical Co, India. GNP from mineral and synthetic graphite sources were supplied. In sets of 50 ml tubes, each pGNP solvent mix was blended with 0.047g CMC, 0.220g of SDS, both 0.047g CMC and 0.220g of SDS, or neither. All samples were blended on a high shear mixer for ten minutes to thoroughly mix all components. mineral graphene was used as a baseline material to compare dispersion.

5.1. Dispersion

A dispersion, in the context of this dissertation, refers to solid particles suspended in a continuous liquid phase. Because the particles are between 1 nm and 1 μm, the dispersion may be considered a colloidal suspension [131]. Dispersion is important for GNP application for two reasons. First, Spray application requires that a significant mass of GNP be suspended in the solvent and that the suspension be stable for a long enough time that the suspension be usable. Second, in order to apply GNP evenly through a composite it is critical that the nanomaterial not be agglomerated, otherwise exceptionally high energy methods are required to redisperse the GNP. The stability of a dispersion requires that the energy barrier to aggregation be large enough that Brownian motion of the particles in suspension be sufficient to maintain it. Because the energy of a colloidal system is determined by the interfacial area and tension and because the theoretical surface area of monolayer graphene is ~2590 m²/g, graphene is exceptionally difficult to disperse in polar solvents [1]. SFGs provide a pathway to increasing the energy barriers to agglomeration, as do dispersion aides [1]. To quantify the dispersibility of pGNP and means to engineer stable suspensions, pGNP was compared to Mineral Graphene (MG) and Synthetic Graphene (SG), examined in water and alcohol solvents, and tested with plant-based dispersion aides. The mass of dispersed solids was measured after 48 hours of settling time by drying a volume of the suspension and measuring the remaining solid matter.

5.1.1. pGNP vs. Graphene

pGNP was compared to mineral graphene (MG) and Synthetic Graphene (SG) in dispersions of DI water and IPA, as shown in Table 2. MG was only measured in trace amounts in water and IPA after 48 hours, while SG was dispersed at 0.24 g/l in water and only trace amounts in IPA. pGNP was substantially more dispersible in both at 0.4 g/l in water and 0.13 g/l in IPA. This is attributed to the polar epoxide and carboxyl functional groups on the pGNP surface and corresponds with increased dispersibility from GNP with similar functionality [1].

Table 2. Dispersibility, of pGNP, MG, and SG in water and 91% IPA.

	DI Water (g/l)	*91% IPA (g/l)*
pGNP	*0.4*	*0.13*
MG	*0.01*	*0.01*
SG	*0.24*	*0.01*

5.1.2. Solvents and Additives

pGNP was dispersed in suspensions of DI water, 91% IPA, and 45% IPA (a 50% blend of DI water and 91%IPA). CMC and SDS were tested for their impacts to dispersion at 2 g/l and 5 g/l, respectively. Sample suspensions after 48 hours of settling are shown in Figure 17, with the results of the settling test given in Table 3.

Table 3. Dispersibility of pGNP in water and 45% IPA with CMC and SDS additives.

	DI Water (g/l)	*91% IPA (g/l)*	*45% IPA (g/l)*
pGNP	*0.4*	*0.13*	*0.4*
+CMC	*3.31*	*0.09*	*5.05*
+SDS	*2.50*	*0.53*	*5.61*
+CMC+SDS	*5.60*	*0.48*	*4.68*

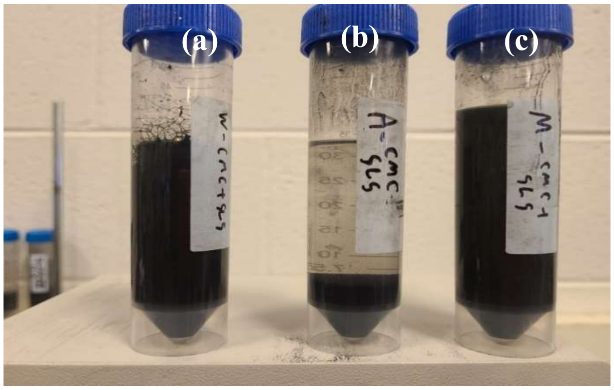

Figure 17: pGNP+CMC+SDS dispersions after 48 hours resting. A) in DI water; b) in 91% IPA, and; c) In 45% IPA. The opaque black color in the left and right samples indicates a much higher pGNP dispersion.

Higher loadings of CMC had a negative impact on suspension viscosity, and higher loadings of SDS caused foaming during mixing. The same suspensions were measured for surface energy and viscosity. Addition of dispersion modifiers increases pGNP dispersibility by an order of magnitude, as shown in Table 3. The highest dispersion of 5.61 g/l is given by 45% IPA with SLS, followed closely by DI water with CMC and SDS at 5.60 g/l. pGNP/IPA exhibited very poor dispersion of pGNP and were deemed unsuitable for further exploration.

5.2.Surface Energy

The contact angle, CA, was measured shortly after mixing on a sheet of uncured prepreg using the sessile drop method, as shown in Figure 18. High contact angles represent the highest surface energy and best wetting of the surface which is important to distributing pGNP uniformly. As shown in Table 4, the pGNP/IPA dispersion exhibited the best surface wetting, with a 180º contact angle. pGNP/Water produced the lowest contact angle at 123.4º. pGNP with CMC and SDS in 45% IPA provided intermediate surface wetting with a contact angle of 152.9º.

Table I4. Contact angles (CA) of pGNP in water, 91% IPA, and 45% IPA with CMC and SDS additives.

	DI Water	*91% IPA*	*45% IPA*
pGNP	*117.3°*	*180.0°*	*144.8°*
+CMC	*119.0°*	*156.1°*	*156.2°*
+SDS	*116.4°*	*158.4°*	*152.9°*
+CMC+SDS	*123.8°*	*162.3°*	*152.9°*

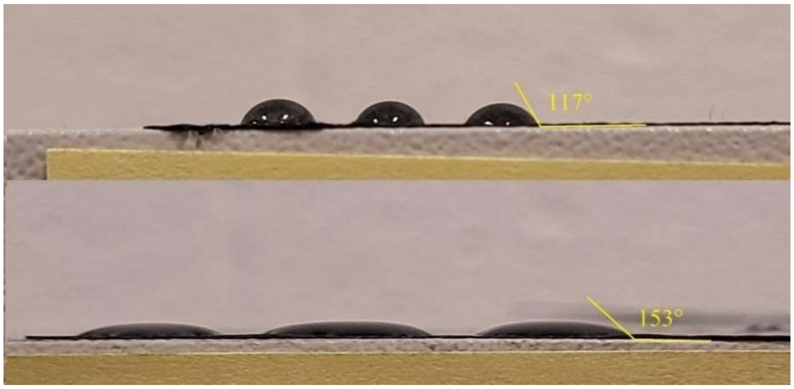

Figure 18: Contact angle measurements for pGNP in DI water at 117º and pGNP in 45% IPA with CMC and SDS at 153º.

The impact of CMC and SDS is dependent on the solvent. In 91% alcohol, both additives reduced wetting through increases in viscosity and surface tension. In DI water and 45% IPA, CMC and SDS increased surface wetting over the base solvent.

5.3. Viscosity

The viscosity measurements of DI Water and 45% IPA pGNP suspensions are detailed in Table 5, below. Other solvents were determined not to have sufficient dispersibility of pGNP to be viable as spray suspensions. The 45% IPA, pGNP mixture shows a higher viscosity than water. CMC addition increases the mixture slightly in all cases, while SDS addition increases viscosity dramatically in water but trivially in IPA solutions.

Table 5. Viscosity of pGNP suspensions in water and 45% IPA with CMC and SDS additives.

	DI Water, η *[mPa·s]*	*45% IPA,* η *[mPa·s]*
pGNP	*2.089*±0.991	*4.223*±0.943
+*CMC*	*2.206*±0.0.166	*5.263*±0.983
+*SDS*	*17.093*±34.250	*4.148*±1.135
+*CMC*+*SDS*	*1.918*±0.204	*6.155*±3.278

The viscosity profiles for the 45% IPA suspensions are shown in Figure 19. All suspensions show shear thinning with increasing shear rates, with the CMC containing suspensions showing this to a much greater extent. In the 45% IPA, the CMC and CMC+SDS suspensions increase viscosity at 1 s^{-1} to 516 and 267 mPa·s, respectively from 17 mPa·s in the suspension with no additives. These viscosity profiles are well suited to a spray mixture. Low viscosity at high shear rates improves spray performance of the suspension because it requires less energy and produces a finer spray, where a high viscosity at low shear rates prevents dripping and sagging during drying and reduces the settling of particles over time [63,64]. The addition of CMC to the suspension provided the greatest improvement to low shear viscosity, without negatively impacting viscosity at high shear rates. The lack of viscosity improvements with SDS in alcohol are not surprising, since SDS is a salt and IPA is much less polar than water [132]. As a surfactant, SDS reduced the surface tension of the liquid in the suspension, and the tension at the graphene/liquid interface which improved nanoparticle wetting and particle suspension [133].

The increase in low shear rate viscosity with CMC addition is expected and provides the combined benefits of improving spray performance (as discussed earlier), nanoparticle suspension, and improvements in surface wetting. The high viscosity at low shear rates helps to keep nanoparticles from settling which is a key element in dispersing particles. The CMC addition was most effective in the 45% water/IPA mixture as well, with an increase in suspended solids from 0.40 g/l to 5.05 g/l. CMC addition increased viscosity at 1 s^{-1} shear rate from 17.1 mPa·s to 516.4 mPa·s. The combined particle dispersion with CMC and SLS was reduced slightly in the water/alcohol mixture from CMC or SDS alone, but the overall combination of properties of the suspension was optimized using CMC and SDS in the 45% water/IPA mixture.

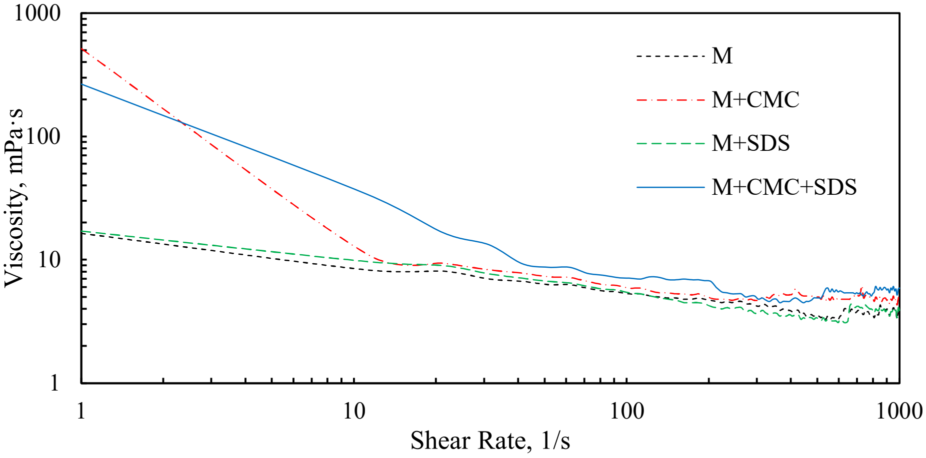

Figure 19: The viscosity of 45% IPA suspensions measured at shear rates of 1-1000 s^{-1} show moderate shear thinning for the neat and SDS mixture, but more dramatic shear thinning for the CMC and CMC+SDS suspensions.

5.4.Test Spraying

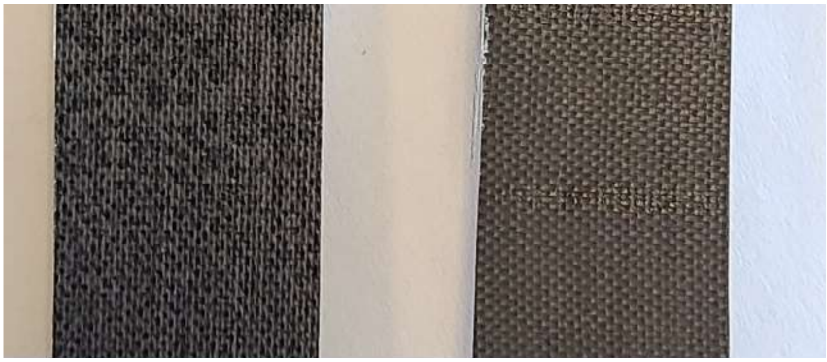

Figure 20: DI water-based suspension (left) leaves an inconsistent, spotty coating. 45% IPA-based suspension (right) leaves a uniform coating.

DI Water and 45% IPA pGNP suspensions were sprayed onto CF-prepreg panels to observe the spraying and drying behavior, the results are shown in Figure 20. The low surface energy and poor wetting behavior of the water-borne pGNP suspension leads to beading of the spray on the prepreg surface. The beading effect, coupled with a low drying time, leads to an inconsistent pGNP coating, with visible regions of high particle density interspersed with regions of low density.

5.5.Discussion

The pGNP spray solution was prepared by combining 220 ml of 70 g/l graphene/water slurry with 1.8513 g of SDS, 0.3846 g of CMC, and 217 ml of 91% IPA and mixing until the SDS and CMC were thoroughly dissolved. This suspension provided the best balance of dispersion at 4.68 g/l, a contact angle of 152.9º, 1 s^{-1} viscosity of 267 mPa·s and 1000 s^{-1} viscosity of 5.9 mPa·s.

The selected suspension did not have the highest suspension, surface wetting, or best viscosity but it gave the best blend of these properties. Water offers higher dispersion of pGNP than alcohol and can be a preferred choice over other solvents because of its ease of use and availability has a much lower surface energy on the epoxy matrix as compared to IPA. IPA provides excellent surface wetting on the prepreg surface, as well as being highly volatile to promote fast, even drying but it has poorer dispersion characteristics for the pGNP. A mixture of 45% IPA and 55% water offers an effective balance of dispersibility and surface wetting. Other solvents could provide better properties but at a higher cost and with prohibitive environmental hazards [1]. pGNP was shown to be more dispersible than MG and SG in the solvents tested due to the polar epoxy and carboxyl functional groups.

Use of plant-based dispersion aids further improved suspension performance. CMC was used as a dispersion aide while improving viscosity and surface tension. CMC addition increases the suspension viscosity at low shear rates by 30x without substantially increasing high shear viscosity. High viscosity at low shear rates prevents dripping and sagging during drying and reduces the settling of particles over time which was observed by the increased to pGNP suspension with CMC addition. Low viscosity at high shear rates requires less energy to spray and produces a finer atomization [63,64], the increase in high shear viscosity with CMC addition is not significant, but at higher loadings it would become detrimental. SDS was added as a dispersion aide and anionic surfactant. SDS reduces the surface tension between pGNP and the polar solvent, which improves interface between the particles and the liquid. This effect is most striking in the 45% water/IPA mixture where suspended solids are increased from 0.40 g/l for water/IPA alone to 5.61 g/l with SDS addition.

Spray testing showed that the engineered suspension provided a means for even, low level pGNP interlaminar application as compared to a simple water spray which created a spotty, uneven coating. The suspension discussed in this chapter was engineered for use with an epoxy composite system. Other composite systems would require similar engineering to match pGNP properties with solvents and dispersion aides which will work together constructively for the target material system.

CHAPTER 6

CURING KENETICS

This chapter discusses the results of investigation on the curing kinetics of pGNP/CFRP. Work in Chapter 4 shows pGNP to be distinct from exfoliated mineral GNP in functionality due to the presence of carboxyl and epoxy functional groups which can interact with the thermoset system during curing. Additionally, work studying the thermal conductivity of GNP has shown both increases due to the high thermal conductivity of GNP [48,102] and decreases due to particle agglomeration and poor particle/matrix interaction [8]. A substantial increase or decrease in the temperature of cured composite parts presents an important design consideration for pGNP/CFRP, as does a substantial change in the curing time. Because multiple interactions can potentially affect the curing kinetics, multiple methods are used for characterization. DSC was used to measure the heat flux in pGNP composites as compared to neat composites as an indication of the rates of curing reactions. Raman Spectroscopy was used to measure the cured bond structure to quantify the impact of pGNP addition on the bond structure of the cured composite. Finally, because temperature evolution in the center of thick parts is a product of through thickness conductivity and heat of reaction, tests were performed measuring the temperature in the center of thick composite sections.

6.1.Differential Scanning Calorimetry

DSC exotherms of the treated and untreated composites in dynamic heating are shown Figure 21-a. The peak heat flow is slightly lower in the pGNP sprayed composite, 1.70 mW/mg vs. 1.84 mW/mg, but the time of reaction is extended for the pGNP sprayed composite. The total heat to cure is almost identical in both cases: 114 J/g for the pGNP/CRFP vs. 112 J/g for the neat CRFP. The exotherm for pGNP treated composite has a distinctive shoulder at higher temperatures, indicating changes to the cure kinetics due to the presence of pGNP. The degree of cure for the treated and untreated composites are shown in Figure 21-b. The degree of cure in pGNP/CFRP initiates at lower temperature, 110ºC vs 126ºC in neat CFRP, and completes at a higher temperature, 259 ºC vs 218 ºC in neat CRFP.

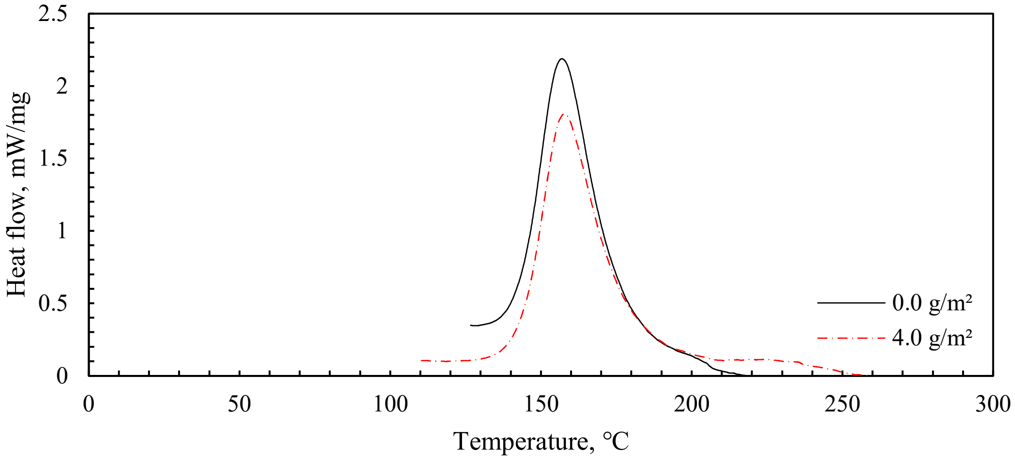

a.

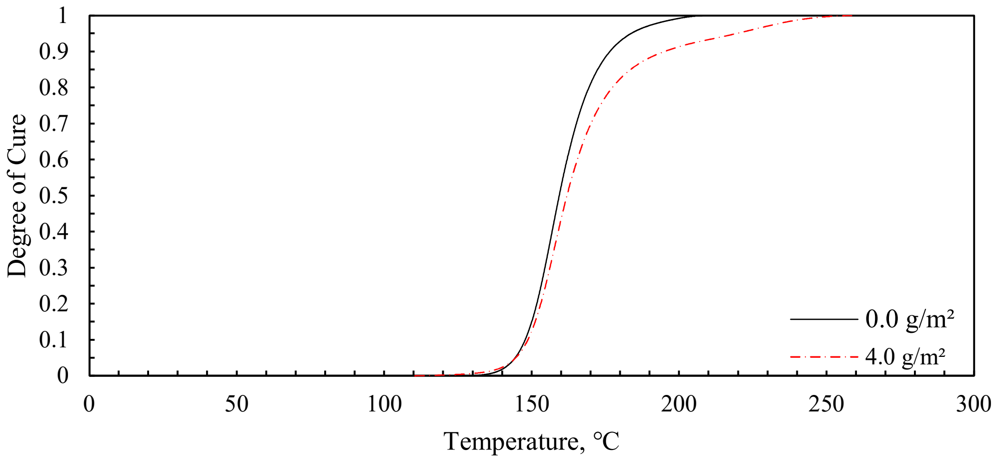

b.

Figure 21: a) Exotherm profiles of curing pGNP/CRFP and neat CRFP under dynamic heating; b) The degree of cure with heating of pGNP/CRFP as compared to neat CRFP.

Isothermal DSC exotherms are shown in Figure 22-a and degree of cure is shown in Figure 22-b. As with dynamic heating, the peak heat flow is lower in the pGNP treated composite, 0.60 mW/mg vs. 0.71 mW/mg for neat CRFP. The time of reaction is extended for the pGNP sprayed composite, 78 minutes vs 64 for neat CRFP. Similar to the dynamic test, the total heat to cure is unaffected by pGNP: it is 117 J/g for the pGNP/CRFP vs. 120 J/g for the neat CRFP.

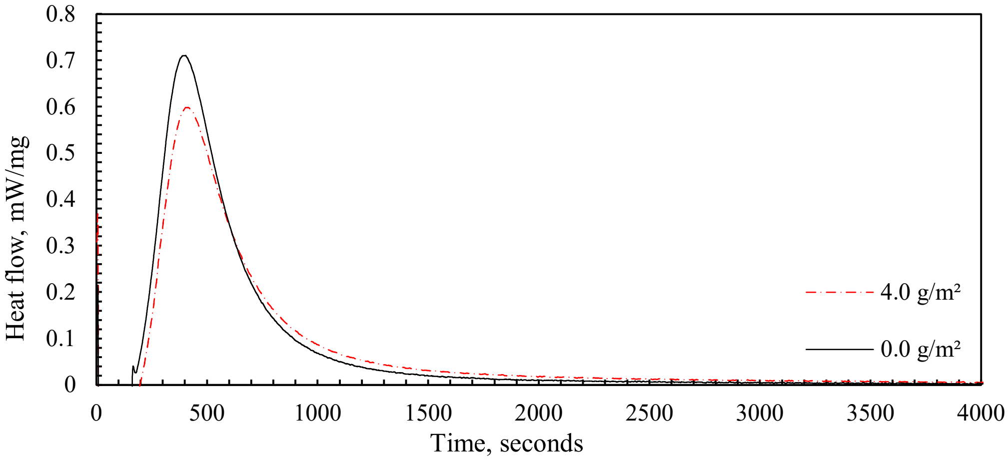

a.

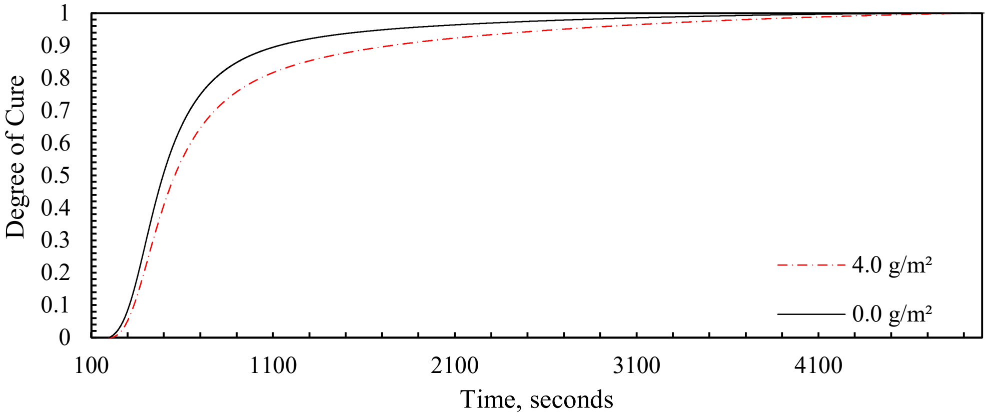

b.

Figure 22: a) Exotherm profiles of curing pGNP/CRFP and neat CRFP under isothermal heating at 135 °C; b) The degree of cure over time of pGNP/CRFP as compared to neat CRFP.

6.2.Raman Spectroscopy

The Raman spectra of an epoxy loaded with pGNP is shown in Figure 23. Peaks from 750-950 cm⁻¹ show C-O-C bonds, from 600-1300 cm⁻¹ show aliphatic C-C vibrations, in-plane vibrations of CH2 bonds are shown between 1400-1470 cm⁻¹, while peaks from 1500-1660 cm⁻¹ show stretching in C=C bonds, and from 2800-3000 cm⁻¹ show stretching in CH2 and CH3 bonds. The peak at ~2330 cm⁻¹ is due to atmospheric N_2 [52,53].

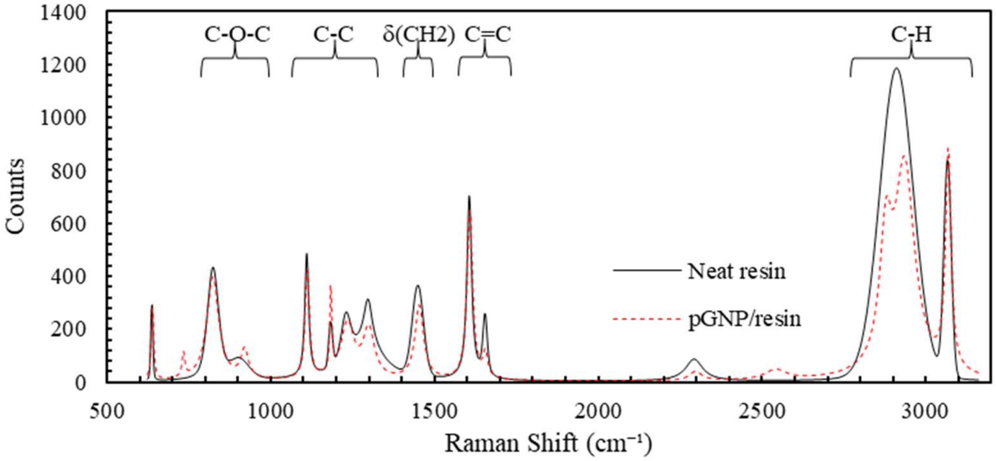

Figure 23: Raman spectra of neat epoxy and pGNP treated epoxy.

The pGNP treated composite shows a clear impact to the resin structure with impacts shown in variations of wave shift intensity at several bands. Increases to intensity at 735 cm^{-1} and 930 cm^{-1} shows an increase in stretching of epoxide bonds and increases at 1185 cm^{-1} shows an increase in stretching of C-C bonds. Strong reductions are observed at 1300, 1460, and 2900 cm^{-1} which correspond to reduction in vibrations of CH2 twisting, CH2 bending, and CH2/CH3 stretching, respectively [54]. The peak shape in the 2800-3000 cm^{-1} region has a substantially different shape with pGNP addition, showing two smaller peaks at 2880 cm^{-1} and 2932 cm^{-1} which correspond to the symmetric stretching of CH3 and asymmetrical stretching of CH2 groups, respectively [55]. This indicates that while aliphatic vibrations are reduced, some groups retain more freedom than others. Reductions in intensity at 1607 cm^{-1} correspond to reductions in vibration in C=C stretching. Other peaks have similar relative height, as well as baseline values between peaks which shows a similar overall intensity between samples. Taken as a whole, pGNP addition results in a stretching of polymer chains with a reduction of vibrations in branched groups, particularly CH2 and CH3 groups. Characteristic peaks for graphene at 1350, 1600, and 2700 cm^{-1} [56] are not noticeable due to the low concentration of pGNP in the sample. Studies with graphene oxide have shown beneficial interactions with hydroxyl groups (also shown in pGNP with XPS) bonding with epoxy matrix, providing a significant increase in interfacial interactions [28,29].

6.3.Temperature Evolution Inside of the Thick Composite

The recorded temperature evolution is a product of both through-thickness conductivity and heat of reaction. DSC testing shows a lower peak heat of reaction with pGNP which would indicate a lower peak temperature during curing while K_{33} was lowered with pGNP addition (as shown in Chapter 7), indicating a higher peak temperature. The temperature evolution was measured to evaluate how the peak temperature in a thick section will change with interlaminar pGNP. The temperature profiles of pGNP treated composites show an increase to the maximum temperature reached during curing with increasing pGNP loading, as shown in Figure 24-a. Peak temperatures are given in Table 6. A negligible difference in internal curing temperature was observed at 1.1 g/m^2 loading, after which the internal temperature rose substantially with increased loadings to a total of 9.3 °C at 4.2 g/m^2.

Table 6. Maximum curing temperature of pGNP treated composites.

Loading	*Coating density g/m^2*	*Resin mass fraction %*	*Maximum temperature, T_{max} (°C)*	*Duration of exotherm peak, t_{exo} (min)*
0.0 g/m^2	*0*	*0.0%*	*185.84*	*40*
1.1 g/m^2	*1.1*	*1.3%*	*186.35*	*41*
2.8 g/m^2	*2.8*	*3.3%*	*191.36*	*46*
4.4 g/m^2	*4.2*	*4.9%*	*195.16*	*47*

This corresponds with the specific gravity of the cured composites, shown in Table 7. There was no increase in void volume at 1.1 g/m^2 loading, but 4.2 g/m^2 loadings produced a void fraction of 0.08. Similar void formation has been shown in other work [102]. This void formation is connected to reductions in thermal and electrical conductivity, as well as flexural modulus, which has not been investigated as a mechanism in studies with comparable results [101].

Table 7. Specific gravity and void fraction of composites

Loading	*g/ml*	*Void Fraction*
0.0 g/m^2	1.443 ± 0.051	*0.000*
1.1 g/m^2	1.470 ± 0.017	*0.000*
2.8 g/m^2	1.340 ± 0.017	*0.077*
4.4 g/m^2	1.337 ± 0.040	*0.080*

There is also a slight delaying of the exothermic cycle with increased loading and a decreased exotherm with increasing pGNP content, visible from the time versus temperature profile. As the loading increased, the duration of the period in which core temperature exceeded oven temperature increased from 40 min for the neat sample to 41 min for 1.1 g/m^2, 46 min for 2.8 g/m^2, and 47 min for 4.2 g/m^2 loadings, as shown in Figure 24-b. This corresponds with isothermal DSC results (shown in Figure 22) which show a similar delaying and elongation of the exothermic cycle with interlaminar pGNP. The lower heat flow peak in pGNP composites from DSC is opposite to the higher temperature peak which was observed during the thick laminate cure. These results show the combined impact on curing temperature from change to curing kinetics and void formation, both of which result from chemical interaction between the pGNP and the resin system.

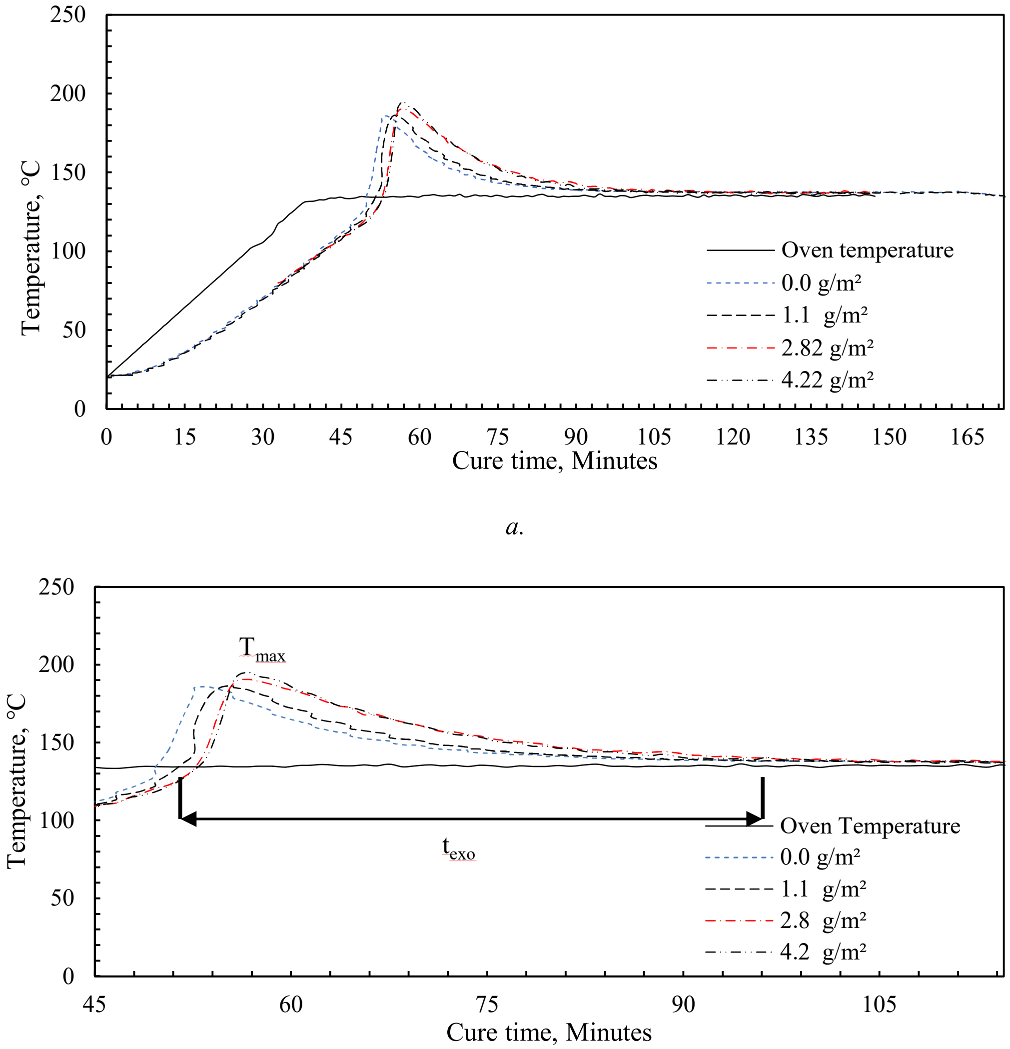

a.

b.

Figure 24: a) Exotherm profiles of curing composite blocks at various graphene loadings, with the oven air temp as a reference; b) Details of the exotherm duration and peak temperature are shown.

6.4. Discussion

Isothermal and dynamic DSC both show that pGNP addition reduces the peak heat flow and extends the curing time of the composite. This behavior is the first confirmation of a chemical interaction between pGNP and the epoxy matrix which is confirmed with Raman spectroscopy of the cured pGNP/composite system. The degree to which this is a result of energy going into crosslinking with SFGs as compared to energy in crosslinking reactions mediated by pGNP is a subject for further study. The changes in peak heights and positions in Raman Spectroscopy show significant interaction between pGNP and the epoxy matrix, particularly around showing stretching of backbone aliphatic carbon chains in the polymer and reduction of vibration of branched side-chain groups.

The reduction in peak heat flow—shown by DSC—would suggest that peak cure temperatures would be reduced by pGNP, however the peak curing temperature increased with pGNP loading as a result of higher void content. Increased pGNP loading did increase the exotherm duration, which corresponds with the longer exotherm shown in DSC. XPS and SEM in Chapter 4 show that pGNP is distinct from exfoliated mineral GNP in morphology and functionality. The presence of carboxyl and epoxy functional groups contribute to crosslinking and reenforcing of resin as shown in every test performed. The interaction between pGNP and resin curing is given further attention in Chapter 7, as it plays a role in improved pGNP/epoxy material properties. The relation between phenomenon in curing and with mechanical performance highlights the multifunctional interactions of pGNP. The impacts of pGNP addition on thermal conductivity, which play a key role in the temperature evolution inside of the thick composite section are addressed in Chapter 8.

CHAPTER 7

MECHANICAL PERFORMANCE

This chapter discusses the results of investigation on the mechanical properties of pGNP/CFRP. Work in Chapter 6 showed evidence of chemical interactions between pGNP and the curing resin, the nature and impact of those interactions will be explored in detail herein. The goal of this work was to test mechanical properties at ambient and elevated temperatures to provide insight into pGNP/epoxy interactions which would otherwise be unclear. Additionally, two of the primary weaknesses of fiber reinforced composites (as compared to traditional materials) are poor interlaminar toughness and weakness at elevated temperatures [16]. Temperature studies have been underrepresented in literature [20], despite the temperature dependence of fracture resistance and its criticality to many applications. To this end, investigating the performance of pGNP/CFRP at elevated temperatures is especially valuable. Thermo-mechanical characterization of viscoelastic properties was done using Dynamic Mechanical Analysis (DMA). Mechanical characterization included flexural beam testing, interlaminar shear strength using short beam testing, Mode I and Mode II fracture toughness testing. Fracture surface micrography was used to quantify mechanisms of fracture toughness improvement. These methods present a comprehensive investigation of graphene induced improvements on the thermo-mechanical properties of CFRP at ambient and elevated temperature.

7.1.Dynamic Mechanical Analysis

Results from DMA testing in a three-point bending configuration for neat CFRP beams and beams with interlaminar pGNP are shown in Figure 25. The glass transition temperature, T_G, as measured by the peak of the extensional loss factor, *tan(δ)* [134], is measured at 122.5°C for both the neat and pGNP treated composite while the onset of the glass transition region is slightly delayed for the pGNP treated composite at 112.5°C vs 110°C for the neat composite.

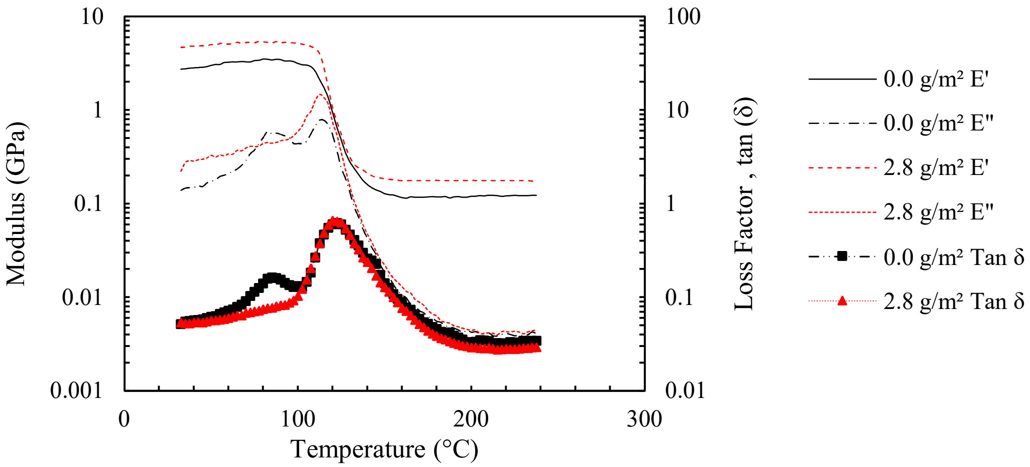

Figure 25: DMA analysis of neat CFRP and pGNP/CFRP at 2.8 g/m².

The storage modulus, *E'*, in pGNP/CFRP is 63% higher before the glass transition and 47% higher after the glass transition. The increase in E' shows that pGNP/epoxy nanocomposite in the interlaminar region has a higher stiffness and improves the load transfer between fibers and matrix in the interlaminar region, which is responsible for the interaction between the plies in both the glassy and rubbery states. This result, at 2.8 g/m² (1.2% w/w) is comparable to reinforcement using hexagonal boron nitride and molybdenum disulfide at 6% loading [135]. The more notable impact of pGNP addition is related to a hump in the tensile loss modulus, *E"*, and loss factor, *tan(δ)*, that peaks at 85°C. This early peak has been defined as the Beta Transition, T_β, which—in bisphenol-A based thermosets such as those in this study—is related to molecular movement of side chains and unreacted ends of the polymer [136]. T_β is known to be related to fracture toughness [137]. Multiple peaks in the loss modulus have been shown in multiscale composites such as CFRP previously [138,139], and it has been shown that the use of a filler which interacts with the epoxy matrix can reduce the earlier tan(δ) peak value [140]. The use of MWCNT reduced the early peak in loss modulus by restricting the molecular motion of polymer chains resulting in higher elastic response and a lower relative viscous response [139]. The addition of 2.8 g/m² of pGNP in this case results in the elimination of the T_β peak in viscous response as a result of pGNP restricting side chain movement in the polymer. This behavior was attributed to the high size and aspect ratio of nanoparticles and chemical interaction between GNP and polymer as shown by Raman spectroscopy. Raman spectra shown in a previous section indicated the stretching of polymer chains and a reduction of branch vibrations that correspond to the restricted chain mobility, and, as a result an increase in the loss modulus in the T_β temperature range is observed in GNP composite. Through these mechanisms, while T_G is not increased the performance the CFRP system at temperatures approaching T_G in the T_β temperature range can be substantially improved. Because the glass transition is a result of large-scale movement in the polymer backbone rather than independent side chain movement in the beta transition [136], we can infer that pGNP addition is minimally effective at reducing bulk chain movement in the polymer, while affecting local interlaminar property where pGNP is introduced. Further study is required to assess the impact on mechanical properties of pGNP addition at temperatures from T_β to T_G. The implication of this result to the mechanical properties will be discussed in the following sections.

7.2.Flexural Beam Testing

The flexural modulus and strength of the pGNP treated composites were increased at 1.1 g/m^2 loadings, as shown in Figure 26-a, by 15% and 17%, respectively. Representative results of the three-point bending test are shown in Figure 26-b. At higher loadings the modulus decreases below the untreated value by 16% and the strength plateaus with a 12% increase. The peak values at 1.1 g/m^2 correspond to the increase in void volume with higher loadings, as the void fraction begins to offset or overcome improvements from the pGNP addition.

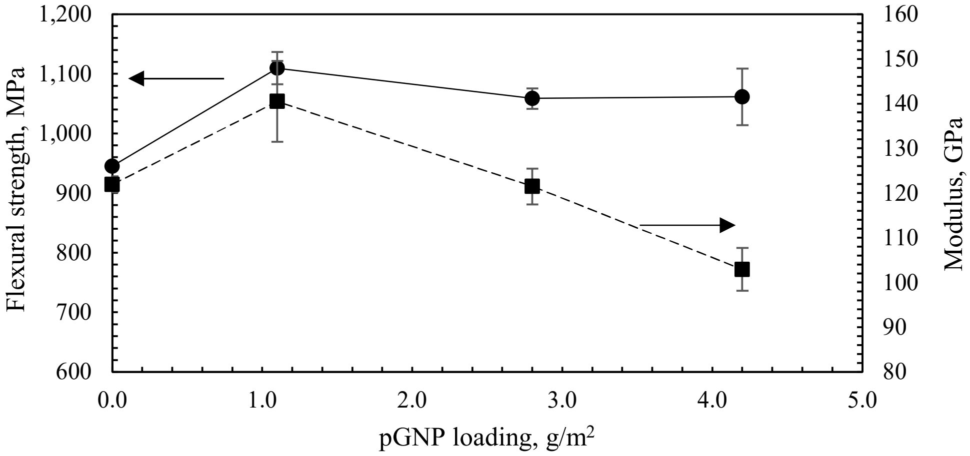

a.

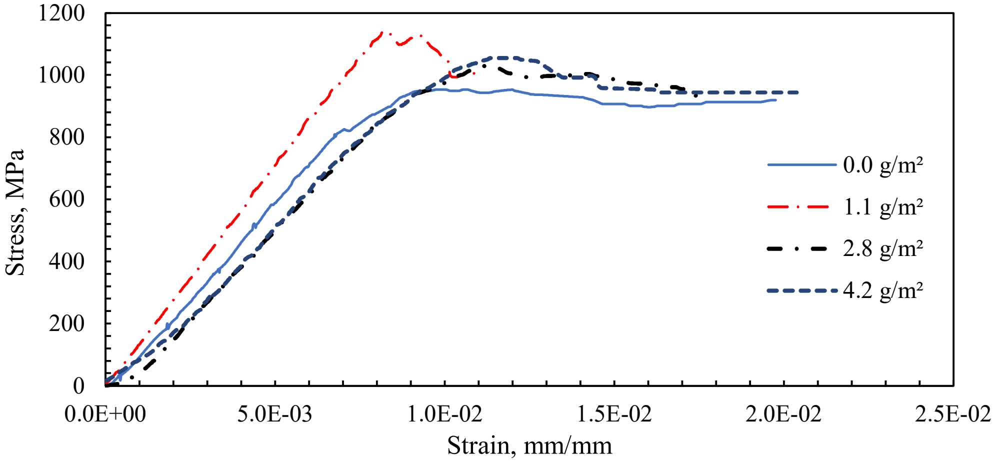

b.

Figure 26: a) Flexural strength and modulus of pGNP treated composite beams; b) Representative stress-strain curves for flexural tests.

7.3.Short Beam Testing

Short beam test results are presented in Figure 27-a, with representative results shown in Figure 27-b. At 20°C, 2.8 g/m^2 loading of pGNP improved ILSS (F_{31}) of composites by 17% over neat samples while 4.2 g/m^2 loading resulted in a 6% increase. At 90°C, ILSS decreased for neat samples by 14%, at 4.2 g/m^2 there was an 8% increase in ILSS, while 2.8 g/m^2 did not show any change from neat samples. The slope of the stress-strain curves in pGNP/CFRP was 17% higher than neat CFRP and the slopes were ~38% lower at 90°C than at 20°C. The peak in ILSS improvement for the room temperature at 2.8 g/m^2 was used to target loading for Mode I and Mode II fracture.

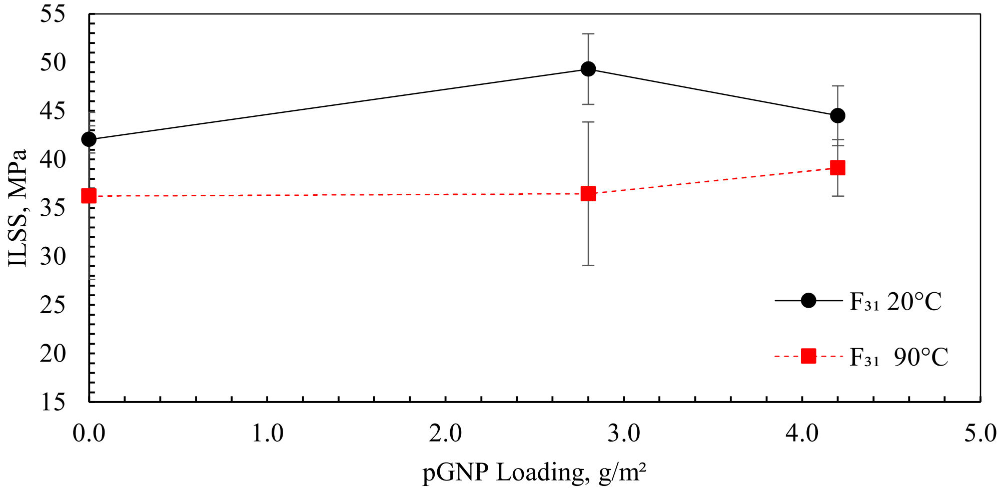

a.

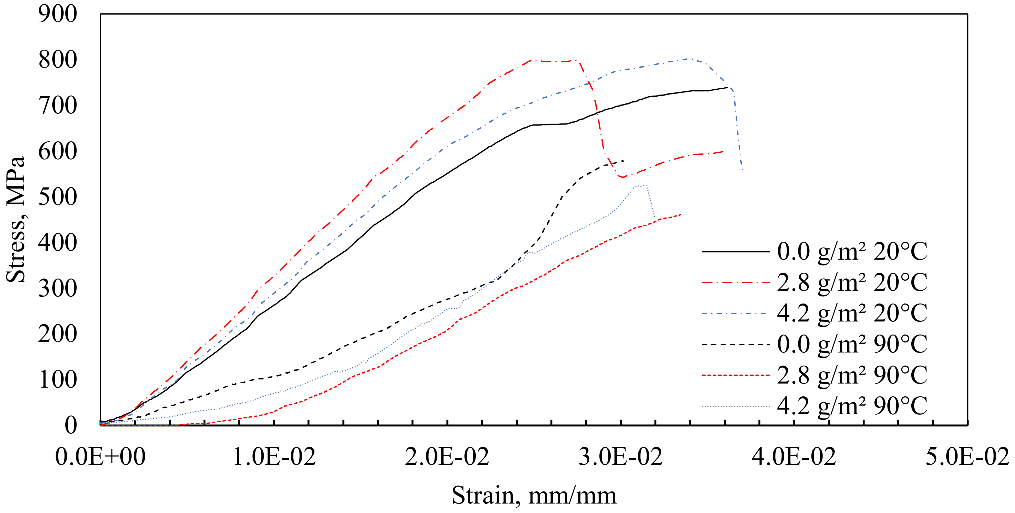

b.

Figure 27: a) F_{31} values for CF/epoxy beams at 0.0, 2.8, and 4.2 g/m^2 pGNP loadings at 20°C and 90°C; b) Representative stress-strain curves for ILSS testing at 20°C and 90°C.

Increases to ILSS are expected as the interlaminar strength is a property of the load transfer between plies where pGNP is able to contribute to the interlaminar reinforcement—which dominates the interlaminar load transfer—and provide crack deflection mechanisms [51], as discussed later in fracture toughness results. Reductions in ILSS at 90°C stand in contrast to later results where fracture toughness is maintained however ILSS is improved at 4.2 g/m². While short beam testing is a widely used method for measuring ILSS due to its simplicity, the results are impacted by non-uniform stress distributions and potential changes in the failure mode at elevated temperature. An alternate method such as the Double Notched Shear Test or Arcan Test may be more accurate for high stiffness fiber composites at elevated temperatures [141].

7.4.Mode I Fracture

Figure 28 shows representative Load-Displacement curves for composite samples in the four conditions tested, showing the improved performance of the CFRP with pGNP interlaminar addition over untreated CFRP, and the relative performance at 90°C. Average dimensions and compliance values from the test beams are given in Table 8.

Table 8. Average DCB test dimensions

Sample	*Mode I a_0 (mm)*	*Thickness, 2h (mm)*	*width, b (mm)*	*n*
0.0 g/m² 20°C	*49.5*	*3.8*	*18.7*	*2.56*
0.0 g/m² 90°C	*54.3*	*3.8*	*17.1*	*2.71*
2.3 g/m² 20°C	*49.8*	*4.1*	*21.4*	*3.03*
2.3 g/m² 90°C	*50.2*	*4.1*	*21.3*	*2.83*

Results for the mechanical testing of pGNP/CFRP and neat CFRP composites are presented in Figure 29. It was found that, at 20°C, the pGNP treated samples were 146% tougher than the untreated samples at initial crack extension. Values are shown in Figure 30 and Table for G_{IC} on initiation, (measured during initial crack extension) and G_{IC} on propagation (averaged over the first 25 mm of crack extension).

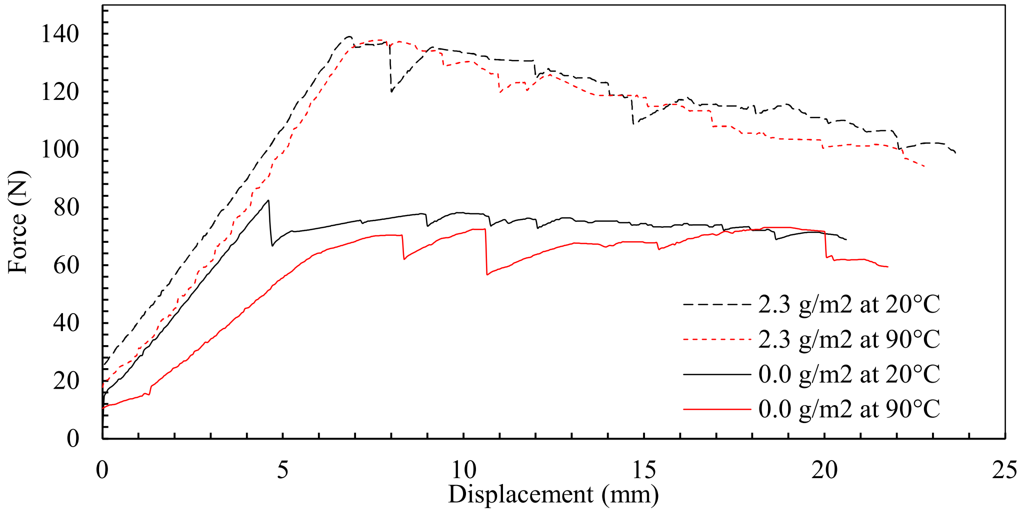

Figure 28: Load-displacement curves for representative fracture tests of untreated CF/epoxy composites and 2.3 g/m^2 pGNP interlaminar spray at 20°C and 90°C.

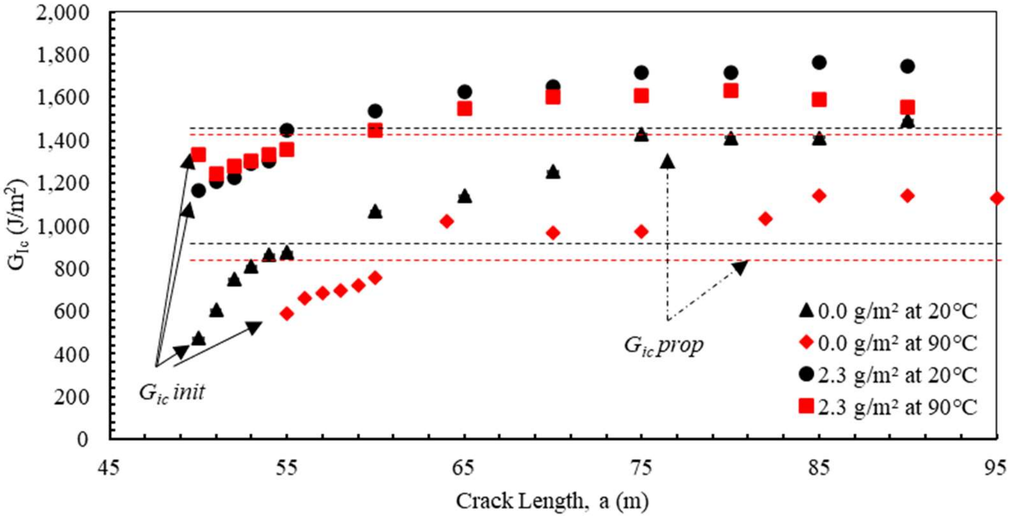

Figure 29: G_{IC} values for CF/epoxy beams without treatment and with 2.3 g/m^2 pGNP interlaminar spray at 20°C and 90°C.

Fracture resistance during extension was 53% greater in the pGNP treated samples. In the case of viscoelastic material, the energy release rate, G_C, which is measured during crack extension consists of two components: the stored elastic strain energy, which is released as a crack grows, and dissipated energy component, as shown in Equation 13 [142].

$$G_C = \frac{dW(E')}{da} + G_{Dis}(E'') \tag{13}$$

where dW represents the incremental work done on crack extension, da. Stored elastic energy is a function of the storage modulus, E'. While the loss modulus, E'', is representative of the viscous component of the dynamic modulus and is related to G_{Dis}, which describes the energy dissipation due to viscous effects and plasticity.

Table 9. G_{IC} values

	G_{IC} Initiation(J/m^2)			G_{IC} Propagation(J/m^2)		
Sample	*Mean*	*Std Dev*	*% Change*	*Mean*	*Std Dev*	*% Change*
0.0 g/m² 20°C	*474*	*97*	*0%*	*928*	*254*	*0%*
0.0 g/m² 90°C	*588*	*39*	*24%*	*809*	*111*	*-13%*
2.3 g/m² 20°C	*1163*	*96*	*145%*	*1416*	*140*	*53%*
2.3 g/m² 90°C	*1332*	*144*	*181%*	*1406*	*250*	*52%*

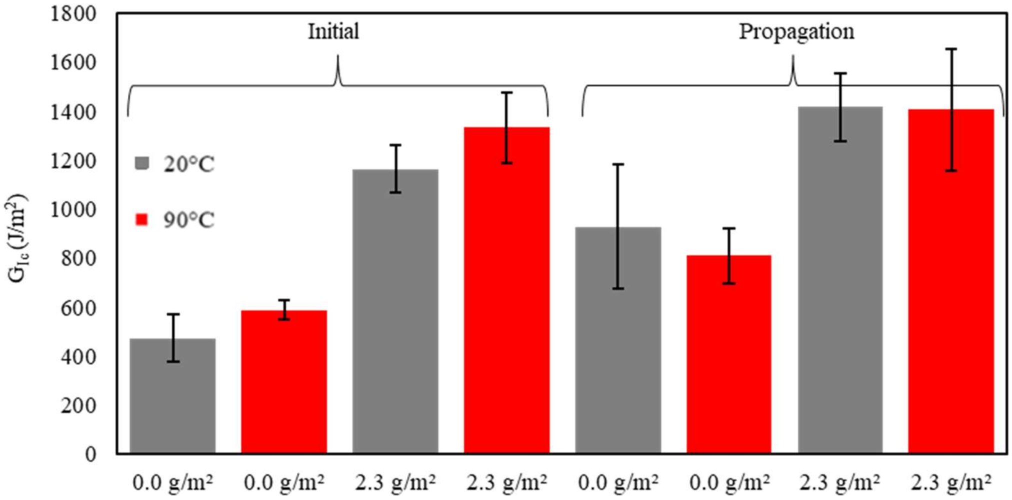

Figure 30: Average G_{IC} values for CF/epoxy beams without treatment and with 2.3 g/m² pGNP interlaminar spray at 20°C and 90°C on initial fracture and during crack propagation.

The propagation values of G_{IC} for pristine, 0.0 g/m², CFRP at ambient temperature were significantly higher than at initiation. Typically, increase in G_{IC} with crack extension represent fiber bridging, an artifact of DCB testing, which depends on the fiber migration into the interlaminar region between the neighboring plies during cure [143]. Examples of fiber bridging are shown in Figure 31.

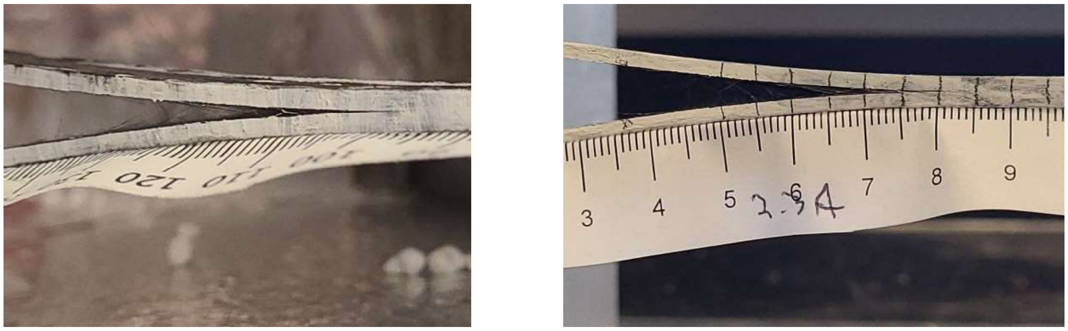

a. *b.*

Figure 31: Fiber bridging at extended crack lengths contributed to increased G_{IC} values in all samples, as shown in, a) untreated composite and b) pGNP/CFRP.

When considering temperature effect at 90°C, G_{IC} on initiation of the untreated, 0.0 g/m², CFRP is increased by 24% from the ambient values. This behavior mirrors our observations with DMA, where the increase of side-chain movement in the untreated matrix near T_β is expected to increase the dissipative mechanisms, while the stored elastic component remains nearly the same [136,137]. Increased viscous response at elevated temperature contributes to more plastic response indicative of a larger damage process zone. The increase of initial G_{IC} at 20°C for pGNP/CFRP composite compared to pristine can be attributed to the increase in E' resulting from pGNP addition to the interlaminar region, as was indicated by DMA results. Specifically, the increase in the stored elastic component at the room temperature can explain a significant 145% increase in Mode I fracture toughness. Furthermore, the addition of pGNP to the interlaminar region of the matrix provides restrictions to the thermal movement of polymer chains reducing crosslinked network mobility through the molecular interactions between epoxy and pGNP as shown by Raman spectroscopy and DMA. These interactions eliminate the early increases in E'' and extensional loss factor, tan(δ), at 85°C—prior to the glass transition region. The beta transition at T_β is related to decoherence of side chain groups and unreacted ends in the polymer. Recent work has proposed that coupling in these groups is related to energy absorption and dissipation [139]. Reduction in energy transfer through these side chain groups can be attributed to a loss in fracture toughness and improving energy transfer through the polymer side chains with pGNP improves the absorption of energy during deformation. The elimination of the beta transition as well as the slight positive shift in T_G is indicative of the improvement in the load-carrying ability of the composite with pGNP. The magnitude of loss modulus in CFRP and GNP/CFRP systems were almost identical at 90ºC. Therefore, the consistent fracture toughness at 90°C of both Mode I and—as discussed later for Mode II—can be attributed to the higher storage modulus in GNP/CFRP system at room and elevated temperature when compared with the neat CFRP. However, the reduction in the side chain mobility is not sufficient to produce higher apparent T_G as measured by DMA.

A reduction in fiber bridging may represent improvements to fiber/matrix interactions with nanoparticle additions which have been observed in other studies [7,28,144]. Studies have shown an increase in the damage process zone in GNP/CRFP systems proportional to GNP loading [69]. The damage process zone is the region ahead of the traction free crack tip which contains lots of distributed microcracks and which reflects the fracture toughness and fracture energy [145]. The larger process zone results in greater roughness of the fracture surface, shown in previous studies where the relatively higher strength of the GNP causes the crack front to tilt and/or twist from its initial plane [69]. Surface micrographs of fracture surfaces from beams tested at 20°C, as shown in Figure 32, show a substantial increase in surface roughness. The zero point in surface roughness measurements was obtained from focusing on the flat region of the Teflon insert, prior to crack extension. The increase in roughness represents an elongation of the crack path as a result of nanoscale reinforcement from pGNP addition, which causes crack deflection. The elongation of the crack front increases the energy required to extend the crack, raising the fracture toughness of pGNP treated composites at ambient and elevated temperatures.

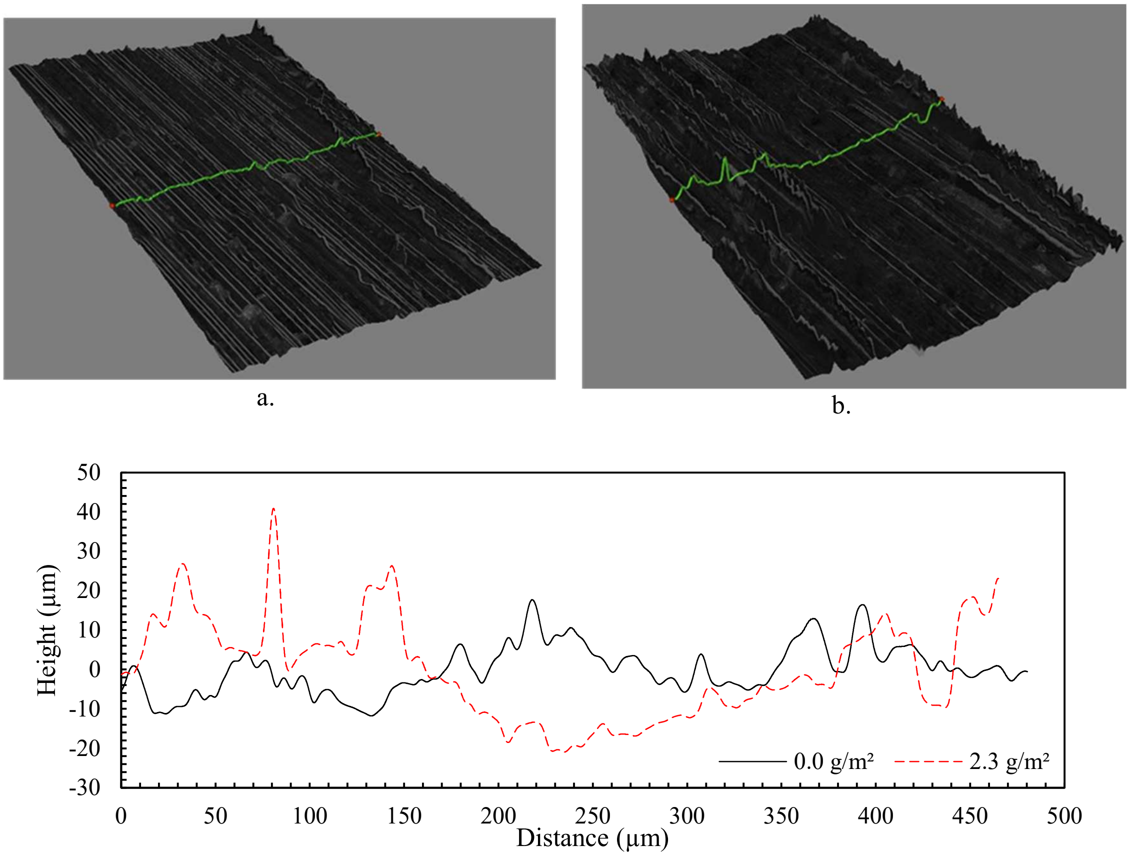

a.

b.

c.

Figure 32: The scanned area of (a) untreated beam fractured at 20°C and (b) pGNP/CFRP beam fractured at 20°C; c) the micrographs for untreaded CFRP and pGNP/CFRP.

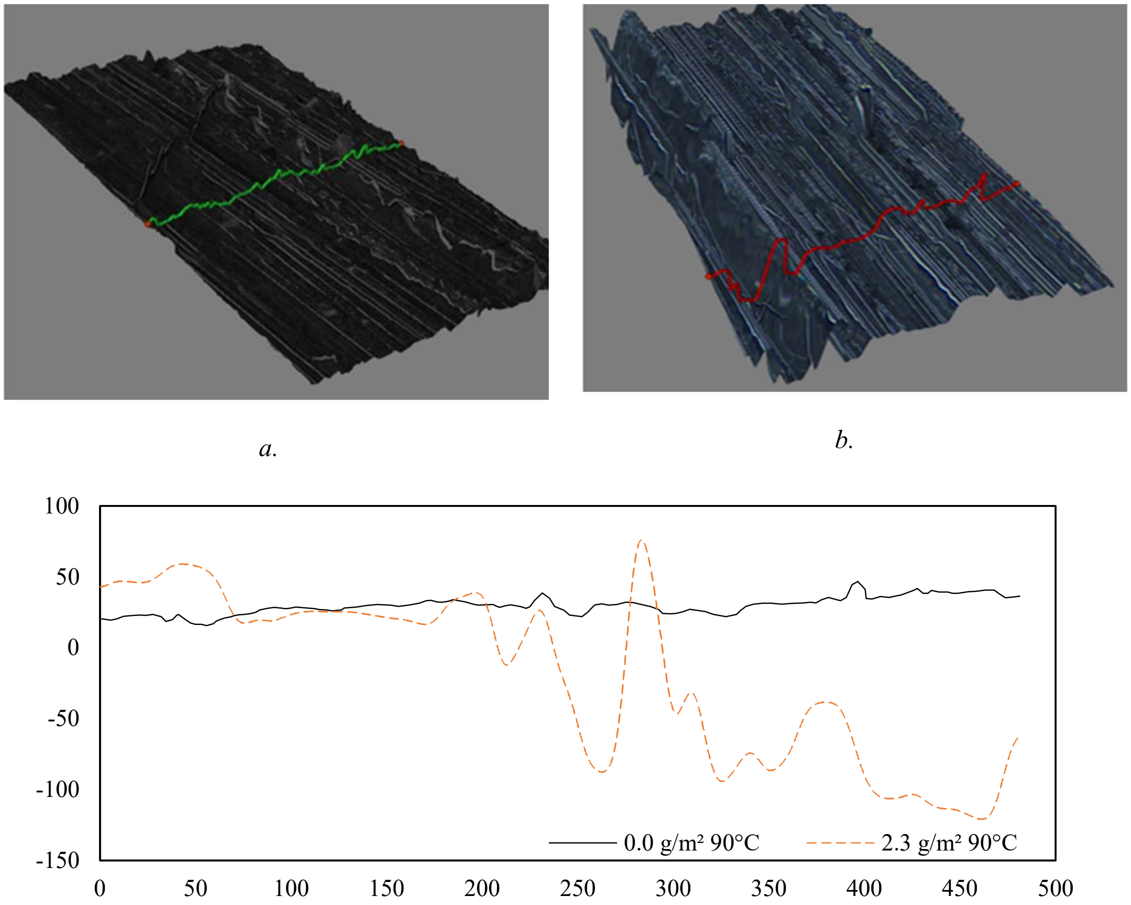

a.

b.

c.

Figure 33: The scanned area of; a) untreated CFRP fractured at 90°C and b) pGNP/CFRP beam fractured at 90°C; c) the micrographs for an untreaded CFRP and pGNP/CFRP beam.

Fracture surface micrographs of DCB samples treated at 90°C (Figure 33) show similar behavior with a significant increase in crack surface roughness and crack front elongation in pGNP treated samples versus neat samples at 90°C, with a respective decrease in roughness for neat samples as compared to ambient fracture tests. The consistent physical properties of the pGNP treated composite at 90°C are shown with the high degree of surface roughness which is representative of the increased energy required to extend the crack front in the elastic matrix.

7.5.Mode II Fracture

Results for the end notch flexural testing of neat and pGNP treated CFRP are presented in Figure 34. The Mode II interlaminar fracture toughness, G_{IIC}, of composites with and without pGNP interlaminar spray were equivalent at 20°C, which is consistent with other studies [69]. While GNP addition has shown consistent improvement in Mode I fracture to varying degrees, GNP impact on Mode II fracture has been mixed. While some studies have shown strong toughening [27,50], other studies have shown a lack of improvement [69] or loss of performance [73]. As reported in a previous study, ENF Mode II testing produces an inherently unstable crack propagation in displacement control mode. Therefore, the reinforcing GNP effect at the room temperature is restricted by relative brittleness of epoxy CFRP and the instantaneous crack growth, in contrast to Mode I where stable crack growth is achieved in displacement-controlled mode. The brittle behavior of thermosetting network is due to a small damage process zone around the crack front where the damage occurs prior to crack propagation. [130,143].

Table 10. Average ENF test dimensions

Sample	*Mode II a_0 (mm)*	*Thickness, 2h (mm)*	*width, b (mm)*	*m*
0.0 g/m^2 20°C	*30*	*3.9*	*17.4*	*0.0277*
0.0 g/m^2 90°C	*30*	*3.9*	*17.7*	*0.0358*
2.3 g/m^2 20°C	*30*	*4.1*	*21.4*	*0.0188*
2.3 g/m^2 90°C	*30*	*4.1*	*21.3*	*0.0189*

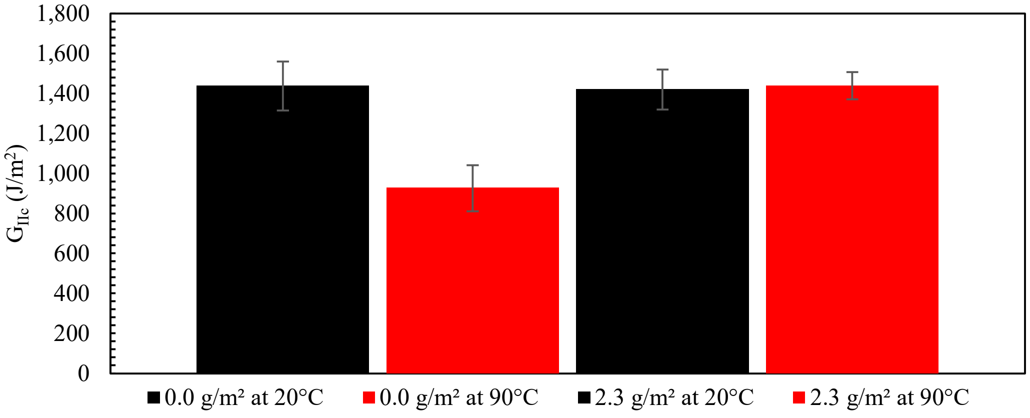

Figure 34: G_{IIC} values for CF/epoxy beams without treatment and with 2.3 g/m2 pGNP interlaminar spray at 20°C and 90°C.

The lack of significant Mode II toughening at room temperature in pGNP/CFRP composite is due to relative brittleness of the matrix and inherently unstable crack propagation. Similar results have been discussed in other studies using GNP/CFRP composites [69,146]. Examples of improvement of Mode II fracture have utilized methods of improving the GNP interaction with the matrix [50]. At 90°C, untreated composite beams showed a 34% reduction in fracture toughness while pGNP/CFRP showed no notable change in Mode II fracture toughness. This corresponds with other work, which shows that at elevated temperature matrix softening leads to reduction of certain composite properties, specifically intralaminar shear strength and stiffness, which in turn reduce Mode II fracture toughness [146]. Average dimensions and compliance values from the test beams are given in Table 10. At 90°C, the presence of pGNP provides the increase of the composite properties, as indicated by DMA results, which produced significant effect for increased Mode II fracture toughness in pGNP/CFRP system. This performance at elevated temperature is consistent with Mode I fracture results, showing the effect of pGNP as a nanoscale reinforcing material in the interlaminar region.

7.6. Discussion

pGNP interacts with the chemical bond structure and viscoelastic behaviors of the epoxy matrix of CFRP. DMA shows that pGNP interacts with the epoxy polymer to eliminate the T_β peak in loss modulus by restricting the molecular motion of polymer side chains resulting in higher elastic response and a lower relative viscous response, while increasing the elastic modulus. As shown in Chapter 5, Raman spectroscopy demonstrates chemical interaction between pGNP and epoxy, showing stretching of epoxide aliphatic carbon bonds along the backbone of the polymer while reducing the vibration of branched groups. These interactions are key to improving mechanical performance at both ambient and elevated temperatures.

DMA testing shows a 63% increase in *E'* in pGNP/CFRP at ambient conditions, which shows that pGNP/epoxy nanocomposite in the interlaminar region has a higher stiffness and improved the load transfer between fibers and matrix in the interlaminar region. At elevated temperatures, the onset of the glass transition region is delayed for the pGNP/CFRP to 112.5°C vs 110°C for the neat composite but T_G is unchanged at 122.5°C. DMA results also showed a 47% increase in *E'* in the rubbery state, after the glass transition temperature. This suggests mechanical improvements at temperatures above T_G which warrant further investigation.

The flexural modulus and strength of the pGNP treated composites were increased by 15% and 17%, respectively at 1.1 g/m². ILSS was improved by 17% 2.8 g/m². At higher loadings the effectiveness of pGNP addition is reduced which corresponds to the increase in void volume with higher loadings as the void fraction begins to offset or overcome improvements from the pGNP addition.

The most dramatic area of mechanical improvement is in fracture toughness, which is expected given the susceptibility of composite materials to fracture failure and the targeted, interlaminar application of pGNP where the improved storage modulus leads to fracture toughness increase at crack initiation. At 20°C, Mode I fracture is improved 146% and at 90°C, pGNP/CFRP showed G_{IC} improvements of 126% on initiation. pGNP addition provides substantial increases to the strength of the interlaminar region which—upon crack propagation—resulted in crack front deflection and elongation which—in turn—increase the energy required to extend the crack in the stable, displacement-controlled Mode I fracture. At ambient conditions Mode II fracture was unaffected by pGNP addition, due to the unstable crack propagation in displacement control mode. However, at 90°C, pGNP/CFRP showed no decrease in Mode II toughness compared to 20°C tests as a result of improved storage modulus, resulting in an overall 55% increase in Mode II toughness at 90°C.

CFRP nanocomposites typically exhibit complex internal structure-property behavior due to interactions between the different constituents. Therefore, the difference in Mode I and Mode II fracture in this study show that pGNP particles provide a direct fracture toughness reinforcement through various means: (i) matrix toughening, (ii) increased elastic properties in the interlaminar region at elevated temperature, and (iii) pGNP particle causing crack deflection. Epoxide and carboxyl functional groups, as well as nanoparticle morphology play a key role in these interactions and must be understood when designing a nanoparticle reinforced system.

Interlaminar application ensured effective dispersion and targeted pGNP loading at the critical interlaminar region. Spray application of pGNP provides a simple, controllable method of improving fracture toughness of the composite but—as highlighted in Chapters 3 and 4—surface functionality of pGNP and spray formulation are important in optimizing pGNP/CFRP. Poor interaction with the spray system would result in pGNP agglomeration and reduction in mechanical properties. pGNP functional groups played a key role in reducing side chain vibrations and in reenforcing the composite system.

CHAPTER 8

MULTIFUNCTIONAL PROPERTIES

This chapter discusses the multifunctional properties of the pGNP/CFRP system. A multifunctional composite is defined as “made of two or more materials that perform two or more functions in a manner that is constructive to the overall purpose of the structure” [147]. In this dissertation, multifunctionality is taken to refer to a combination of structural and non-structural roles. Electrical conductivity (EC) has several applications in composite structure including; electrical grounding, EMI shielding, lightning strike protection, structural health monitoring, and energy storage [54,57,101]. Thermal conductivity (TC) is important for heat dissipation and temperature tolerance [148]. To this end, investigating the thermal and electrical conductivity of pGNP/CFRP in the three principal material directions and at increasing temperatures provides fundamental information on how multifunctional properties can be achieved. EC was measured using a 4-point kelvin probe. TC was measured using a two-sensor heat flux test. Both tests measured unidirectional composites in the three principal material directions, across the sample in the fiber direction (1), perpendicular to the fiber direction (2), and in the out-of-plane direction across the composite thickness (3). Measurements were taken at 30ºC, 50ºC, 70ºC, and 90ºC.

8.1.Electrical Conductivity

The impact of interlaminar pGNP addition varies with respect to fiber orientation and testing temperature as shown in Figure 35. EC values at 30°C are shown in Table 11. EC was increased with increased pGNP loading but the behavior varied depending on the axis of measurement. At 30°C, in the fiber direction (κ_{11}), EC increases linearly up to 2.8 g/m^2 for a 202%, after which it plateaus as the percolation threshold is reached. In the transverse and cross plane directions (κ_{22} and κ_{33}) EC peaks at 1.1 g/m^2, with improvements of 397% in κ_{22} and 168% in κ_{33}. The impact of void formation is clear given that at 2.8 g/m^2 both EC values decrease before rising slightly at 4.2 g/m^2.

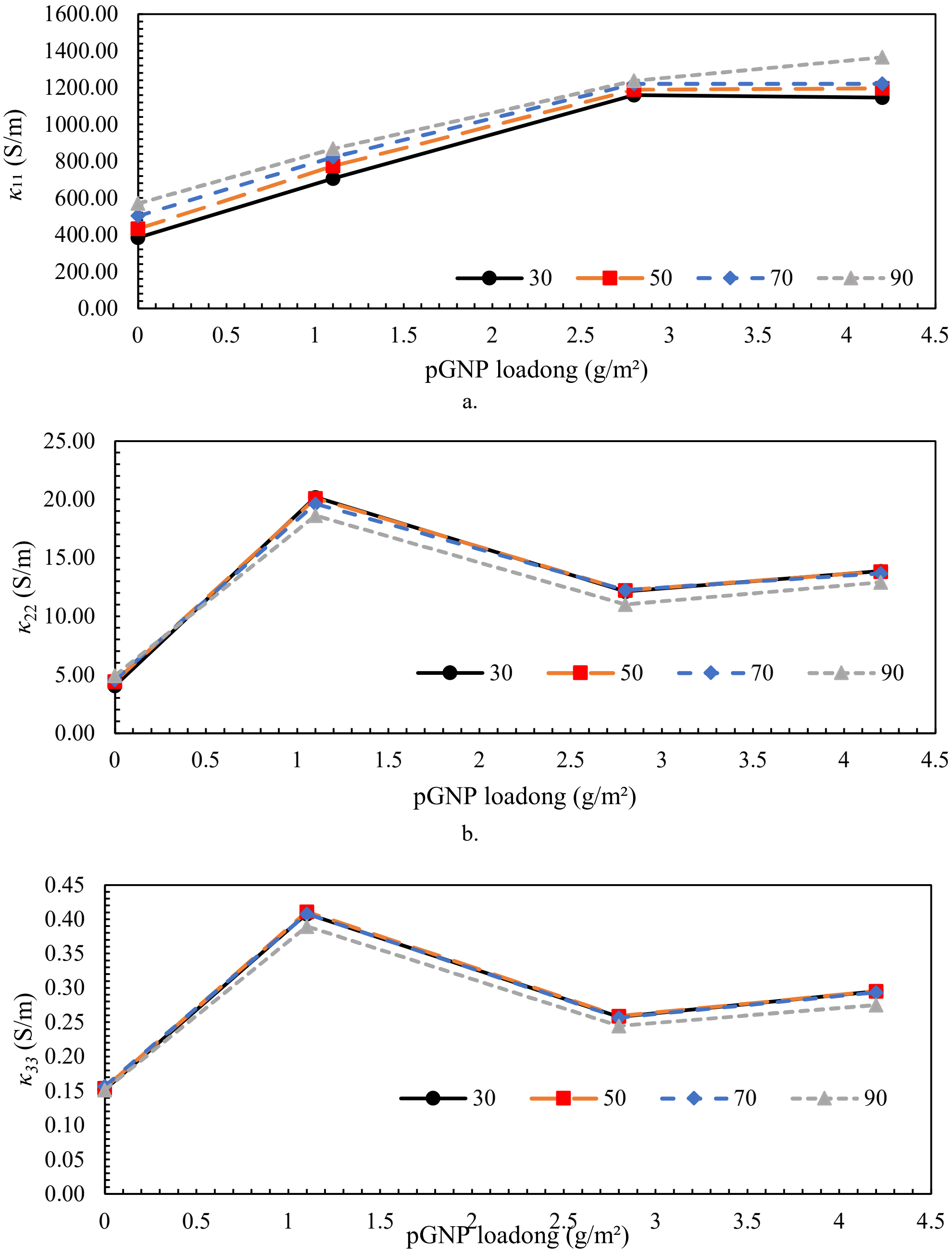

a.

b.

c.

Figure 35: The Electrical conductivity of CFRP composites with increasing interlaminar pGNP from 0-4.2 g/m² at temperatures from 30-90ºC; a) in the fiber direction (κ_{11}); b) transverse to the fiber direction (κ_{22}), and; c) through the composite thickness (κ_{33}).

There is a notable anisotropy in the effect of temperature on EC. κ_{11} increases linearly with temperature from 0-2.8 g/m² loadings of ~2.5 S/m·°C. At 4.2 g/m² there is a noteworthy increase in EC at 90°C as the increased temperature appears to increase the percolation threshold of the composite. κ_{22} and κ_{33} remained approximately consistent with temperature from 30°C-70°C before decreasing slightly at 90°C. The Coefficient of thermal expansion was measured for the tested composite specimens and was a consistent 0.0137 $°C^{-1}$ in all dimensions.

Table 11. Electrical Conductivity at 30 °C

	EC (S/m)		
pGNP Loading (g/m^2)	κ_{11}	κ_{22}	κ_{33}
0	*384.4033*	*4.064224*	*0.15224*
1.1	*705.8968*	*20.18891*	*0.408126*
2.8	*1160.337*	*12.12062*	*0.257741*
4.2	*1146.053*	*13.85268*	*0.294849*

8.2. Thermal Conductivity

The impact of pGNP addition varies with respect to the fiber orientation and sample temperature as shown in Figure 36. In neat CFRP, TC in the fiber direction (k_{11}) at 90ºC increases 3% over 30ºC while TC in the transverse (k_{22}) and through thickness (k_{33}) directions decrease 3% and 7%, respectively. Loading at up to 2.8 g/m^2 increases k_{11} 27%, while increased loading at 4.2 g/m^2 reduces TC to neat values. k_{22} decreases with pGNP loading at all levels, and this decrease is heightened with increasing temperatures at higher loadings. k_{33} peaks at 1.1 g/m^2 loading with a 48% increase over neat values, returning to neat values at higher loading.

Increased pGNP loading increased k_{11} sensitivity to temperature up to 2.8 g/m^2 such that k_{11} at 90ºC is 95% k_{11} at 30ºC but this variation is absent at 4.2 g/m^2. Sensitivity to temperature in k_{22} was increased, with decreasing TC at increasing temperatures. k_{33} showed no variation with temperature at 1.1 g/m^2 while 2.8 g/m^2 loading increased k_{33} by 21% at 70ºC. At 4.2 g/m^2 loading, k_{33} was reduced 10% at 90ºC. The conflicting behaviors are interesting and warrant further study as TC in the fiber direction is dominated by pGNP/fiber interactions while through thickness TC is dominated by pGNP/epoxy interactions.

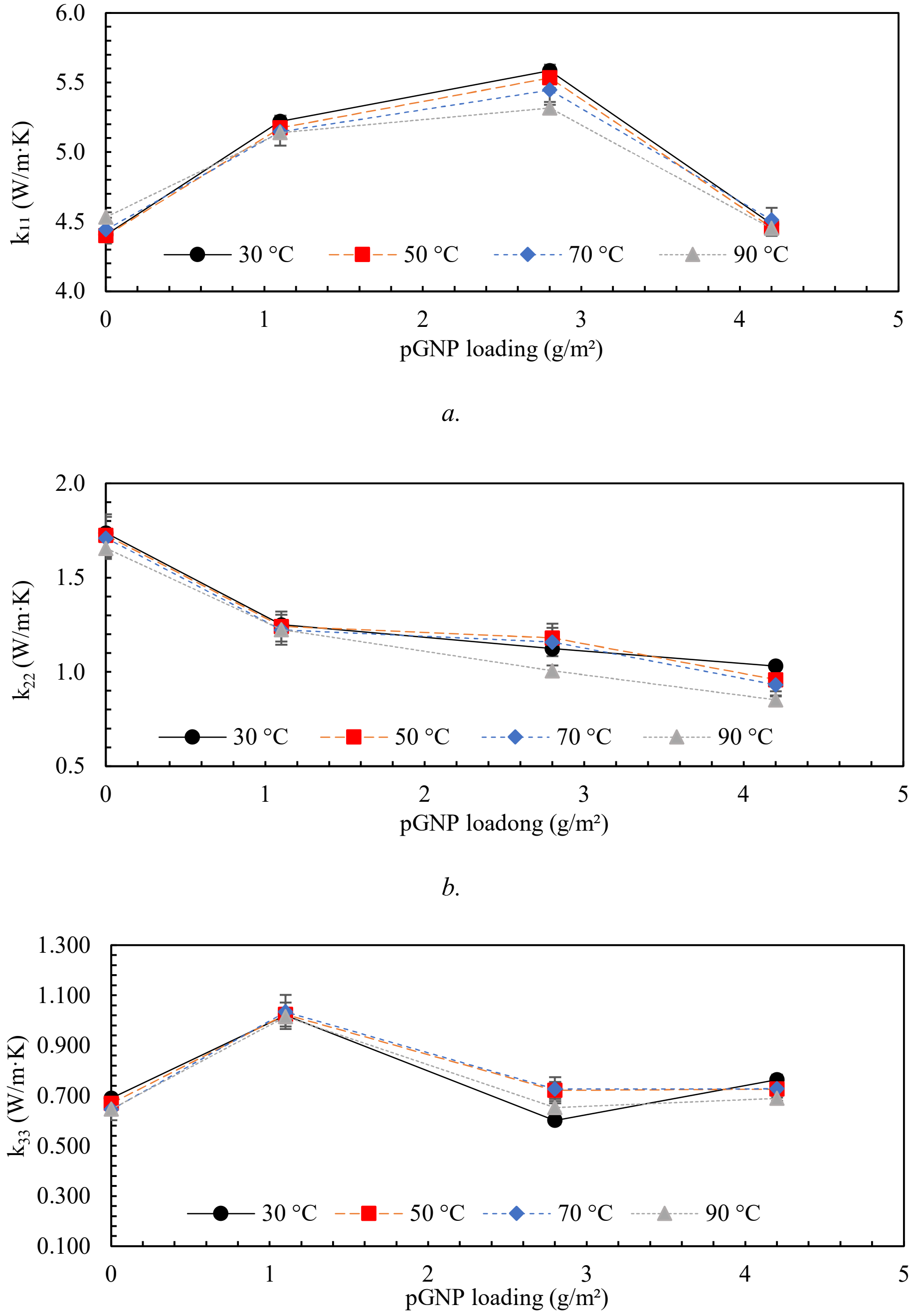

a.

b.

c.

Figure 36: The thermal conductivity of CFRP composites with increasing interlaminar pGNP from 0-4.2 g/m² at temperatures from 30-90ºC; a) in the fiber direction (k_{11}); b) transverse to the fiber direction (k_{22}), and; c) through the composite thickness (k_{33}).

8.3. Discussion

pGNP addition increased EC in each principal composite direction, with the largest relative impact to κ_{22} at 1.1 g/m² loading. This is unsurprising, as interlaminar pGNP addition is able to improve the percolation of a conductive network between conductive carbon fibers.

Increasing temperature to 90°C to increase the percolation threshold of the composite in κ_{11}. This highlights a phase change which warrants further investigation. κ_{22} and κ_{33} were unaffected by temperature from 30°C-70°C but decreased slightly at 90°C. These behaviors indicate a phase change in the composite with regards to electrical conductivity which is noteworthy when compared to the elimination of the T_β Shown in DMA. Further study of this effect and its implications is warranted.

Increases in TC at ambient (30ºC) show that pGNP particles are well distributed and have good interaction with the epoxy structure which supports the conclusions from DMA and Raman spectroscopy that pGNP particles are well distributed and bound to polymer chains. The greater proportional increase in the through thickness conductivity is expected, as the interlaminar spray is targeted in the thermally resistive interlaminar region and pGNP particles are able to percolate the region between the fibers, providing both increased TC and greater interlaminar strength. Poor pGNP/matrix interaction would be evidenced by reduced TC, which can occur at higher pGNP loadings due to particle agglomeration. Agglomeration of pGNP results in poor filler-matrix interfaces, which results in poor phonon transport at the interface and a loss in heat transfer efficiency [11]. Additionally, agglomeration reduces the overall heat conduction path [12] and can result in porosity which further reduces TC. Thermal conductivity impacts curing, elevated temperature performance, with the decreases in k_{22} and k_{33} corresponding to the increase in void formation and the higher temperatures observed during curing tests. As such, it is important to consider the TC of a GNP as an indicator of GNP distribution and interface between the CNP and the matrix.

Composite samples in this study were unidirectional in order to examine the behavior in three axes with respect to the fiber direction. The potential of engineered anisotropic conductivity is apparent, as the sample tested shows significant anisotropy in thermal and electrical conductivity. Likewise, the potential to produce composites with increased EC without increased TC is indicated, and further examination of pGNP/matrix interactions which increase and interfere with EC and TC are warranted. As such, it is important to consider TC and EC of a GNP/CFRP in the three principal directions individually.

Examining conductive behavior with stacking sequences more representative of manufactured composite parts or with woven fiber composites would be informative. Likewise, examining the impacts of a glass fiber composite system would remove the conductivity of the carbon fibers and would give different behavior in each of the material directions.

CHAPTER 9

FUNCTIONAL COATINGS FOR PA6/GLASS FIBER ORGANOSHEET

This chapter discusses work in-progress focused on applying pGNP coatings to PA6/Glass Fiber Organosheet to impart multifunctional properties. The use of an organosheet presents a distinct contrast to prior work with CFRP prepreg materials which is useful in presenting a wider description of pGNP application to a wider range of material systems. Glass fiber does not have the same electrical or thermal conductivity as carbon fiber, and inter-fiber percolation with pGNP will not be a factor in increasing conductivity. Additionally, this dissertation has shown that interlaminar pGNP with thermoset prepreg provides significant interaction between pGNP and the polymer [149,150]. Engineering a pGNP/PA6 system presents several distinct challenges since PA6 is a thermoplastic polymer with relatively low surface energy compared with epoxy prepreg. The uncured epoxy surface supports adhesion with the sprayed pGNP , unlike PA6 which provides no adhesion with the sprayed particles. Additionally, curing epoxy creates opportunities for chemical interaction with the resin, where a substantial degree of the interaction responsible for mechanical and multifunctional improvements are achieved. PA6, as a thermoplastic does not undergo the curing process and does not present the same opportunities so other means must be found to integrate pGNP with the polymer as a surface layer, and so new opportunities to develop pGNP/polymer interaction must be engineered.

Strategies which are considered in this chapter include the use of ε-Caprolactam as an adhesion promoter and binding agent as well as the use of hydrochloric acid (HCl) as a surface etchant. Caprolactam is a precursor to PA6 and has been used for in-situ polymerization of GNP nanocomposites [13,14]. The amide linkages in PA6 are readily attacked by strong acids such as HCl [15]. At low levels, this damage to the polymer chains causes surface etching and an increase in surface energy which can improve spray adhesion. The combination of these factors has the potential of providing a significant improvement in pGNP adhesion.

9.1.Materials and Methods

9.1.1. Materials

In addition to the materials listed in chapter 3, PA6/Glass Fiber Organosheet was used as the base composite material and ε-Caprolactam was used in spray formulation. The present work used organosheets produced by Johns Manville in a continuous process in which woven glass fiber reinforcement was impregnated with caprolactam monomer followed by in-situ anionic polymerization to form a thermoplastic PA6 matrix with 50% glass fiber by weight. A high molecular weight PA6 matrix was obtained during the in-situ polymerization, resulting in high mechanical properties of the final composites. ε-Caprolactam was supplied by Sigma-Aldrich at 99% purity.

9.1.2. Composite Preparation

12.5 cm x 12.5 cm Organosheet samples were prepared for spray application by sanding with a maroon 3M Scotch-Brite™ pad (~360 grit) and gleaning with a degreaser. Current collectors, in the form of copper foil tape, were applied along opposite edges of the sample panels prior to spray treatment. pGNP suspensions were applied using a pneumatic, high-volume low-pressure spray gun with 0.8 mm nozzle at 30 psi. 5 coats were applied, letting each coat dry fully between spray cycles. The weight of each panel was taken before spraying and between coats to ensure even application. Light coatings were used in order to ensure uniformity and to prevent beading on the prepreg surface.

9.1.3. Surface Conductivity

Sheet resistance, commonly used to describe the conductivity of thin surfaces or films used in EMI applications, is the resistance of a square piece of a thin material with contacts made along two opposite sides of the square. Sheet Resistance, R_s is calculated using the Resistance, R, measured in Equation 11 as shown in Equation 14:

$$R_s = \frac{R \cdot w}{l} \tag{14}$$

where R_s is the sheet resistance in ohms-per-square (*Ω/sq*), *w* is the width of the sample, and *l* is the length of the sample. Because the units *w* and *l* cancel, R_s is reported in *Ω/sq* to distinguish from bulk resistance.

Resistance was measured between the two copper current collectors on the sides of the pGNP/organosheet panels, as shown in Figure 37. Current was supplied with a TEKPower™ TP3005P Programable DC power supply and voltages was measured using a Commercial Electric™ MAS830B digital multimeter across the sample.

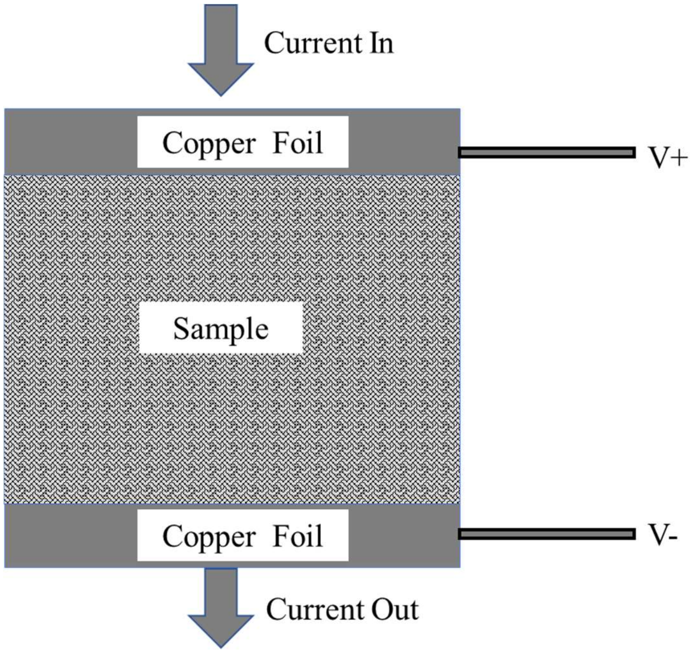

Figure 37: A schematic of the four-point probe for surface resistance.

9.2.Spray Formulation and Application

pGNP suspensions were formulated using the same DI water, 91% IPA, and 45% IPA solvents as used in Chapter 5, along with acetone, and a 50% acetone water mix which were omitted from the prepreg study due to possible negative interactions with the epoxy which are not a consideration with PA6. CMC and ε-Caprolactam were tested as dispersion aides. SDS was not included due to negative interactions with ε-Caprolactam. When dissolved in water, caprolactam hydrolyzes to aminocaproic acid, shown in Figure 38, which is also an intermediate for PA6 [153]. Aminocaproic acid is a compound with a 6-carbon chain and polar carboxyl headgroup which suggests similar behavior to SDS. In early tests, the combination of SDS and caprolactam led to excessive foaming that interfered with exfoliation. Moderate foaming was observed in caprolactam suspensions in water and alcohol, but not in suspensions containing acetone. CMC was used at the same targeted loading of 1 g/l as used in Chapter 5. ε-Caprolactam was used at a 35 g/l loading to give a 1:1 mass ratio with pGNP to provide sufficient opportunities for particle interaction.

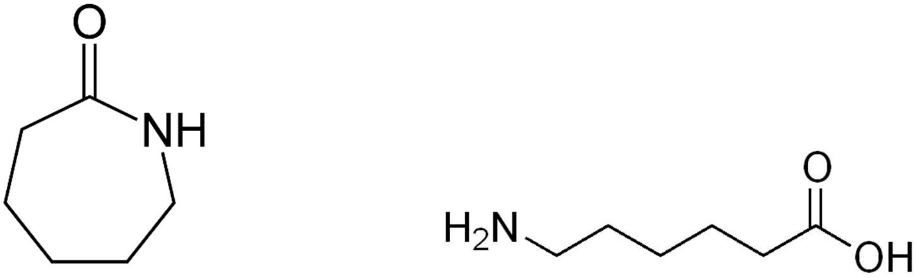

c. *d.*

Figure 38: Diagrams of; a) ε-Caprolactam and b) ε-Aminocaproic acid

Dispersion was tested following the same method as used in section 5.1, with samples mixed thoroughly and then left undisturbed to settle for 48 hours before measuring solids percentage. The dispersion of solids after 48 hours of settling is given in **Error! Reference source not found.**. The higher dispersion reported for the acetone mixtures is not representative of the same behavior as the water and IPA mixtures. When suspended solids were measured, as shown in Figure 39, pGNP dispersed with ε-Caprolactam in water produced solids which were visibly high in carbon and had an even, black color. pGNP dispersed with ε-Caprolactam in acetone—including a 50% water acetone mix—produced solids with a clear-white color, obviously primarily ε-Caprolactam with little pGNP.

Table 12. Dispersion of pGNP/ ε-Caprolactam after 48 hours settling.

	DI Water (g/l)	*45% IPA (g/l)*	*91% IPA (g/l)*	*50% Acetone (g/l)*	*Acetone (g/l)*
pGNP	*0.4*	*0.4*	*0.13*	*0.26*	*0.12*
+eC	*15.8*	*12.6*	*11.8*	*15.4*	*20.4*
+CMC+eC	*34.8*	*38.8*	*13.8*	*20.6*	*21.2*

a.

b.

Figure 39: Suspended solids from pGNP+eCapralactam in a) DI water and b) Acetone.

The behavior of the acetone suspension during solids testing coupled with the lack of foaming with acetone highlights that—even in 50% acetone solutions—ε-caprolactam is not undergoing conversion to aminocaproic acid, which appears key to interacting with pGNP.

Table 13. Contact angles of pGNP/ ε-Caprolactam on PA6 organosheet

	DI Water	*45% IPA*	*91% IPA*	*50% Acetone*	*Acetone*
pGNP	*114.2*	*147.6*	*180.0*	*146.3*	*180.0*
+εC	*113.5*	*152.5*	*157.7*	*148.9*	*166.7*
+εC+CMC	*113.0*	*151.7*	*157.9*	*149.1*	*166.0*

Surface energy was measured using CA shortly after mixing on a sheet of organosheet using the sessile drop method. As shown in Table 13, the pGNP/IPA and pGNP/Acetone dispersions exhibited the best surface wetting, with 180º contact angles. pGNP/water with caprolactam and CMC produced the lowest contact angle at 113º. pGNP with caprolactam and CMC in 45% IPA provided intermediate surface wetting with a contact angle of 151.7º. The addition of caprolactam reduced surface wetting in pGNP/IPA and pGNP/Acetone dispersions but had negligible effect on water and water mixed dispersions.

9.2.1. HCl Etching

Based on the results of suspension and surface energy testing, pGNP sprays were formulated in 45% IPA with 35 g/l pGNP and 1 g/l CMC, with and without caprolactam and with HCl at 0%, 1.2%, 2.8%, and 5.2% HCl. The results of spray tests are shown in Figure 40. Without HCl, both pGNP and pGNP+caprolactam are easily removed from the organosheet surface with light pressure. 1.2% HCl provides a significant increase in adhesion in pGNP and pGNP+caprolactam sprays. For the pGNP spray, 2.8% and 5.2% HCl resulted in significant cracking on the pGNP surface on drying, a result of contraction of the pGNP surface. For pGNP+caprolactam sprays at 2.8% and 5.2% HCl, no cracking was observed, however both sprays showed significant impact to the PA6 substrate, as evidenced by the visible structure of the glass fiber weave after spraying.

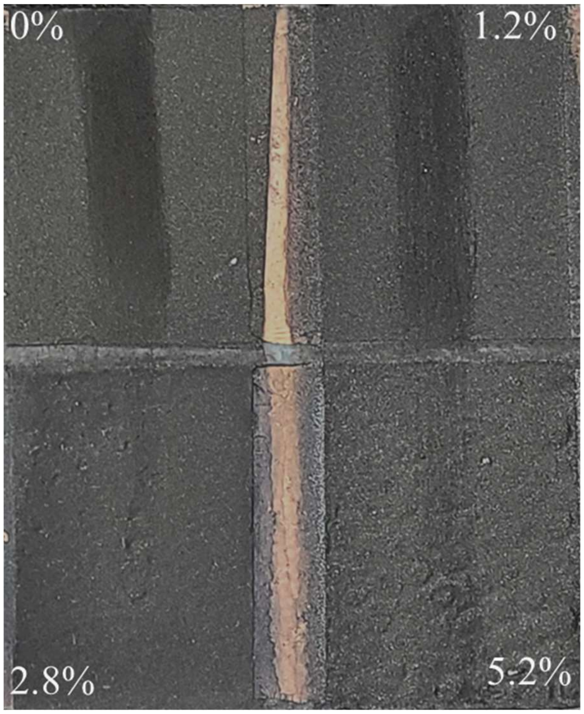

a.

b.

Figure 40: pGNP spray on PA6 organosheet a) pGNP in water/alcohol and b) pGNP+caprolactam in water/alcohol.

9.3.Surface Conductivity

The impact of pGNP addition on the organosheet surface is shown in Table 14 and Figure 41. The surface resistivity of untreated PA6 is Nylon surface resistivity $5 \cdot 10^{10}$ Ω/sq.

Table 14. Resistance and sheet resistance of pGNP sprayed PA6/GF Organosheet.

	pGNP		*pGNP+caprolactam*	
HCl%	Ω	Ω*/sq*	Ω	Ω*/sq*
0.0%	*1164*	*1552*	*2380*	*3173*
1.2%	*1100*	*1467*	*2130*	*2840*
2.8%	*1265*	*1687*	*2530*	*3373*
5.2%	*2793*	*3724*	*9960*	*13280*

Surface resistivity is minimized with the pGNP spray with 1.2% HCl at 1467 Ω/sq. The minimum surface resistivity for pGNP+caprolactam is also reached with 1.2% HCl with a value of 2840 Ω/sq. These values represent an improvement over untreated PA6 of ~$1.7 \cdot 10^7$-$3.4 \cdot 10^7$.

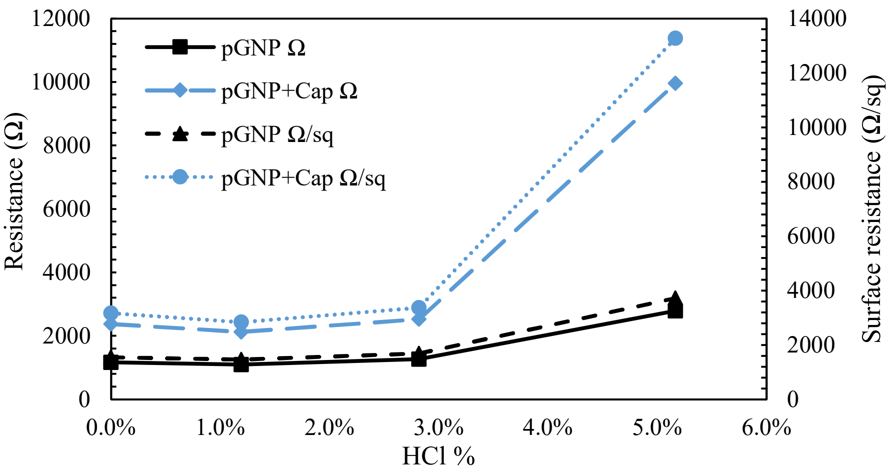

Figure 41: Resistance and Sheet Resistance of pGNP and pGNP+caprolactam spray coatings with HCl addition.

The resistivity of pGNP+caprolactam coating was consistently twice the resistance of comparable coatings of pGNP without caprolactam. This is an indication that the caprolactam is interacting with the pGNP to prevent the formation of a conductive network. The increase in resistance of the pGNP+caprolactam at 5.2% is due to the strong action of HCl in penetrating the PA6 and interfering with pGNP percolation, while the increase in pGNP is due to cracking in the sprayed surface.

9.4. Discussion

The surface resistivity of organosheet was improved by a factor of $3.4 \cdot 10^7$ with pGNP coating, giving a surface resistance of 1467 Ω/sq. The achieved surface resistivity is greater than that of metals, but within the range of conductive materials [154]. The addition of caprolactam during the pGNP exfoliation process increased the resistance of the sprayed coatings by a factor of 2. In conjunction with the behavior of the caprolactam containing suspensions in water and water/alcohol as compared to acetone, it is clear that pGNP is forming a conjugate with the hydrolyzed aminocaproic acid. Previous studies have shown the potential of in-situ polymerization of graphene with PA6 using caprolactam [27,151], and this work presents a simple pathway to the production of similar PA6/pGNP nanocomposites.

Both caprolactam and HCl were important in producing a durable, conductive surface. Etching with HCl significantly improved surface adhesion, while conversion of caprolactam into aminocaproic acid allowed for in-situ polymerization of the pGNP to prevent cracking in the pGNP surface on drying. Further work will investigate the effects of molding of the sprayed organosheet and the resulting pGNP surface. Additional work will consider spray formulations based around polyurethane to provide adhesion and durability.

The significant increase in sheet resistance has applications in EMI shielding which will be tested. Other key factors such as flame resistance, UV resistance, and scratch resistance will be tested.

CHAPTER 10

CONCLUSIONS AND RECOMMENDATIONS

GNP has substantial potential to provide improvements to the strength, electrical conductivity, thermal conductivity, and temperature tolerance of plastics and composite materials, but has yet to reach wide industrial use for reasons including cost, lack of supply, and difficulty of use. The use of a plant-based feedstock with wide availability and a manufacturing process with lower energy usage than thermal or oxidative exfoliation offers a pathway to lowering costs and increasing availability to commercially relevant levels. Difficulty in utilization of graphenes is frequently attributed to issues with agglomeration, poor distribution of particles, and poor particle/matrix interaction which the cause of the majority of GNP compounding issues [65]. This dissertation has shown that this description is an oversimplification and that careful analysis of GNP properties and understanding of nanomaterial interactions can be used to successfully engineer nanocomposite systems.

10.1. pGNP

Biomass feedstocks typically carbonize into amorphous, hard carbons [155] which do not have the high aspect ratio, aromatic bonding, or nanoscale which give graphene its properties. pGNP has all of the same properties which make mineral and CVD graphenes desirable, as well as having a morphology and functionality which are useful to applications in thermoset polymers. The biomass derived pGNP contains a higher number of SFGs as compared to mineral graphite which increase interaction with simple solvents such as water, alcohol, and acetone resulting in a GNP which can be more easily utilized in simple applications such as spray coating. Further, epoxide functional groups offer opportunities for crosslinking in a thermoplastic matrix.

Analysis from TEM, Raman spectroscopy, and XPS gives a consistent description of pGNP nanoplatelets. Raman spectroscopy shows few-layer graphitic particles with a high degree of disorder. This is confirmed with SEM and TEM which show stacked, multilayer graphene crystals. Surface analysis performed with XPS shows aromatic sp2 graphitic/graphene bonding with epoxide and carboxyl functional groups. Similar functionality is observed in reduced graphene oxide platelets [1]. Graphene oxide has a higher degree of oxidation and substantially better dispersion, but oxygenation converts sp2 bonds to sp3 bonding which removes many of graphene’s unique properties [1]. A surface C:O ratio 1.77 times higher than bulk

C:O indicates that oxygen is primarily in SFGs. The interlaminar spacing of 0.345 nm is slightly larger than the 0.335 nm spacing typical of mineral graphene, but this is consistent with the degree of surface functionalization observed with XPS.

The above characterization, along with the results of the physical testing in this dissertation show that renewable biomass feedstock can be utilized to produce a high-quality GNP. Conventional graphene production requires high purity, lump graphite with limited sources which requires energy intensive processing to produce GNP, along with environmental concerns around hazardous materials in wastewater [94]. The use of a biomass feedstock provides a renewable feedstock with opportunities for dramatic reductions in carbon emissions. The low energy cost of pGNP production and the lack of hazardous chemicals in the process creates a significant opportunity for capturing the benefits of nanomaterial addition without the environmental costs.

10.2. Spray Formulation

Utilization of GNP properties in a composite system relies on effective dispersion of GNP. Issues with agglomeration, poor distribution of particles, and poor particle/matrix interaction are the cause of many GNP compounding problems. Nanoparticle dispersion in resin has shown multiple issues with particle agglomeration during RTM. Interlaminar spray application of GNP is an effective method for composite manufacture.

Effective spray formulation required the balancing of several properties, specifically particle suspension, surface wetting, and viscosity. pGNP was shown to be more dispersible in the tested solvents than graphenes produced from mineral and synthetic graphite. This is due to polar epoxide and carboxylic functional groups which are absent in mineral graphenes. Use of plant-based dispersion aids further improved dispersion dramatically. This effect is most striking in the 45% water/IPA mixture where suspended solids are increased from 0.40 g/l for water/IPA alone to 5.61 g/l with SDS addition.

CMC addition increases the suspension viscosity at low shear rates by 30x without substantially increasing high shear viscosity. High viscosity at low shear rates prevents dripping and sagging during drying and reduces the settling of particles over time which contributes to pGNP suspension, while low viscosity at high shear rates requires less energy to spray and produces a finer atomization [63,64].

Water offers higher dispersion of pGNP than alcohol and can be a preferred choice over other solvents because of its ease of use and availability, however water has a much lower surface energy on the epoxy matrix as compared to IPA. IPA provides excellent surface wetting on the prepreg surface, as well as being highly volatile to promote fast, even drying but IPA has poorer dispersion characteristics for the pGNP. A mixture of 45% IPA and 55% water offers an effective balance of dispersibility and surface wetting. The optimized suspension did not have the highest suspension, surface wetting, or best viscosity but it does offer the best blend of these properties. CMC was used to provide benefits to the pGNP spray formulation, as a dispersion aid while improving viscosity and surface tension. SDS is added as a dispersion aide and anionic surfactant. Spray testing showed that the engineered suspension provided a means for even, low level pGNP interlaminar application as compared to a simple water spray which created a spotty, uneven coating.

10.3. Thermoset Composite Interactions

Interlaminar pGNP addition results in chemical interaction with the epoxy matrix due to activity between SFGs and crosslinking sites and polymer edge groups, as evidenced by impacts to DSC and Raman spectroscopy of the cured resin. Isothermal and dynamic DSC show that pGNP addition reduces the peak heat flow and extends the curing time of the composite. Raman spectroscopy of the cured pGNP/composite system shows changes in the relative energies stored in vibrational states in the polymer structure. This result, in combination with DSC, confirms an interaction between pGNP and the epoxy polymer on a chemical level. pGNP addition results in stretching of backbone aliphatic carbon chains in the polymer and reduction of vibration of branched side-chain groups. This substantially changes the mechanical properties of the composite, especially under heating. These results highlight the multiscale interactions of pGNP with the CFRP system and highlight mechanisms which have been overlooked in previous studies which contribute to the impacts of pGNP addition.

Reduction in peak heat flow suggests that peak cure temperatures should be reduced, however the peak curing temperature increased with pGNP loading as a result of higher void content. The void content may be a result of pGNP agglomeration but may also result from chemical interactions between pGNP and the curing epoxy. Increased pGNP loading did increase the exotherm duration, which corresponds with the longer exotherm shown in DSC.

10.4. Mechanical Reinforcement

pGNP interacts with the chemical bond structure and viscoelastic behaviors of the epoxy matrix of CFRP, providing improvements to the stiffness, strength, and toughness of the composite. DMA shows that pGNP interacts with the epoxy polymer to eliminate the T_β peak in loss modulus by restricting the molecular motion of polymer side chains resulting in higher elastic response and a lower relative viscous response, while increasing the elastic modulus. This confirms the earlier characterization using Raman spectroscopy and DSC which demonstrates chemical interaction between pGNP and epoxy. These interactions are key to improving mechanical performance at ambient temperatures but provide a substantial impact to the behavior of the composite system at elevated temperatures.

The onset of the glass transition region is delayed for the pGNP/CFRP to 112.5°C vs 110°C for the neat composite but T_G is unchanged at 122.5°C. The 63% increase in E' in pGNP/CFRP at ambient conditions shows that the pGNP/epoxy interlaminar region has a higher stiffness and improved the load transfer between fibers and matrix. Most impactful to this dissertation and the temperatures studied is the elimination of the T_β peak because of pGNP restricting side chain movement in the polymer. This behavior is in agreement with Raman spectra showing stretching of polymer chains and reductions of branch vibrations that correspond to the restricted chain mobility. As a result, a decrease in the loss modulus in the T_β temperature range is observed in the pGNP composite. Glass transition is a result of large-scale movement in the polymer backbone rather than independent side chain movement in the beta transition [136]. We can infer that pGNP addition is minimally effective at reducing bulk chain movement in the polymer.

The flexural modulus and strength of the pGNP treated composites were increased by 15% and 17%, respectively at 1.1 g/m². ILSS was improved by 17% at 2.8 g/m². At higher loadings the effectiveness of pGNP addition is reduced which corresponds to the increase in void volume as the void fraction begins to offset or overcome improvements from the pGNP addition. The Short Beam Test was shown to not be a reasonable test of ILSS at elevated temperatures, the Double Notched Shear Test or Arcan Test are more accurate for high stiffness fiber composites at elevated temperatures [141]

The most dramatic area of mechanical improvement is in fracture toughness and analysis for fracture performance in Modes I and II at ambient and elevated temperatures provide significant insight into mechanisms of pGNP reinforcement. At 20°C, Mode I fracture is improved 146% and at 90°C, pGNP/CFRP showed G_{IC} improvements of 126% on initiation. pGNP addition provides substantial increases to the strength of the interlaminar region which—upon crack propagation—resulted in crack front deflection and elongation which—in turn—increase the energy required to extend the crack in the stable, displacement-controlled Mode I fracture. Due to the unstable crack propagation in displacement control mode, Mode II fracture was unaffected by pGNP addition, at ambient conditions. At 90°C, pGNP/CFRP showed no decrease in Mode II toughness compared to 20°C tests as a result of improved storage modulus, resulting in an overall 55% increase in Mode II toughness at 90°C. interlaminar application of pGNP where the improved storage modulus leads to fracture toughness increase at crack initiation. Mode II toughness has had mixed results in literature. Reduction in Mode II toughness has been attributed to failure at matrix/GNP interface due to poor interfacial bonding [69]. Examples of improvement of Mode II fracture have utilized methods of improving the GNP interaction with the matrix [50]. CFRP nanocomposites typically exhibit complex internal structure-property behavior due to interactions between the different constituents. Therefore, the difference in Mode I and Mode II fracture in this study show that pGNP particles provide a direct fracture toughness reinforcement through various means: (i) matrix toughening, (ii) increased elastic properties in the interlaminar region at elevated temperature, and (iii) pGNP particle causing crack deflection.

Investigation of pGNP properties as well as the interactions during composite curing show interaction between pGNP and CFRP on a chemical level. DSC analysis shows pGNP interaction with polymer chain motion, and examinations of fracture mechanics in this work and past studies shows the physical reenforcing of GNP addition. Interlaminar application ensured effective dispersion and targeted pGNP loading at the critical interlaminar region which provides a simple, controllable method of improving composite properties. Surface functionality of pGNP and spray formulation are important in optimizing pGNP/CFRP. The improvements shown in mechanical testing highlight the importance of a complete characterization of GNP properties and how they interact with a composite system to explain and engineer GNP interactions.

10.5. Multifunctionality

EC and TC were optimized at 1.1 g/m² loading, with κ_{22}, κ_{33}, and k_{33} maximized, showing 397%, 168%, and 51% improvements, respectively. κ_{11} and K_{11} were maximized at 2.8 g/m² with 202% and 27%. K_{22} was reduced at all loadings tested. Decreases at higher loadings correspond with void formation. pGNP addition increased EC in each principal direction, which is expected as interlaminar pGNP addition is able to improve the percolation of a conductive network between conductive carbon fibers. Void formation in these regions interferes with the ability for conductive networks to form in the transverse and through thickness directions while percolation along the fiber direction was unaffected.

The effect of increased temperature on electrical conductivity is noteworthy in two ways. First, κ_{11} increases with increasing temperature while κ_{22} and κ_{33} decrease. Second, there is no change in κ_{22} and κ_{33} from 30°C-70°C and a slight decrease at 90°C while κ_{11} shows a linear increase from 30°C-70°C and a nonlinear increase at 90°C which indicated the percolation threshold has suddenly increased with temperature. The sudden shift in performance indicates a phase change in the conductive nature of the composite which has not been previously observed and warrants further explanation.

Increases in TC at 1.1-2.8 g/m² loading show that pGNP particles are well distributed and have good interaction with the epoxy structure which supports the evidence that pGNP particles are well distributed and bound to polymer chains. Higher loading appears to reduce the effectiveness of interactions. In the through thickness direction, interlaminar pGNP are targeted in the thermally resistive region and particles are able to percolate between the fibers, leading to the largest proportional increase in TC. This corresponds to increases in interlaminar strength observed with fracture and short beam testing. The reduction in TC transverse to the fiber direction is unexpected and contrasts with EC, where κ_{22} showed the largest increase.

TC is reliant on phonon transport between pGNP, the epoxy matrix, and carbon fibers, particularly at material interfaces. Improved TC shows strong pGNP/matrix interaction at loadings which correspond with increases in composite strength, stiffness, and fracture toughness. Poor interaction is evidenced by reduced TC—along with a reduction in mechanical properties—which was observed at higher pGNP loadings. Porosity is a cause for reduced TC as well as reduced mechanical properties. Agglomeration of pGNP has been cited as the cause of poor filler-matrix interfaces which results in poor phonon transport at the interface and a loss in heat transfer efficiency [9,10], however this dissertation shows that agglomeration may be the result of poor filler-matrix interfaces, rather than the cause and that chemical interactions may result in void formation.

10.6. Recommendations and Future Work

10.6.1. Curing Chemistry

Isothermal and dynamic DSC show that pGNP addition reduces the peak heat flow and extends the curing time of the composite. The degree to which this is a result of energy going into crosslinking reactions with SFGs and how much is related to pGNP mediating crosslinking reactions is a subject for further study. Likewise, void content may be a result of pGNP agglomeration but may also result from chemical interactions between pGNP and the curing epoxy. The interactions in this dissertation observe that reactions are occurring on a high level, a more detailed examination of the interactions between pGNP SFGs is warranted to more completely understand the reactions occurring and how to utilize them in engineered applications.

10.6.2. Expanded Polymer Systems

Chapter 9 detailed the status of ongoing work with PA6/GF composites. Continuation of this work will provide further detail on pGNP polymer interactions and insight into how pGNP can be integrated with thermoplastic polymers through molding and in-situ polymerization.

The CFRP system used in this dissertation showed a decrease in fracture toughness in the T_β region, which is consistent with other CFRP systems tested [42], however other CFRP systems have not shown weakening due to the T_β transition [43]. Examining the impact of pGNP addition on systems without a T_β transition would be informative in highlighting interactions with polymers with different backbone and side-chain structure.

Expanding the study, as performed in this dissertation into other composite systems would also be valuable. Other thermoset polymer matrixes—such as polyurethane and phenolic—will provide more information on pGNP interactions which will be valuable for engineering multifunctional composites. The strong interaction between pGNP and the epoxy resin is likely related to Van der Waals interactions with aromatic rings in bisphenol A. Diisocyanates in polyurethane systems also contain aromatic rings, and crosslink with functional groups found in pGNP, making polyurethane an interesting target for continued study. Thermoplastic materials such as aramid and PEEK—with significant backbone aromatic groups—also present a promising target for pGNP utilization. Examining manufacturing methods beyond interlaminar application to prepregs has wide applications, as resin transfer molding is less costly than prepreg fabrication and is widely used in industry [156,157].

10.6.3. Expanded Temperature Ranges

DMA results showed a 47% increase in E' in the rubbery state, after T_G. This suggests mechanical improvements at temperatures above T_G which warrant further investigation. Similarly, interlaminar pGNP addition increases the ductility of the epoxy matrix and the DPZ during fracture, which has potential applications at lower temperatures where materials are more brittle. Examining mechanical behaviors at higher and lower temperatures than were studied in this dissertation is recommended.

At 90°C, the percolation threshold of the composite in κ_{11} is increased, highlighting a phase change in the conductive behavior of the nanocomposite separate from the mechanical behavior of the material. This has potential applications for smart materials and SHM.

10.6.4. Anisotropic Properties

Composite samples in this study were unidirectional in order to examine the behavior in three axes with respect to the fiber direction. The potential of engineered anisotropic conductivity is apparent, as the sample tested shows significant anisotropy in thermal and electrical conductivity. Although the pGNP in this study was applied uniformly throughout composite samples, variations in loading could provide targeted properties not possible with GNP dispersed in resin used in RTM. For example, pGNP loading between outer plies will increase surface conductivity without increasing conductivity through the thickness of the composite. Likewise, the potential to produce composites with increased EC without increased TC is indicated, and further examination of pGNP/matrix interactions which increase and interfere with EC and TC are warranted.

Examining conductive behavior with stacking sequences more representative of manufactured composite parts or with woven fiber composites would be informative. Likewise, examining the impacts of glass fiber composite systems would remove the conductivity of the carbon fibers and would give different behavior in each of the material directions.

10.6.5. Electromagnetic Interference Shielding

There is a wide demand for non-metallic EMI shielding materials for military and consumer electronics as well as for battery enclosures in electronic vehicles (EVs). For electronics, there is a demand for flexible, lightweight, and corrosion resistant EMI shielding for lighter, more durable electronics. For EVs, EMI shielding is necessary for battery enclosures which utilize high voltage batteries that create electromagnetic (EM) impulses during AC/DC conversion that can impact the on-board electronics and therefore must be shielded from the rest of the vehicle using special battery enclosures. These battery enclosures in turn must provide fire resistance in the event of cascading thermal runaway of the battery pack that can cause severe thermal damage to the vehicle. Therefore, low electrical conductivity presents a significant hazard in the event of a thermal runaway of the batteries [65,158–161] along with the lack of EMI shielding for onboard electronics. The use of isolated solutions, such as EMI shielding wire mesh and fire protective insulations add parasitic weight, while wire meshes causes concerns due to galvanic corrosion.

pGNP, as demonstrated in this dissertation, has applications in both of these fields. For electronics, interlaminar pGNP can be explored for composite electronics housings, or applied to Mylar and Kapton films. For EV manufacture, interlaminar GNP can provide novel material formulations that can synergistically provide multifunctional properties to achieve the required thermal and electrical conductivities along with improved mechanical performance.

10.6.6. Lightning Strike Protection

Lightning strikes represent a major hazard for aircraft with composite airframes, as airframe construction transitions to CRFP and other composite structures the effects of lightning strike on composite materials becomes more critical and lightning strike protection (LSP) systems must be implemented [162]. Metal aircraft frames are highly conductive and are able to withstand the high currents from lightning strikes [158,163,164] Composite materials have electrical conductivities on the order of 0.01-1 S/m [95]—orders of magnitude lower than metals (10-58 MS/m) [165]—and the low conductivity can present a significant hazard in the event of a lightning strike [158–161]. Carbon fiber reinforced plastic (CFRP) stands out as a leading composite for aircraft structures because of its high strength and low weight but has issues with galvanic corrosion when using aluminum LSP materials, requiring either a fiberglass intermediate material or copper LSP conductors, both of which increase weight [161]. The current state of the art for LSP in composite manufacturing utilizes metallic materials in the form of meshes, foils, or fibers integrated with the composite material. These materials have drawbacks such as integration costs, debonding, high repair costs, and parasitic weight [162].

The interlaminar spray application of pGNP as shown in this dissertation presents a solution to these obstacles. Improvements to EC and TC suggest a significant improvement in LSP. While interlaminar coatings may be effective, there is also potential to explore surface loadings at higher densities than would be mechanically favorable for interlaminar mechanical properties.

10.6.7. Smart Materials

Interlaminar pGNP addition presents several novel opportunities for the development of smart materials, composites with enhanced electronic abilities such as SHM or structural capacitors. SHM has been explored with GNP and other nanomaterials and has clear applications for pGNP. Interlaminar pGNP can be instrumented for live resistance measurements at the conductive ply-to-ply interfaces of glass fiber laminates and in-situ monitoring can be achieved, providing strain and damage data. This allows for microscopic damage nucleation and propagation during fatigue life of a composite to be effectively monitored prior to composite failure. Changes in the conductivity of an interlaminar conductive layer in a composite occur across three distinct regimes; first: linear, reversable piezoresistivity which works as an embedded sensor showing strain in the composite which is not correlated to interlaminar damage, and which returns to the original, unstrained value. Second: nonlinear, irreversible resistance increase, which results in a reduction of conductivity from an unstrained value can indicate the development of fatigue and microscopic damage, when compared to the undamaged configuration. Finally: critical damage, which is detected through a significant change in conductivity, indicating opening and closing of delamination cracks or fracture of composite plies. There is significant potential in utilizing pGNP to monitor composite structures, both in research and commercial application.

Similarly, structural capacitors provide energy storage through composite structures. Frequently this is achieved by stacking conductive carbon fiber layers with non-conductive glass fiber, and as such delamination is a common failure mode owing to the difference in fiber properties. The use of carbon nanoparticles has been proposed as a means of fracture improvement [166,167] which corresponds with the results of this dissertation. The addition of pGNP, percolated with a carbon fiber layer, could increase the functional surface area of the conductive layer which would have a positive impact on capacitance [166].

GO has been used as an insulator, but GNP has not been studied as a conductor [167]. Study of CNT in structural capacitors found that mechanical performance was improved by grafting CNTs on the carbon fibers but there were inverse effects on their electrical properties due to the high viscosity of the non-aqueous, epoxy-based electrolyte, which restricts the access of electrolyte into mesopores on the surface of CNT. As such the introduction of CNTs into CFRP electrodes was not recommended [167]. Given the lateral, 2D structure of pGNP, the pore size issue would not be a factor, and pGNP offers a higher specific surface area and better fracture resistance than CNT. Interlaminar pGNP could be used to produce conductive surfaces or interlaminar films on a dielectric separator composite material for energy storage. The use of GNP in structural capacitors and structural batteries has not been studied and presents an opportunity for novel research.

10.7. Summary

It was the goal of this work to show a more detailed description of graphene/polymer interaction than has been previously shown and to highlight how chemical, mechanical, electrical, and thermal analysis can be used to characterize these interactions.

pGNP was shown to be a more available, lower cost alternative to mineral in Chapter 4. Chemical analysis and electron microscopy showed pGNP to have structure and morphology similar to mineral graphenes while having distinct properties which were used in later chapters to provide more effective integration with CFRP than has been shown with mineral graphene or with graphene oxide. Analysis of the cradle-to-gate environmental impact of pGNP shows that the production of a plant-based material is significantly less environmentally impactful than production of conventional graphene.

Spray application was presented as a means of nanoparticle application with benefits over other methods in Chapter 5. Key factors of suspension formulation were described as particle dispersion, surface energy/wetting, and viscosity, and method for creating an engineered suspension is shown. The improvement in dispersibility of pGNP over mineral graphenes was shown. Spray application is demonstrated as a means of achieving even, low loadings of pGNP to the interlaminar region of composites, a key factor for success in application.

The mechanical and multifunctional benefits of pGNP application were detailed in Chapter 7 and Chapter 8, building on demonstrations of curing kinetics in Chapter 6. The impacts to curing kinetics build on chemical analysis of pGNP and show that there is significant interaction between pGNP and the epoxy matrix on a chemical scale, affecting crosslinking and polymer structure. This strong integration with the CFRP system leads to significantly improved mechanical properties at ambient and elevated temperature. This result also presents methods such as DMA and high temperature mechanical analysis as a means of evaluating nanoparticle/matrix interaction. Increases to EC and TC also highlight the effectiveness of nanoparticle/matrix interaction, which can be used as a tool for understanding nanoparticle/matrix interfaces.

The roots of particle agglomeration in graphene/surface interactions—frequently attributed to difficulty in graphene utilization—were examined. In previous works, nanoparticle agglomeration has been described as a cause of poor particle matrix interactions, void formation, and loss of composite properties. The work of this dissertation has shown that nanoparticle/matrix interactions can be optimized, and that agglomeration may be the result of poor nanoparticle/matrix interaction, rather than the cause. Additionally, observations such as void formation may be the result of chemical interaction which have not previously been observed.

While the above results were shown using pGNP in a CFRP system specifically, it is the goal of the author to present a method for utilization of pGNP and other nanomaterials in composites in general, as well as in other manufacturing applications. The work of Chapter 9—which is ongoing—shows how the results of the preceding chapters can be applied to alternate polymer systems with different target properties.

REFERENCES

[1] Johnson DW, Dobson BP, Coleman KS. A manufacturing perspective on graphene dispersions. Current Opinion in Colloid & Interface Science 2015;20:367–82. https://doi.org/10.1016/j.cocis.2015.11.004.

[2] Sherman LM. A Bright Future for Thermally Conductive Plastics n.d. https://www.ptonline.com/articles/a-bright-future-for-thermally-conductive-plastics (accessed November 8, 2021).

[3] Liu J, Li Y, Xiang D, Zhao C, Wang B, Li H. Enhanced Electrical Conductivity and Interlaminar Fracture Toughness of CF/EP Composites via Interleaving Conductive Thermoplastic Films. Appl Compos Mater 2021;28:17–37. https://doi.org/10.1007/s10443-020-09848-w.

[4] Plastech. Graphene nanotubes in plastics are the basis for cars of the future n.d. https://www.plastech.biz/en/news/Graphene-nanotubes-in-plastics-are-the-basis-for-cars-of-the-15628 (accessed November 8, 2021).

[5] Clark R. Real world graphene: Industrial applications for the 21st century 2017.

[6] Geim AK, Novoselov KS. THE RISE OF GRAPHENE n.d.:14.

[7] Joshi SC, Dikshit V. Enhancing interlaminar fracture characteristics of woven CFRP prepreg composites through CNT dispersion. Journal of Composite Materials 2012;46:665–75. https://doi.org/10.1177/0021998311410472.

[8] Gong G. Literature study of graphene modified polymeric composites 2018:57.

[9] Lv R, Ren Y, Guo H, Bai S. Recent progress on thermal conductivity of graphene filled epoxy composites. Nano Materials Science 2022;4:205–19. https://doi.org/10.1016/j.nanoms.2021.06.001.

[10] Su Y, Li JJ, Weng GJ. Theory of thermal conductivity of graphene-polymer nanocomposites with interfacial Kapitza resistance and graphene-graphene contact resistance. Carbon 2018;137:222–33. https://doi.org/10.1016/j.carbon.2018.05.033.

[11] Md Said NH, Liu W, Khe C, Lai C, Zulkepli NN, Aziz A. Review of the past and recent developments in functionalization of graphene derivatives for reinforcement of polypropylene nanocomposites. Polymer Composites 2021;42:1075–108. https://doi.org/10.1002/pc.25922.

[12] Pizza A, Metz R, Hassanzadeh M, Bantignies J-L. Life cycle assessment of nanocomposites made of thermally conductive graphite nanoplatelets. Int J Life Cycle Assess 2014;19:1226–37. https://doi.org/10.1007/s11367-014-0733-2.

[13] Cossutta M, McKechnie J, Pickering SJ. Comparative LCA of different graphene production routes. University of Nottingham, Nottingham NG7 2RD, UK 2017:18.

[14] Serrano-Luján L, Víctor-Román S, Toledo C, Sanahuja-Parejo O, Mansour AE, Abad J, et al. Environmental impact of the production of graphene oxide and reduced graphene oxide. SN Appl Sci 2019;1:179. https://doi.org/10.1007/s42452-019-0193-1.

[15] Arvidsson R. Review of environmental life cycle assessment studies of graphene production. Adv Mater Lett 2017;8:187–95. https://doi.org/10.5185/amlett.2017.1413.

[16] Choi NS, Kinloch AJ, Williams JG. Delamination Fracture of Multidirectional Carbon-Fiber/Epoxy Composites under Mode I, Mode II and Mixed-Mode I/II Loading. Journal of Composite Materials 1999;33:73–100. https://doi.org/10.1177/002199839903300105.

[17] Johnson C. 2020 State of the Industry Report. Composites Manufacturing Magazine 2020. https://compositesmanufacturingmagazine.com/2020/01/2020-state-of-the-industry-report/ (accessed February 15, 2023).

[18] Composites Industry Market Overview. American Composites Manufacturers Association n.d. https://acmanet.org/composites-industry-overview/ (accessed February 15, 2023).

[19] Singh R, Sandhu GS, Penna R, Farina I. Investigations for Thermal and Electrical Conductivity of ABS-Graphene Blended Prototypes. Materials (Basel) 2017;10:881. https://doi.org/10.3390/ma10080881.

[20] Coronado P, Argüelles A, Viña J, Mollón V, Viña I. Influence of temperature on a carbon–fibre epoxy composite subjected to static and fatigue loading under mode-I delamination. International Journal of Solids and Structures 2012;49:2934–40. https://doi.org/10.1016/j.ijsolstr.2012.05.018.

[21] Bilisik K, Akter M. Graphene nanocomposites: A review on processes, properties, and applications. Journal of Industrial Textiles 2022;51:3718S-3766S. https://doi.org/10.1177/15280837211024252.

[22] Batista CAS, Larson RG, Kotov NA. Nonadditivity of nanoparticle interactions. Science 2015;350:1242477. https://doi.org/10.1126/science.1242477.

[23] Park YT, Qian Y, Chan C, Suh T, Nejhad MG, Macosko CW, et al. Epoxy Toughening with Low Graphene Loading. Advanced Functional Materials 2015;25:575–85. https://doi.org/10.1002/adfm.201402553.

[24] Rafiee MA, Rafiee J, Wang Z, Song H, Yu Z-Z, Koratkar N. Enhanced Mechanical Properties of Nanocomposites at Low Graphene Content. ACS Nano 2009;3:3884–90. https://doi.org/10.1021/nn9010472.

[25] Ning H, Li J, Hu N, Yan C, Liu Y, Wu L, et al. Interlaminar mechanical properties of carbon fiber reinforced plastic laminates modified with graphene oxide interleaf. Carbon 2015;91:224–33. https://doi.org/10.1016/j.carbon.2015.04.054.

[26] Kamar NT, Hossain MM, Khomenko A, Haq M, Drzal LT, Loos A. Interlaminar reinforcement of glass fiber/epoxy composites with graphene nanoplatelets. Composites Part A: Applied Science and Manufacturing 2015;70:82–92. https://doi.org/10.1016/j.compositesa.2014.12.010.

[27] Zhao X, Chen W, Han X, Zhao Y, Du S. Enhancement of interlaminar fracture toughness in textile-reinforced epoxy composites with polyamide 6/graphene oxide interlaminar toughening tackifier. Composites Science and Technology 2020;191:108094. https://doi.org/10.1016/j.compscitech.2020.108094.

[28] Mishra K, Bastola KP, Singh RP, Vaidyanathan R. Effect of Graphene Oxide on the Interlaminar Fracture Toughness of Carbon Fiber/Epoxy Composites. Polymer Engineering and Science 2019;59:1199–209.

[29] Liu B, Cao S, Gao N, Cheng L, Liu Y, Zhang Y, et al. Thermosetting CFRP interlaminar toughening with multi-layers graphene and MWCNTs under mode I fracture. Composites Science and Technology 2019;183:107829. https://doi.org/10.1016/j.compscitech.2019.107829.

[30] Nagi CS, Ogin SL, Mohagheghian I, Crean C, Foreman AD. Spray deposition of graphene nano-platelets for modifying interleaves in carbon fibre reinforced polymer laminates. Materials & Design 2020;193:108831. https://doi.org/10.1016/j.matdes.2020.108831.

[31] Yu A, Ramesh P, Itkis ME, Bekyarova E, Haddon RC. Graphite Nanoplatelet−Epoxy Composite Thermal Interface Materials. J Phys Chem C 2007;111:7565–9. https://doi.org/10.1021/jp071761s.

[32] Teng C-C, Ma C-CM, Lu C-H, Yang S-Y, Lee S-H, Hsiao M-C, et al. Thermal conductivity and structure of non-covalent functionalized graphene/epoxy composites. Carbon 2011;49:5107–16. https://doi.org/10.1016/j.carbon.2011.06.095.

[33] Liu H, Dong M, Huang W, Gao J, Dai K, Guo J, et al. Lightweight conductive graphene/thermoplastic polyurethane foams with ultrahigh compressibility for piezoresistive sensing. J Mater Chem C 2017;5:73–83. https://doi.org/10.1039/C6TC03713E.

[34] Kravchenko OG, Pedrazzoli D, Kovtun D, Qian X, Manas-Zloczower I. Incorporation of plasma-functionalized carbon nanostructures in composite laminates for interlaminar reinforcement and delamination crack monitoring. Journal of Physics and Chemistry of Solids 2018;112:163–70. https://doi.org/10.1016/j.jpcs.2017.09.018.

[35] Kravchenko OG, Pedrazzoli D, Bonab VS, Manas-Zloczower I. Conductive interlaminar interfaces for structural health monitoring in composite laminates under fatigue loading. Materials & Design 2018;160:1217–25. https://doi.org/10.1016/j.matdes.2018.10.045.

[36] Kravchenko OG, Solouki Bonab V, Manas-Zloczower I. Spray-Assisted Microwave Welding of Thermoplastics Using Carbon Nanostructures with Enabled Health Monitoring. Polymer Engineering & Science 2019;59:2247–54. https://doi.org/10.1002/pen.25227.

[37] Zhang H, Liu Y, Kuwata M, Bilotti E, Peijs T. Improved fracture toughness and integrated damage sensing capability by spray coated CNTs on carbon fibre prepreg. Composites Part A: Applied Science and Manufacturing 2015;70:102–10. https://doi.org/10.1016/j.compositesa.2014.11.029.

[38] Sun Z, Li Y-Q, Huang P, Cao H-J, Zeng W, Li J, et al. Temperature-dependent mechanical properties of polyetherimide composites reinforced by graphene oxide-coated short carbon fibers. Composite Structures 2021;270:114075. https://doi.org/10.1016/j.compstruct.2021.114075.

[39] Gangineni PK, Patnaik S, Gupta K. BNVSG, Prusty RK, Ray BC. Interfacial behavior of graphene carboxyl-grafted carbon fiber reinforced polymer composites at elevated temperatures: Emphasis on the effect of electrophoretic deposition time. Polymer Composites 2021;42:5893–903. https://doi.org/10.1002/pc.26269.

[40] Araki W, Shintaku H, Ohashi H, Horiuchi Y, Arai Y. Temperature dependence and fracture criterion of mixed mode I/II fracture toughness of phenolic resin for friction material. Journal of Applied Polymer Science 2011;121:2301–9. https://doi.org/10.1002/app.33939.

[41] Sales R de CM, Gusmão SR, Gouvêa RF, Chu T, Marlet JMF, Cândido GM, et al. The temperature effects on the fracture toughness of carbon fiber/RTM-6 laminates

processed by VARTM. Journal of Composite Materials 2017;51:1729–41. https://doi.org/10.1177/0021998316679499.

[42] Kim H-S, Wang W, Takao Y. Effects of temperature and fiber orientation on mode I interlaminar fracture toughness of carbon/epoxy composites. Durability of composite systems, Paris, France: 1999.

[43] Celebi K, Daricik F. Mode I Interlaminar Fracture Behaviour of Carbon/Epoxy Laminated Composites under Different Temperatures. Çukurova University Journal of the Faculty of Engineering and Architecture 2017;32. https://doi.org/10.21605/cukurovaummfd.310102.

[44] Sun G, Zuo W, Chen D, Luo Q, Pang T, Li Q. On the effects of temperature on tensile behavior of carbon fiber reinforced epoxy laminates. Thin-Walled Structures 2021;164:107769. https://doi.org/10.1016/j.tws.2021.107769.

[45] Jia Z, Li T, Chiang F, Wang L. An experimental investigation of the temperature effect on the mechanics of carbon fiber reinforced polymer composites. Composites Science and Technology 2018;154:53–63. https://doi.org/10.1016/j.compscitech.2017.11.015.

[46] Bosze EJ, Alawar A, Bertschger O, Tsai Y-I, Nutt SR. High-temperature strength and storage modulus in unidirectional hybrid composites. Composites Science and Technology 2006;66:1963–9. https://doi.org/10.1016/j.compscitech.2006.01.020.

[47] Kostagiannakopoulou C, Loutas TH, Sotiriadis G, Markou A, Kostopoulos V. On the interlaminar fracture toughness of carbon fiber composites enhanced with graphene nano-species. Composites Science and Technology 2015;118:217–25. https://doi.org/10.1016/j.compscitech.2015.08.017.

[48] Senis EC, Golosnoy IO, Andritsch T, Dulieu-Barton JM, Thomsen OT. The influence of graphene oxide filler on the electrical and thermal properties of unidirectional carbon fiber/epoxy laminates: Effect of out-of-plane alignment of the graphene oxide nanoparticles. Polymer Composites 2020;41:3510–20. https://doi.org/10.1002/pc.25637.

[49] Rodríguez-González JA, Rubio-González C. Influence of sprayed multi-walled carbon nanotubes on mode I and mode II interlaminar fracture toughness of carbon fiber/epoxy composites. Advanced Composite Materials 2018:1–18. https://doi.org/10.1080/09243046.2018.1458510.

[50] Kumar A, Roy S. Characterization of mixed mode fracture properties of nanographene reinforced epoxy and Mode I delamination of its carbon fiber composite. Composites Part B: Engineering 2018;134:98–105. https://doi.org/10.1016/j.compositesb.2017.09.052.

[51] Kumar A, Li S, Roy S, King JA, Odegard GM. Fracture properties of nanographene reinforced EPON 862 thermoset polymer system. Composites Science and Technology 2015;114:87–93. https://doi.org/10.1016/j.compscitech.2015.04.008.

[52] Kang W-S, Rhee KY, Park S-J. Thermal, impact and toughness behaviors of expanded graphite/graphite oxide-filled epoxy composites. Composites Part B: Engineering 2016;94:238–44. https://doi.org/10.1016/j.compositesb.2016.03.052.

[53] Kang W-S, Rhee KY, Park S-J. Influence of surface energetics of graphene oxide on fracture toughness of epoxy nanocomposites. Composites Part B: Engineering 2017;114:175–83. https://doi.org/10.1016/j.compositesb.2017.01.032.

[54] Campell M. EMI Shielding Solutions for Automotive FRP Composite Applications 2021.

[55] Sang M, Shin J, Kim K, Yu KJ. Electronic and Thermal Properties of Graphene and Recent Advances in Graphene Based Electronics Applications. Nanomaterials (Basel) 2019;9:374. https://doi.org/10.3390/nano9030374.

[56] Kohne M, Rizzi L. Can graphene compete with copper in electrical conductivity? Bosch Global n.d. https://www.bosch.com/stories/can-graphene-compete-with-copper-in-electrical-conductivity/ (accessed February 14, 2022).

[57] Gagné M, Therriault D. Lightning strike protection of composites. Progress in Aerospace Sciences 2014;64:1–16. https://doi.org/10.1016/j.paerosci.2013.07.002.

[58] Imran KA, Shivakumar KN. Enhancement of electrical conductivity of epoxy using graphene and determination of their thermo-mechanical properties. Journal of Reinforced Plastics and Composites 2018;37:118–33. https://doi.org/10.1177/0731684417736143.

[59] Joven R, Das R, Ahmed A, Roozbehjavan P, Minaie B. THERMAL PROPERTIES OF CARBON FIBER-EPOXY COMPOSITES WITH DIFFERENT FABRIC WEAVES n.d.:14.

[60] Thakre PR, Lagoudas DC, Riddick JC, Gates TS, Frankland S-JV, Ratcliffe JG, et al. Investigation of the effect of single wall carbon nanotubes on interlaminar fracture toughness of woven carbon fiber—epoxy composites. Journal of Composite Materials 2011;45:1091–107. https://doi.org/10.1177/0021998310389088.

[61] Vignesh V, Nagaprasad N, Karthik Babu NB, Manimaran P, Stalin B, Ramaswamy K. Effect of green hybrid fillers loading on mechanical and thermal properties of vinyl ester composites. Polymer Composites 2022:pc.26925. https://doi.org/10.1002/pc.26925.

[62] Ma L-L, Liu W-J, Hu X, Lam PKS, Zeng JR, Yu H-Q. Ionothermal carbonization of biomass to construct sp2/sp3 carbon interface in N-doped biochar as efficient oxygen reduction electrocatalysts. Chemical Engineering Journal 2020;400:125969. https://doi.org/10.1016/j.cej.2020.125969.

[63] Scientific TF. Investigating the shear flow and thixotropic behavior of paints and coatings 2019:4.

[64] Eley RR. Applied rheology and architectural coating performance. Journal of Coatings Technology and Research 2019;16:263–305. https://doi.org/10.1007/s11998-019-00187-5.

[65] Barkan T. Graphene: the hype versus commercial reality. Nat Nanotechnol 2019;14:904–6. https://doi.org/10.1038/s41565-019-0556-1.

[66] Housecroft C, Sharpe A G. Inorganic Chemistry. 2nd ed. Pearson Prentice-Hal; 2005.

[67] Banhart F. Elemental carbon in the sp1 hybridization. ChemTexts 2020;6:3. https://doi.org/10.1007/s40828-019-0098-z.

[68] Mueller JO, Su DS, Schloegl R. Carbon Hybridization Determination in Soot and Carbon Black 2006.

[69] Ahmadi-Moghadam B, Taheri F. Fracture and toughening mechanisms of GNP-based nanocomposites in modes I and II fracture. Engineering Fracture Mechanics 2014;131:329–39.

[70] Mopoung S, Moonsri P, Palas W, Khumpai S. Characterization and Properties of Activated Carbon Prepared from Tamarind Seeds by KOH Activation for Fe(III) Adsorption from Aqueous Solution. The Scientific World Journal 2015;2015:e415961. https://doi.org/10.1155/2015/415961.

[71] Dhakate SR, Bahl OP. Effect of carbon fiber surface functional groups on the mechanical properties of carbon–carbon composites with HTT 2003:11.

[72] Adak NC, Chhetri S, Kim NH, Murmu NC, Samanta P, Kuila T. Static and Dynamic Mechanical Properties of Graphene Oxide-Incorporated Woven Carbon Fiber/Epoxy Composite. Journal of Materials Engineering and Performance 2018;27:1138–47. https://doi.org/10.1007/s11665-018-3201-5.

[73] Shadlou S, Alishahi E, Ayatollahi MR. Fracture behavior of epoxy nanocomposites reinforced with different carbon nano-reinforcements. Composite Structures 2013;95:577–81. https://doi.org/10.1016/j.compstruct.2012.08.002.

[74] Tsymbal. Section 08_Electron_Transport.pdf n.d.

[75] Bhattacharya S, Das S, Das D, Rahaman H. Electrical transport in graphene nanoribbon interconnect. 2014 2nd International Conference on Devices, Circuits and Systems (ICDCS), Combiatore, India: IEEE; 2014, p. 1–4. https://doi.org/10.1109/ICDCSyst.2014.6926148.

[76] Mafakheri M, Dodaran AAS. Graphene phonons lifetime and mean free path using ab initio molecular dynamics and spectral energy density analysis. Phys Scr 2021;96:065702. https://doi.org/10.1088/1402-4896/abede2.

[77] Ramdani N. Nanotechnology in Aerospace and Structural Mechanics n.d.:374.

[78] Hahn DW, Özisik MN. Heat Conduction. 3rd Edition. Wiley; 2012.

[79] Saito R, Mizuno M, Dresselhaus MS. Ballistic and Diffusive Thermal Conductivity of Graphene. Phys Rev Applied 2018;9:024017. https://doi.org/10.1103/PhysRevApplied.9.024017.

[80] Yang H, Yuan L, Yao X, Fang D. Piezoresistive response of graphene rubber composites considering the tunneling effect. Journal of the Mechanics and Physics of Solids 2020;139:103943. https://doi.org/10.1016/j.jmps.2020.103943.

[81] Garrett KW, Rosenberg HM. The thermal conductivity of epoxy-resin / powder composite materials. J Phys D: Appl Phys 1974;7:1247–58. https://doi.org/10.1088/0022-3727/7/9/311.

[82] Seki Y, Kizilkan E, İşbilir A, Sarikanat M, Altay L. Enhanced in-plane and through-plane thermal conductivity and mechanical properties of polyamide 4.6 composites loaded with hybrid carbon fiber, synthetic graphite and graphene. Polymer Composites 2021;42:4630–42. https://doi.org/10.1002/pc.26174.

[83] Zhang F, Yang K, Liu G, Chen Y, Wang M, Li S, et al. Recent advances on graphene: Synthesis, properties and applications. Composites Part A: Applied Science and Manufacturing 2022;160:107051. https://doi.org/10.1016/j.compositesa.2022.107051.

[84] Jafari I, Shakiba M, Khosravi F, Ramakrishna S, Abasi E, Teo YS, et al. Thermal Degradation Kinetics and Modeling Study of Ultra High Molecular Weight Polyethylene (UHMWP)/Graphene Nanocomposite. Molecules 2021;26:1597. https://doi.org/10.3390/molecules26061597.

[85] Garcia PS, Oliveira YDC, Valim FCF, Kotsilkova R, Ivanov E, Donato RK, et al. Tailoring the graphene oxide chemical structure and morphology as a key to

polypropylene nanocomposite performance. Polymer Composites 2021;42:6213–31. https://doi.org/10.1002/pc.26297.

[86] Liu H, Li Y, Wang T, Wang Q. In situ synthesis and thermal, tribological properties of thermosetting polyimide/graphene oxide nanocomposites. J Mater Sci 2012;47:1867–74. https://doi.org/10.1007/s10853-011-5975-9.

[87] Singh PK, Sharma K. Molecular Dynamics Simulation of Glass Transition Behavior of Polymer based Nanocomposites. Journal of Scientific & Industrial Research 2018:4.

[88] Yu JW, Jung J, Choi M, Choi JH, Yu J, Lee K, et al. Enhancement of Crosslink Density, Glass Transition Temperature, and Strength of Epoxy Resin by Using Functionalized Graphene Oxide Co-curing Agents 2016:10.

[89] Masson-Delmotte V, Zhai P, Pirani A, Connors SL, Péan C, Berger S, et al. IPCC, 2021: Climate Change 2021: The Physical Science Basis. Contribution of Working Group I to the Sixth Assessment Report of the Intergovernmental Panel on Climate Change. Cambridge University Press; n.d.

[90] The Cement Sustainability Initiative: Our agenda for action. World Business Council for Sustainable Development; 2002.

[91] Long W-J, Zheng D, Duan H, Han N, Xing F. Performance enhancement and environmental impact of cement composites containing graphene oxide with recycled fine aggregates. Journal of Cleaner Production 2018;194:193–202. https://doi.org/10.1016/j.jclepro.2018.05.108.

[92] Papanikolaou I, Arena N, Al-Tabbaa A. Graphene nanoplatelet reinforced concrete for self-sensing structures – A lifecycle assessment perspective 2019. https://doi.org/10.17863/CAM.43464.

[93] Rubber tire life cycle assessment and the effect of reducing carbon footprint by replacing carbon black with graphene: International Journal of Green Energy: Vol 14, No 1 n.d. https://www.tandfonline.com/doi/abs/10.1080/15435075.2016.1253575?journalCode=ljge20 (accessed November 8, 2021).

[94] Jara AD, Betemariam A, Woldetinsae G, Kim JY. Purification, application and current market trend of natural graphite: A review. International Journal of Mining Science and Technology 2019;29:671–89. https://doi.org/10.1016/j.ijmst.2019.04.003.

[95] Fang C, Zhang J, Chen X, Weng GJ. Calculating the Electrical Conductivity of Graphene Nanoplatelet Polymer Composites by a Monte Carlo Method. Nanomaterials 2020;10:1129. https://doi.org/10.3390/nano10061129.

[96] Zhang H, Liu Y, Huo S, Briscoe J, Tu W, Picot OT, et al. Filtration effects of graphene nanoplatelets in resin infusion processes: Problems and possible solutions. Composites Science and Technology 2017;139:138–45. https://doi.org/10.1016/j.compscitech.2016.12.020.

[97] Shan FL, Gu YZ, Li M, Liu YN, Zhang ZG. Effect of deposited carbon nanotubes on interlaminar properties of carbon fiber-reinforced epoxy composites using a developed spraying processing. Polym Compos 2013;34:41–50. https://doi.org/10.1002/pc.22375.

[98] Almuhammadi K, Alfano M, Yang Y, Lubineau G. Analysis of interlaminar fracture toughness and damage mechanisms in composite laminates reinforced with sprayed

multi-walled carbon nanotubes. Materials & Design 2014;53:921–7. https://doi.org/10.1016/j.matdes.2013.07.081.

[99] Leow C, Kreider PB, Notthoff C, Kluth P, Tricoli A, Compston P. A graphene film interlayer for enhanced electrical conductivity in a carbon-fibre/PEEK composite. Functional Composite Mater 2021;2:1. https://doi.org/10.1186/s42252-020-00015-9.

[100] Luong ND, Hippi U, Korhonen JT, Soininen AJ, Ruokolainen J, Johansson L-S, et al. Enhanced mechanical and electrical properties of polyimide film by graphene sheets via in situ polymerization. Polymer 2011;52:5237–42. https://doi.org/10.1016/j.polymer.2011.09.033.

[101] Senis EC, Golosnoy IO, Dulieu-Barton JM, Thomsen OT. Enhancement of the electrical and thermal properties of unidirectional carbon fibre/epoxy laminates through the addition of graphene oxide. J Mater Sci 2019;54:8955–70. https://doi.org/10.1007/s10853-019-03522-8.

[102] Imran KA, Shivakumar KN. Graphene-modified carbon/epoxy nanocomposites: Electrical, thermal and mechanical properties. Journal of Composite Materials 2019;53:93–106. https://doi.org/10.1177/0021998318780468.

[103] Zhang B, Soltani SA, Le LN, Asmatulu R. Fabrication and assessment of a thin flexible surface coating made of pristine graphene for lightning strike protection. Materials Science and Engineering: B 2017;216:31–40. https://doi.org/10.1016/j.mseb.2017.02.008.

[104] Han J. The combination of carbon nanotube buckypaper and insulating adhesive for lightning strike protection of Formulaction Scientific Instruments 2020. https://formulaction.com/what-is-a-colloidal-dispersion-and-how-to-measure-its-stability/ (accessed March 20, 2023).

[132] Polarity Index n.d. https://macro.lsu.edu/howto/solvents/polarity%20index.htm (accessed August 9, 2022).

[133] Hassan M, Reddy KR, Haque E, Minett AI, Gomes VG. High-yield aqueous phase exfoliation of graphene for facile nanocomposite synthesis via emulsion polymerization. Journal of Colloid and Interface Science 2013;410:43–51. https://doi.org/10.1016/j.jcis.2013.08.006.

[134] Domínguez JC. Thermosets, Chapter 4 - Rheology and curing process of thermosets. In: Guo Q, editor. Thermosets (Second Edition). Second Edition, Elsevier; 2018, p. 115–46. https://doi.org/10.1016/B978-0-08-101021-1.00004-6.

[135] Rao YS, Shivamurthy B, Shetty N, Mohan NS. Thermomechanical Properties of Carbon Fabric Reinforced Epoxy Laminates with h-BN and MoS2 Fillers. Mat Res 2021;24:e20210215. https://doi.org/10.1590/1980-5373-mr-2021-0215.

[136] Dynamic Mechanical Analysis Basics: Part 2 Thermoplastic Transitions and Properties 2007.

[137] Boyer RF. Dependence of mechanical properties on molecular motion in polymers. Polym Eng Sci 1968;8:161–85. https://doi.org/10.1002/pen.760080302.

[138] Deng SH, Zhou XD, Zhu MQ, Fan CJ, Lin QF. Interfacial toughening and consequent improvement in fracture toughness of carbon fiber reinforced epoxy resin composites: induced by diblock copolymers. Express Polym Lett 2013;7:925–35. https://doi.org/10.3144/expresspolymlett.2013.90.

[139] Kumar PS. Synergistic effect of carbon fabric and multiwalled carbon nanotubes on the fracture, wear and dynamic load response of epoxy-based multiscale composites. Polymer Bulletin 2022:22.
[140] Garcia FG, Soares BG, Pita VJRR, Sánchez R, Rieumont J. Mechanical properties of epoxy networks based on DGEBA and aliphatic amines. Journal of Applied Polymer Science 2007;106:2047–55. https://doi.org/10.1002/app.24895.
[141] Daniel I, Ishai O. Determination of Through Thickness Properties. Engineering Mechanics of Composite Materials. Second Edition, New York: Oxford University Press; 2006, p. 329–35.
[142] Orowan E. Fracture and strength of solids. Reports on Progress in Physics 1949;12:185–232. https://doi.org/10.1088/0034-4885/12/1/309.
[143] Kravchenko OG, Kravchenko SG, Sun C-T. Thickness dependence of mode I interlaminar fracture toughness in a carbon fiber thermosetting composite. Composite Structures 2017;160:538–46. https://doi.org/10.1016/j.compstruct.2016.10.088.
[144] Chaudhry MS, Czekanski A, Zhu ZH. Characterization of carbon nanotube enhanced interlaminar fracture toughness of woven carbon fiber reinforced polymer composites. International Journal of Mechanical Sciences 2017;131–132:480–9. https://doi.org/10.1016/j.ijmecsci.2017.06.016.
[145] Yoshihara H, Satoh A. Shear and crack tip deformation correction for the double cantilever beam and three-point end-notched flexure specimens for mode I and mode II fracture toughness measurement of wood. Engineering Fracture Mechanics 2009;76 (3):335–46.
[146] Gong Y, Jiang L, Li L, Zhao J. An Experimental and Numerical Study of the Influence of Temperature on Mode II Fracture of a T800/Epoxy Unidirectional Laminate. Materials 2022;15:8108. https://doi.org/10.3390/ma15228108.
[147] Lincoln RL, Scarpa F, Ting VP, Trask RS. Multifunctional composites: a metamaterial perspective. Multifunct Mater 2019;2:043001. https://doi.org/10.1088/2399-7532/ab5242.
[148] Guo Y, Ruan K, Shi X, Yang X, Gu J. Factors affecting thermal conductivities of the polymers and polymer composites: A review. Composites Science and Technology 2020;193:108134. https://doi.org/10.1016/j.compscitech.2020.108134.
[149] Mulqueen DW, Sattar S, Kravchenko OG, Le T. Spray deposition of sustainable plant-based graphene in thermosetting carbon fiber laminates for mechanical, thermal, and electrical properties. Polym Compos 2022;1:19. https://doi.org/10.1002/pc.27051.
[150] Mulqueen DW, Sattar S, Kravchenko OG. Mechanical and thermal properties of carbon fiber epoxy composite with interlaminar graphene at elevated temperature. Composites Part B: Engineering 2023:110609. https://doi.org/10.1016/j.compositesb.2023.110609.
[151] Zhao X, Li Y, Chen W, Li S, Zhao Y, Du S. Improved fracture toughness of epoxy resin reinforced with polyamide 6/graphene oxide nanocomposites prepared via in situ polymerization. Composites Science and Technology 2019;171:180–9. https://doi.org/10.1016/j.compscitech.2018.12.023.
[152] Polyamides. Chemistry LibreTexts 2013. https://chem.libretexts.org/Bookshelves/Organic_Chemistry/Supplemental_Modules

_(Organic_Chemistry)/Amides/Reactivity_of_Amides/Polyamides (accessed March 20, 2023).

[153] Chen J, Liu G, Jin L, Ni P, Li Z, He H, et al. Catalytic hydrolysis of waste nylon 6 to produce ε-caprolactam in sub-critical water. Journal of Analytical and Applied Pyrolysis 2010;87:50–5. https://doi.org/10.1016/j.jaap.2009.10.004.

[154] Groop EE, Nowicki AW, Calle CI, Buhler CR, Mantovani JG, Aerospace S. Comparison of Surface Resistivity and Triboelectric Charge Generation Characteristics of Materials n.d.

[155] Ghosh S, Santhosh R, Jeniffer S, Raghavan V, Jacob G, Nanaji K, et al. Natural biomass derived hard carbon and activated carbons as electrochemical supercapacitor electrodes. Sci Rep 2019;9:16315. https://doi.org/10.1038/s41598-019-52006-x.

[156] Mishnaevsky L, Branner K, Petersen HN, Beauson J, McGugan M, Sørensen BF. Materials for Wind Turbine Blades: An Overview. Materials (Basel) 2017;10:1285. https://doi.org/10.3390/ma10111285.

[157] Watson JC, Serrano JC. Composite Materials for Wind Blades n.d.:6.

[158] Revel I, Evans S, Flourens F. Edge glow: A combined voltage/power controlled mechanism? 2016 33rd International Conference on Lightning Protection (ICLP), Estoril: IEEE; 2016, p. 1–6. https://doi.org/10.1109/ICLP.2016.7791388.

[159] Kawakami H. Lightning Strike Induced Damage Mechanisms of Carbon Fiber Composites. PhD Thesis. University of Washington, 2011.

[160] Morgan D, Hardwick CJ, Haigh SJ, Meakins AJ. The Interaction of Lightning with Aircraft and the Challenges of Lightning Testing 2012:11.

[161] Black S. Lightning strike protection strategies for composite aircraft. Composite World 2013. https://www.compositesworld.com/articles/lightning-strike-protection-strategies-for-composite-aircraft (accessed February 12, 2022).

[162] Kumar V, Yokozeki T, Karch C, Hassen AA, Hershey CJ, Kim S, et al. Factors affecting direct lightning strike damage to fiber reinforced composites: A review. Composites Part B: Engineering 2020;183:107688. https://doi.org/10.1016/j.compositesb.2019.107688.

[163] Lepetit B, Escure C, Guinard S, Revel I, Peres G. Thermo-mechanical effects induced by lightning on carbon fiber composite materials 2011.

[164] Laroche P, Blanchet P, Delannoy A, Issac F. Experimental Studies of Lightning Strikes to Aircraft 2012:14.

[165] TIBTECH innovations: Metal properties comparison: electric conductivity, thermal conductivity, density, melting temperature n.d. https://www.tibtech.com/conductivite.php?lang=en_US (accessed February 14, 2022).

[166] Qian H, Diao HL, Houllé M, Amadou J, Shirshova N, Greenhalgh ES, et al. CARBON FIBRE MODIFICATIONS FOR COMPOSITE STRUCTURAL POWER DEVICES 2012:5.

[167] Chan K-Y, Jia B, Lin H, Hameed N, Lee J-H, Lau K-T. A critical review on multifunctional composites as structural capacitors for energy storage. Composite Structures 2018;188:126–42. https://doi.org/10.1016/j.compstruct.2017.12.072.

VITA

Daniel W. Mulqueen

Ph.D., Mechanical Engineering, Old Dominion University, College of Engineering & Technology

1105 Engineering Systems Building, Norfolk, VA 23529

B.S., Engineering Physics, Colorado School of Mines

1500 Illinois St, Golden, CO 80401

Daniel Mulqueen was born in Denver, Colorado, USA in 1985. He received his bachelor's degree from the Colorado School of Mines in Engineering Physics in 2008. In his senior design project, he worked on the development of photosensitive, nanoscale molecular motors. Since 2008, he has designed processes and equipment for the production of renewable, plant-based carbon materials including biochar, bio-coal, activated carbon, carbon fillers, and nanocarbons. In January 2020, he joined the Mechanical and Aerospace Engineering Department at Old Dominion University to pursue his Ph.D. in Mechanical Engineering. Pyrolysis systems he has designed include plants operating in six US states as well as Canada, India and Estonia. His doctoral research is on the mechanisms of interaction between graphitic nanoparticles and composite systems, with the focus on multifunctional properties at elevated temperatures. Daniel defended his doctoral thesis in August 2023.

Selected publications:

D. W. Mulqueen, S. Sattar, O. G. Kravchenko, “Mechanical and thermal properties of carbon fiber epoxy composite with interlaminar graphene at elevated temperature,” *Composites Part B*, Feb. 2023

D. W. Mulqueen, S. Sattar, T. Le, O. G. Kravchenko, Le T. “Spray deposition of sustainable plant based graphene in thermosetting carbon fiber laminates for mechanical, thermal, and electrical properties.” *Polym Compos* 2022; 1:19. https://doi.org/10.1002/pc.27051.

R. A. Adams, A. D. Dysart, R. Esparza, S. Acuña, S. R. Joshi, A. Cox, D. Mulqueen, V. G. Pol, "Superior lithium-ion storage at room and elevated temperature in an industrial woodchip derived porous carbon," *Ind. Eng. Chem. Res.*, **2016**, 55 (32), 8706–8712.

US20110278150A1, Daniel W. Mulqueen, James L. Fournier, Thomas B. Reed “Method and apparatus for continuous production of carbonaceous pyrolysis by-products,” Priority Date: 2010-05-05, Publication Date:

2015-08-18